REPORT DOCUMENTATION PAGE

Form Approved
OMB No. 0704-0188

1. REPORT DATE (DD-MM-YYYY)
December 3, 2003

2. REPORT TYPE
Final Report

3. Final
01 AUG 02 - 31 DEC 03

4. TITLE AND SUBTITLE
New Technologies for Polymer and Bio-Optic Systems for Broad Military and Civilian Applications

5a. CONTRACT NUMBER
DAAD19-02-1-0338

5b. GRANT NUMBER

5c. PROGRAM ELEMENT NUMBER

6. AUTHOR(S)
Kody Varahramyan, Ph.D.

20040112 023

7. PERFORMING ORGANIZATION NAME(S) AND ADDRESS(ES)
Institute for Micromanufacturing
Louisiana Tech University
911 Hergot Avenue
Ruston, LA 71270

8. PERFORMING ORGANIZATION REPORT NUMBER
DAAD-19-02-1-0338

9. SPONSORING/MONITORING AGENCY NAME(S) AND ADDRESS(ES)
U.S. Army Research Office
P. O. Box 12211
Research Triangle Park, NC 27709-2211

10. SPONSOR/MONITOR'S ACRONYM(S)

11. SPONSOR/MONITOR'S REPORT NUMBER(S)
44365-MS-

12. DISTRIBUTION/AVAILABILITY STATEMENT

13. SUPPLEMENTARY NOTES
The views and/or findings contained in this report are those if the author(s) and should not be construed as an official Department of the Army position, unless so designated by other documentations.

14. ABSTRACT
This constitutes the final report for the project, initiated on August 1, 2002, on New Technologies for Polymer and Bio-Optic Systems for Broad Military and Civilian Applications. A mid-term report for this project was also submitted in January 2003. The overall project has consisted of three individual projects for the realization of new technologies for polymer and bio-optic systems for broad military and civilian applications. Specifically, the three projects have been defined as: Project 1, Project 2, Project 3. The senior investigators carrying out the work described in this report are Dr. Kody Varahramyan, Dr. Tianhong Cui, Dr. Alfred Gunasekaran, and Mr. Ji Fang. These investigators are associated with the Institute for Micromanufacturing at Louisiana Tech University. The team is headed by Dr. Kody Varahramyan, the Director of the Institute, and the Principal Investigator (PI) of this work. Moreover, the overall management plan consisted of Drs. Varahramyan, Cui, and Gunasekaran with Mr. Fang overseeing Projects 1, 2, and 3, respectively, and Dr. Varahramyan heading and coordinating this management team.

15. SUBJECT TERMS

16. SECURITY CLASSIFICATION OF:

a. REPORT	b. ABSTRACT	c. THIS PAGE
Unclassified	Unclassified	Unclassified

17. LIMITATION OF ABSTRACT

18. NUMBER OF PAGES

19a. NAME OF RESPONSIBLE PERSON
Kody Varahramyan

19b. TELEPHONE NUMBER (Include area code)
318-257-5107

Standard Form 298 (Rev. 8/98)
Prescribed by ANSI Std. Z39.18

New Technologies for Polymer and Bio-Optic Systems for Broad Military and Civilian Applications

Final Report

Submitted to DARPA

Dr. Leonard J. Buckley
DARPA/DSO
3701 North Fairfax Drive
Arlington, VA 22203-1714

and

Dr. John Prater
Army Research Office
P.O. Box 12211
4300 South Miami Blvd.
Durham, NC 27709-2211

by

Dr. Kody Varahramyan, Director
Institute for Micromanufacturing
Louisiana Tech University
P.O. Box 10137, 911 Hergot Avenue, Ruston, LA 71272
Tel: (318) 257-5107, Fax: (318) 257-5104, Email: kody@coes.latech.edu

December 2003

Executive Summary

This constitutes the final report for the project, initiated on August 1, 2002, on New Technologies for Polymer and Bio-Optic Systems for Broad Military and Civilian Applications. A mid-term report for this project was also submitted in January 2003. The overall project has consisted of three individual projects for the realization of new technologies for polymer and bio-optic systems for broad military and civilian applications. Specifically, the three projects have been defined as:

- **Project 1: New Technologies for Realization of All-Polymer Microelectronic and Optoelectronic Systems**

- **Project 2: Ultra-Sensitive Polymer Tunneling Sensor Platform for Physical Sensing**

- **Project 3: Bio-Inspired Micro-Optical System with Dynamically Varying Refractive Index**

The final reports for Projects 1, 2, and 3 are provided in the following sections. The senior investigators carrying out the work described in this report are Dr. Kody Varahramyan, Dr. Tianhong Cui, Dr. Alfred Gunasekaran, and Mr. Ji Fang. These investigators are associated with the Institute for Micromanufacturing at Louisiana Tech University. The team is headed by Dr. Kody Varahramyan, the Director of the Institute, and the Principal Investigator (PI) of this work. Moreover, the overall management plan consisted of Drs. Varahramyan, Cui, and Gunasekaran with Mr. Fang overseeing Projects 1, 2, and 3, respectively, and Dr. Varahramyan heading and coordinating this management team.

Project 1

New Technologies for Realization of All-Polymer Microelectronic and Optoelectronic Systems

Executive Summary

Since the submission of the Semi-Annual Report in January 2003, the project on New Technologies for Realization of All-polymer Microelectronic and Optoelectronic Systems (Project 1) has been carried out in accordance with the project objectives and milestones. Details about the work conducted and the results obtained are provided in this section. Specially, the work presented is on the research and development efforts leading to the realization of polymeric thin film capacitors, organic field-effect transistors, polymeric p-channel junction field-effect transistors, and low voltage all-polymer field-effect transistors fabricated with inkjet printing technique.

Objective

The main objective of this project is to establish the enabling technologies for the realization of all-polymer microelectronic and optoelectronic systems for broad military and civilian applications. This is a revolutionary approach based on ink-jet printing technology, liquid embossing, conventional lithography technique and nano self-assembly for rapid-processing and making of ultra-inexpensive products. These products include all-polymer microelectronics, optoelectronics, and MEMS-based devices and systems.

The foundation of many modern military and civilian technologies is based on state-of-the-art microelectronic devices. The final goal of this research is to fabricate microelectronic devices based on the ink-jet printing technique combined with several other novel or conventional fabrication technologies. This technology is meant to be the low-cost solution for realizing microelectronic and optoelectronic type of products for a broad range of applications.

Project 1 Accomplishments

1. Polymeric Thin Film Capacitors

1.1 Introduction

Polymer materials are attracting more and more attention for applications in microelectronic devices due to their flexibility, lightweight, and low cost. The most important development for microelectronics application of polymers was the realization of conducting polymers. Since the first polymer-based transistor with polyacetylene as the active semiconductor was fabricated by Ebisawa et al. in 1983, there has been an increasing amount of research work done in the field of organic devices. In 1989, the first polymer Light Emitting Diode (LED)

with polyphenylene-vinylene (PPV) as the emissive layer was made by the University of Cambridge. In 1997, the first printed transistor in the world was developed at Lucent Technologies.

Ink-jet printing, lithography, thermal evaporation, reactive ion etching (RIE), hot embossing, self-assembly, and polymerization are the main technologies that may be used to fabricate polymer devices. Polymers, in addition to their applications in microelectronics, can also be applied in making sensors, actuators, artificial muscles, and electrically conducting textiles, among other things.

There are rare reports about all-polymer devices fabricated by UV lithographic techniques, especially for all-polymer thin film capacitors. In this work, the fabrication and characteristics of an all-polymer capacitor, using polypyrrole (PPy) and Poly (3,4-ethylenedioxythiophene) poly (styrenesulfonate) (PEDOT/PSS) as a semiconductor and a gate layer, are reported. Dielectric polymer, poly-vinylphenol (PVP), was applied as the insulator to the device. The all-polymer capacitor, analogous to Metal Oxide Semiconductor (MOS) capacitor, was fabricated by the conventional UV lithography technique. The fabricated device was measured and characterized electrically. The results are compared with the electrical behavior of analogous silicon-based MOS devices. The results demonstrate that the polymer device operates in a very similar fashion to its conventional MOS counterpart.

1.2 Experiments

The thin-film capacitor was fabricated by UV lithographic techniques. The device was made through the process outlined in Figure 1 (a)-(e). MOS-like structure was adopted, including three different polymer materials. P-type semiconducting polymer, polypyrrole (PPy), was used as the semiconductor. Conducting polymer, PEDOT/PSS (Baytron P from Bayer AG), was applied as the gate material. The dielectric layer was PVP insulation polymer.

| Gate (PEDOT/PSS) |
| Dielectric layer (PVP) |
| Semiconductor (PPy) |
| Si Substrate |

(a) Spin-coating three polymer materials

| Aluminum |
| Gate (PEDOT/PSS) |
| Dielectric layer (PVP) |
| Semiconductor (PPy) |
| Si Substrate |

(b) Aluminum deposition

| Photoresist |
| Aluminum |
| Gate (PEDOT/PSS) |
| Dielectric layer (PVP) |
| Semiconductor (PPy) |
| Si Substrate |

(c) Photoresist applying

| Photoresist |
| Aluminum |
| Gate (PEDOT/PSS) |
| Dielectric layer (PVP) |
| Semiconductor (PPy) |
| Si Substrate |

(d) Aluminum patterning

| Gate |
| Dielectric layer |
| Semiconductor |
| Si Substrate |

+ + + + + + + + +

Fig. 1 Polymer thin-film capacitor fabrication process

A silicon wafer with a layer of silicon dioxide was used as the substrate. Three layers of polymers, PPy, PVP and PEDOT/PSS from the bottom to the top, were spun coated on the wafer respectively. Each layer was baked at 100-105°C for 1-5 minutes before the next layer was spun coated. Then aluminum was deposited on top of the PEDOT/PSS by thermal evaporation. Aluminum, instead of photoresist (PR), was used as an etching mask because PR is difficult to remove selectively. Moreover, it was found that PVP can be dissolved in many organic solvents such as AZ300 (PR 1813 developer), ethyl alcohol, and isopropyl alcohol, etc. Even photoresist itself can dissolve PVP to some degree. Aluminum was also used to prevent polymer layers from being affected during the UV lithography. Finally the polymer capacitor was patterned with dry etching. Two minutes of reactive ion etching was enough to remove the PEDOT/PSS and PVP layers.

Though only basic lithographic techniques were applied, several issues needed to be considered and avoided. Moisture inside the polymer layers can cause polymer degradation. One method to solve this problem is to bake each layer completely dry after spin-coating step. The other way is to make the fabrication process continuous to prevent moisture from being introduced.

Spin-coating is the main fabrication approach. There are several advantages to spin-coating, such as fine structures and global planarization of the resulting film. However, problems still exist and affect the performance of the electronic devices. For example, gap-filling, multilevel structures and shrinkage may be introduced by spin-coating. The other issue related to the multilayer spin-coating is the interlayer mixing, occurring at the interface between two layers. This is due to the penetration of the solvents of the spin-coated polymer into a previously deposited polymer film. The function of the interlayer mixing can assist or confine the carrier transport between the two layers.

1.3 Electrical Characteristics

The thin-film capacitor was characterized in air with Keithley Test and Measurement Instrument. Keithley software provides comprehensive analysis for the measured and calculated parameters. There are two models for testing quasistatic and high frequency capacitance in the System 82 simultaneous C-V System with windows-based Metrics-ICS C-V software. Figures 2 and 3 show the electrical characteristics of the capacitor.

In Figure 2, the curve of quasistatic capacitance of the polymer capacitor is similar to that of a conventional silicon-based capacitor. The accumulation, depletion and inversion modes in the capacitor can be demonstrated through the capacitance-voltage relationship. The capacitance is given by the series capacitance of the insulator layer (C_i) and the depletion layer (C_d), and is given by

$$C = C_i C_d / (C_i + C_d)$$

The formation of the accumulation layer for negative bias voltage is illustrated in Figure 2, as the tested capacitance tends towards the capacitance of the insulating layer. The capacitance decreases as the bias voltage becomes more positive, showing the formation of the depletion layer. Inversion is caused by the accumulation of the minority carriers beneath the insulator.

The production of minority charge carriers is controlled by the thermal generation rate of electro-hole pairs. In order to obtain the onset of the inversion, the testing parameters need to be adjusted carefully to make the minority carriers capable to follow the probe signal and accumulate under the insulator.
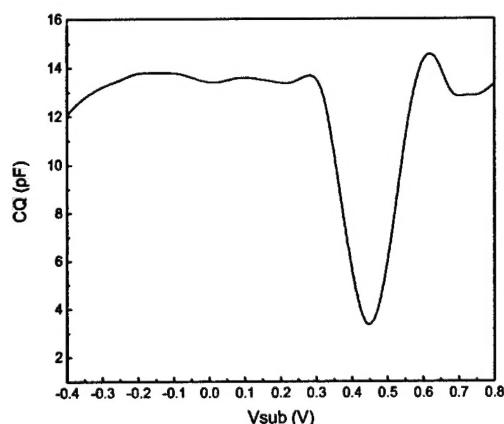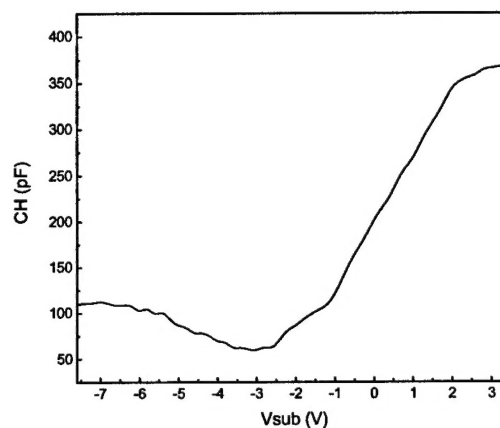

Fig. 2 Quasistatic capacitance curve

Fig. 3 High frequency capacitance curve

As shown in Figures 2 and 3, the capacitance-voltage measurements for the polymeric capacitors are very analogous to the ones displayed by conventional MOS capacitors.

1.4 Summary

An all-polymer MOS-like capacitor fabricated by UV lithographic technique was realized successfully. The conducting polymer as an active semiconducting component in this microelectronic device behaved in the similar fashion as the silicon-based counterpart in the accumulation, depletion, and inversion regions. UV lithographic technique is a simple and convenient approach to fabricate polymer-based microelectronic devices.

2. Organic Field-Effect Transistors with SiO_2 Nanoparticle Thin Film as Gate Dielectric

In this part, we report the fabrication of organic field-effect transistors (OFETs) using self-assembled SiO_2 as the gate dielectric material and pentacene as the semiconductor. The dielectric layer was self-assembled with 10 layers of SiO_2 nanoparticles, 45 nm in diameter, and its breakdown field was larger than 0.57 MV/cm. Being a low-cost and low-temperature process, the layer-by-layer (LbL) self-assembly approach used is particularly suitable for the OFET fabrication. The pentacene was thermally evaporated on the substrate under high vacuum at the room temperature. The fabricated transistor has a threshold voltage of 0.3 V, field-effect mobility of 0.05 cm^2/Vs, and subthreshold slope of 1.4 V/decade.

2.1. Introduction

Organic field-effect transistors (OFETs) have attracted great interest over the past decade due to their low cost, flexibility, and ease of fabrication for applications to large-area displays and low-end electronic devices, such as smart cards. To be useful for these applications, OFETs must provide substantial performance and processing advantages compared with the conventional FETs. The main parameters for device performance are charge carrier mobility, threshold voltage, and the on/off current ratio. Among the various OFETs based on organic semiconductors, pentacene OFETs were demonstrated to have the highest mobility and sufficiently high on/off current ratios up to date. Moreover, the low-cost and batch fabrication process is necessary to derive benefit from the various advantages of the OFETs. Furthermore, low-temperature processing is required, due to the thermal sensitivity of the organic materials. SiO_2 is the most widely used gate dielectric. However, the deposition of SiO_2 in the previous work was done either by the high-temperature thermal oxidation, or through LPCVD, PECVD, or sputtering, requiring complex equipments.

In recent years, the LbL nano-assembly process has gathered much attention in the fabrication of nanometer scale electronic devices, because it is a very easy and low-temperature process, requiring no expensive and complex equipments. In this work, a simple, low-temperature, and low-cost fabrication procedure for realization of pentacene OFETs has been developed. The self-assembly technique was used to deposit the gate dielectric layer formed with SiO_2 nanoparticles. The vertical dimension of the self-assembled thin film can be precisely controlled on the nanometer scale. Unlike the conventional process, the LbL self-assembly allows one to obtain the thin films for a semiconductor device, at a dramatically lower temperature, lower cost, and shorter processing time.

2.2 Experiments

Figure 5 shows the electrical characteristics of the Au/self-assembled SiO_2/heavily n^+-doped Si structure (illustrated as the inset of Figure 5). Positive bias is defined here as a negative voltage applied to the silicon substrate. The 10 layers of SiO_2 nanoparticles were self-assembled, and a gold electrode 80 nm thick was sputtered. Since the breakdown field was larger than 0.57 MV/cm from the analysis of electrical characteristics shown in Figure 5, it indicates that the self-assembled SiO_2 can be used as a gate dielectric instead of silicon dioxide based on thermal oxidation or other deposition techniques.
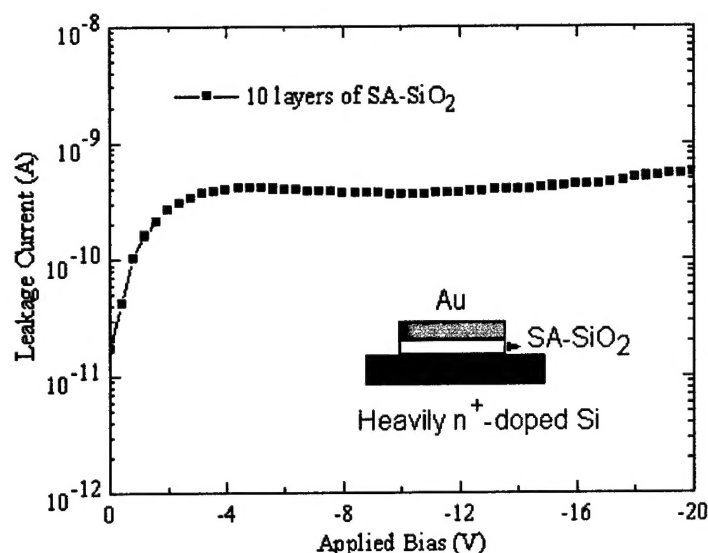
Figure 5 Gate leakage characteristic of the Au/self-assembled SiO₂/heavily-doped Si structure.
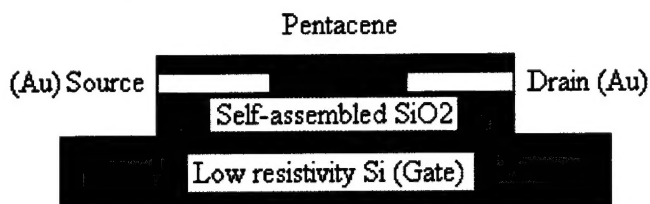

Figure 6 Schematic structure of pentacene FET with self-assembled SiO₂ as the gate dielectric.

For the pentacene OFETs with self-assembled SiO$_2$ (SA-SiO$_2$) as the gate dielectric, shown in Figure 6, a heavily n$^+$-doped silicon wafer (resistivity of about 0.001 Ω·cm) was used as the gate electrode and the substrate. Next, the dielectric layer was self-assembled with SiO$_2$ nanoparticles, 45 nm in diameter. Figure 7(a) shows the schematic diagram of the device with 4 layers of self-assembled SiO$_2$ nanoparticles, and Figure 7(b) illustrates the self-assembled SiO$_2$ thin film. After the cleaning of the silicon wafer surface and the H$_2$SO$_4$-H$_2$O$_2$ treatment for 1 hour, the silicon substrate was immersed into a 50 ml poly(dimethyldiallylammonium chloride) (PDDA) solution for 20 minutes. Following that, it was rinsed in DI water for 1 minute, and dried by a nitrogen flow. It was then immersed in a 50 ml polystyrene (PSS) solution for 10 minutes, rinsed and dried as in the previous step. Next, the immersion into PDDA was repeated for 10 minutes. The sequence was done as {PDDA (20 minutes) + [PSS (10 minutes) + PDDA (10 minutes)]₂}, i.e. dipping in PSS and PDDA were repeated after the initial three steps. The intermediate rinsing and drying are necessary. Thus up to date the outermost layer was positively charged PDDA. After the precursor mutilayers, the substrate was immersed in 50 ml diluted SiO$_2$ (45 nm in diameter) colloidal dispersions for 5 minutes, rinsed and dried, followed by another cycle of PDDA (10 minutes). Therefore the complete sequence of adsorption is {PDDA (20 minutes) + [PSS (10 minutes) + PDDA (10 minutes)]₂} + [SiO$_2$ (5 minutes) + PDDA (10 minutes)]₁₀.

PDDA
SiO$_2$
PDDA
SiO$_2$
PDDA
SiO$_2$
PDDA
SiO$_2$
(PDDA/PSS)$_2$+PDDA
Substrate
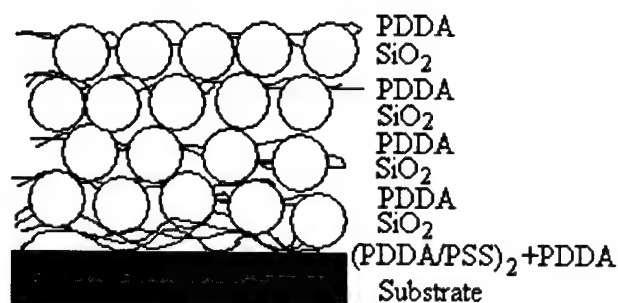
(a)
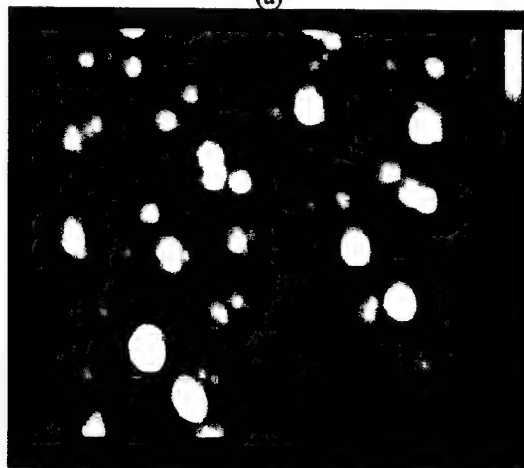
(b)

Figure 7 (a) Schematic diagram of self-assembly of SiO$_2$ nanoparticles on a silicon substrate,
(b) AFM image of the nano-assembled SiO$_2$ nanoparticles 45 nm in diameter.

After finishing the self-assembly of SiO$_2$ layers as the gate dielectric, a layer of Au 80 nm thick was sputtered on top of gate dielectric, and followed by patterning to form the source and the drain electrodes, as shown in the Figure 6. Finally, the pentacene OFETs were completed with the deposition of a layer of pentacene about 200 nm thick as the organic semiconductor. Pentacene was thermally evaporated through a shadow mask with a slow deposition rate and a working pressure of 6×10^{-7} Torr. The pentacene material is commercially available from Aldrich Chemical (98%), and used without performing any further purification process. During the evaporation of pentacene, the substrate was kept at room temperature. With the purification of the pentacene material and the control of the substrate temperature during the evaporation as described in the previous work, the electrical characteristics of the fabricated FETs could be further improved as expected. The electrical characteristics of the fabricated FET were measured with Keithley SMU236 and 238 source measurement units in the ambient atmosphere at room temperature.

2.3 Results and Discussions

By assuming that the MOS theory of the traditional MOSFET is still effective for the organic FETs, the drain current in the linear region and the saturation region can be expressed by the following equations:

$$I_D = \frac{W\mu_{FET}C_{ox}}{L}V_{DS}(V_{GS} - V_{th}) \qquad (1)$$

$$I_{Dsat} = \frac{W\mu_{FET}C_{ox}}{2L}(V_{GS} - V_{th})^2 \qquad (2)$$

where W and L are the channel width and length, respectively, μ_{FET} is the field-effect mobility of the charge carrier in the pentacene channel, $C_{ox} = \varepsilon_{ox}/d_{ox}$ is the gate dielectric capacitance per unit area (ε_{ox} and d_{ox} are the dielectric constant and the thickness of the self-assembled SiO_2 gate dielectric layer, respectively), and V_{GS}, V_{DS}, V_{th} are the gate- source voltage, the drain-source voltage, and the threshold voltage, respectively.

A QCM (quartz crystal measurement) equipment was used to monitor the LBL assembly process of SiO_2 nanoparticles. It is a microbalance suitable to measure the tiny mass and thickness adsorbed on the quartz surface. It senses the resonance frequency directly with a high sensitivity. The following relationship is obtained between the adsorbed mass M (g) and the frequency shift ΔF (Hz) by taking into account the characteristics of quartz resonators used:

$$\Delta F = -1.83 \times 10^8 \, M/A \quad (3)$$

where A is the apparent area of the quartz microbalance placed between two QCM electrodes. This is 0.16 ± 0.01 cm^2 in our system. The thickness of the alternative layer corresponding to the QCM frequency shift was determined by the observation of the film cross-section SEM images of the resonators coated with silicon/polycation films, which gives the following relationship with ±5 % error:

$$d \, (nm) = 0.022 \, (-\Delta F) \, (Hz) \qquad (4)$$

The accumulative frequency shift for 10 layer silica nanoparticles obtained is 16023 Hz. Based on the equation (4), the total thickness of the self-assembled SiO_2 dielectric layer was calculated as 353 nm.

It was found the dielectric constant was higher than the thermal SiO_2. The volume composition of the SiO_2/PDDA film is 70 % SiO_2, 10 % polycation, and 20 % air-filled pores. These pores are formed by the closely packed 45 nm SiO_2 and have a typical dimension of 15 nm. The dielectric constant of the multiplayer was higher due to about 30% of inclusions of other materials, such as polyion layers. If the layer of SiO_2 was produced by the conventional thermal oxidation, the dielectric constant would be 3.9. The dielectric constant of the multiplayers formed by the LBL nanoassembly is about 6.

The I_D-V_{DS} drain characteristics of a typical pentacene FET fabricated with the self-assembled SiO_2 as the gate dielectric are shown in Fig. 8. This device has a channel length and width of 25 and 500 μm, respectively, and a gate dielectric layer 353 nm thick. In the pentacene OFETs, the current between the drain and the source I_D is controlled by the applied gate-source voltage V_{GS}. Since pentacene is a p-type polymeric semiconductor, the pentacene FETs generally operate in the accumulation mode with a negative bias on the drain-source and the gate-source electrodes. The negative gate bias will enlarge the conduction channel due to the formation of a hole accumulation layer. Thus, the conductivity of the channel between the drain and the source is increased with the negative gate bias.

Fig. 9 shows the measured gate transfer characteristics of the same pentacene OFET described above. The field-effect mobility is generally determined in the region where the drain current saturates according to the equation (2). From the slope of the square root of the saturation current as a function of the gate voltage as shown in Figure 5, a field-effect mobility of 0.05 cm^2/Vs was extracted at the small V_{DS} of -3 V. Through linearly extrapolating the curve to the V_{GS} axis, the threshold voltage V_{th} can be extracted to be 0.3 V. When the V_{DS} of -3 V was applied and the gate voltage were swept from 2 V to -10 V, the subthreshold slope was obtained to be about 1.4 V/decade, and the on/off current ratio was about 10^3.
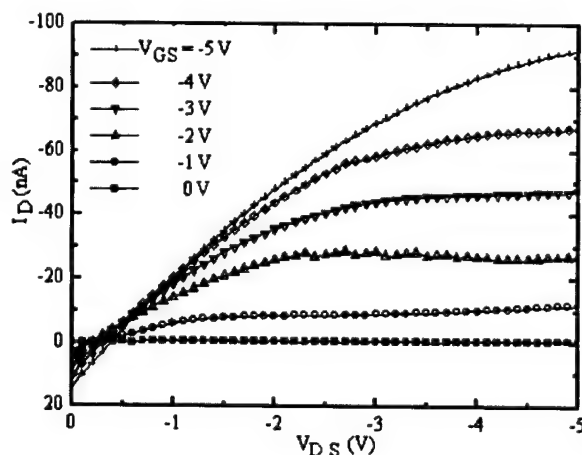

Figure 8 Drain characteristics of pentacene FET on SA-SiO_2 with the
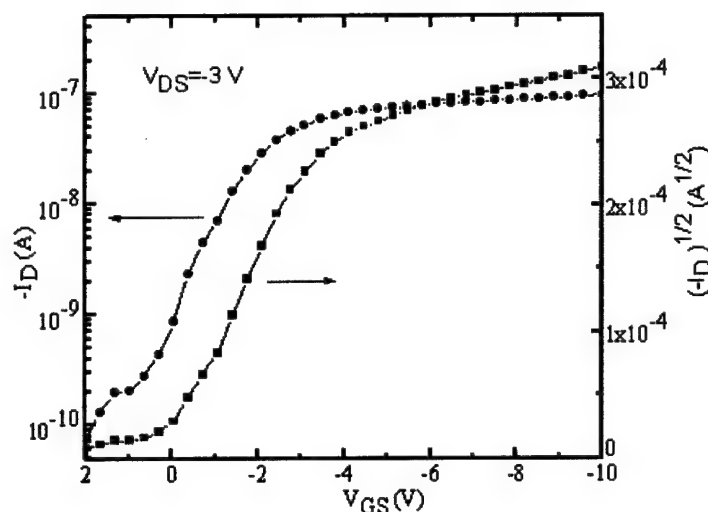channel length and width of 25 μm and 500 μm, respectively.

Figure 9 Gate characteristics of pentacene FET on SA-SiO$_2$ with the
channel length and width of 25 μm and 500 μm, respectively.

2.4 Summary

In summary, we have demonstrated the low-cost and low-temperature fabrication process of organic field-effect transistors (OFETs) using the self-assembled SiO$_2$ as the gate dielectric material and pentacene as the semiconductor. 10 layers of SiO$_2$ nanoparticles, 45 nm in diameter were self-assembled to form the dielectric layer, which has a breakdown field larger than 0.57 MV/cm. The fabricated transistors have a threshold voltage of 0.3 V, a field-effect mobility of 0.05 cm^2/Vs, and an on/off current ratio of about 10^3. Due to the low-cost and low-temperature advantages of the fabrication process, the self-assembly technique is particularly suitable for the fabrication of OFETs.

3. Polymeric P-channel Junction Field-Effect Transistors

3.1 Introduction

In this work, fabrication and characterization of a polymer junction field effect transistor (JFET), using poly (3,4-ethylenedioxythiophene) poly (styrenesulfonate) (PEDT/PSS) as the channel, and poly(2,5-hexyloxy p-phenylene cyanovinylene) (CNPPV) as the gate layer, are reported. The all-polymer JFET was fabricated by the conventional UV lithography techniques. The measured electrical characteristics demonstrate that the device operates in a very similar fashion to its conventional counterparts.

3.2. Experiments

The JFET is a device providing a controlled transport of majority carriers through a semiconductor, and its key part is a nonlinear resistor fabricated with a doped semiconductor material. To be specific, we refer to it as a p-channel polymeric JFET because the conducting

material is a p-type semiconductor polymer material, poly (3,4-ethylenedioxythiophene) poly (styrenesulfonate) (PEDT/PSS) (Baytron P from Bayer AG) in this work. The gate material is an n-type polymer, poly (2,5-hexyloxy p-phenylene cyanovinylene) (CNPPV). The device was fabricated through the processes outlined in Fig. 10 (a)-(d).
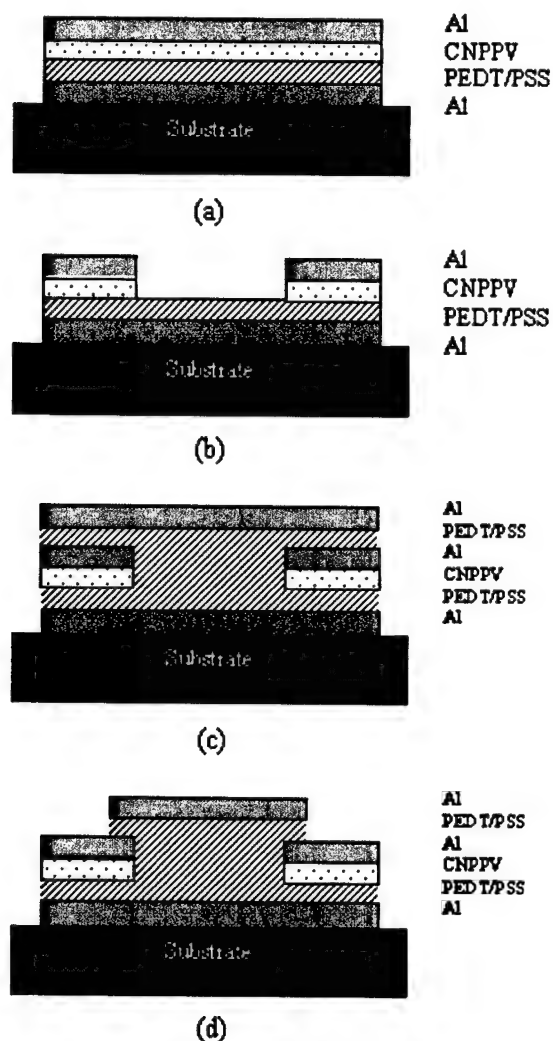
Al
CNPPV
PEDT/PSS
Al

(a)

Al
CNPPV
PEDT/PSS
Al

(b)

Al
PED T/P SS
Al
CNPPV
PED T/P SS
Al

(c)

Al
PED T/P SS
Al
CNPPV
PED T/P SS
Al

(d)

Figure 10. Fabrication procedures of JFET

First, a silicon dioxide wafer covered with a layer of evaporated 0.15µm aluminum (Al) was used as the substrate, which can also be glass or polymeric material. Two layers of polymers, 1µm PEDOT/PSS and 1µm CNPPV, were spun on the substrate at the bottom and on the top, respectively. Each layer was baked at 100-105°C for 1-5 minutes before the next layer was spun. Next, 0.15µm Al was deposited on top of the CNPPV by thermal evaporation. Al, instead of photoresist (PR), was used as an etching mask layer because PR is difficult to remove selectively. After patterning of Al and Reactive Ion Etching (RIE) of CNPPV, a layer of PEDT/PSS was spun on top of the pattern to fill the channel region between two CNPPV gates,

followed by another 0.15µm thick Al film evaporated on top of the PEDT/PSS. Finally, the JFET structures, as shown in Fig. 11, were built after wet etching of Al and RIE of the polymer.

Though only basic lithographic techniques were applied, several issues need to be considered and avoided. One needs to control well the time to etch CNPPV and keep the PEDT/PSS from being etched. It normally takes 1min to remove CNPPV at the condition given in Table 1.
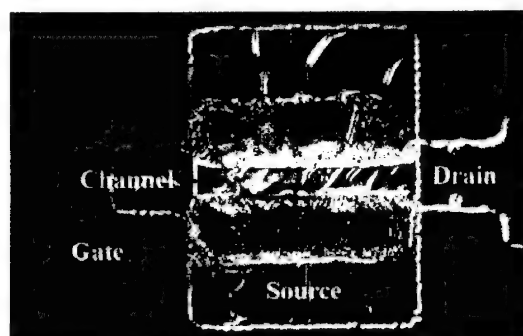

Figure 11. JFET on the silicon substrate

Table 1. Conditions for reactive ion etching of CNPPV

Oxygen	Power	Pressure
20sccm	200w	<10mToor

Moisture inside the polymer layers can cause the polymer degradation. One approach to solve this problem is to bake and dry each layer completely prior to the fabrication of the following layers. The other way is to make the fabrication process step by step continuously to prevent moisture from the environment. Moreover, the device also needs to be baked after a long period of time between two fabrication steps. Compared with p-type polymers, the degradation of n-type polymers is much easier.

3.3. Results and Analysis

Drain and transconductance characterization
The p-channel polymeric JFET was characterized in air ambient with Keithley Test and Measurement Instrument. Keithley software provides comprehensive analysis to the measured and calculated parameters. Fig. 12 shows the schematic structure of the JFET, which can be explained by the mechanism of conventional JFETs.
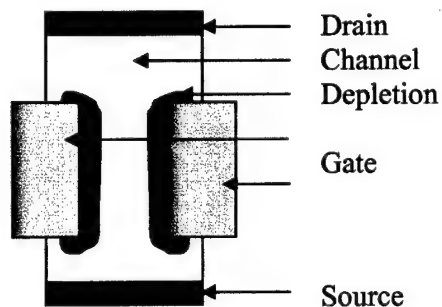

Figure 12. JFET structure

The JFET makes use of the fact that a very strong electric field exists across a pn junction, and the electric field affects charge carriers in the junction region. The gate electrodes shown in the Fig. 12 are formed as pn junctions, with the channel forming between the two junctions. The same positive voltage (V_{GS}) was applied onto the two gates. In the meantime, external voltages were added between source and drain (V_{DS}). With increasing V_{DS}, the current between the source and the drain (I_{DS}) will go through the linear region and the saturation region. The width of the depletion region increases with increasing the reverse bias V_{GS}, thus extending into the channel, further increasing the channel resistance and shrinking the channel width.

The conductivity of JFET carrier-transport in the channel is modified by the electric field associated with the depletion region of a reverse-biased junction extended into the channel. The capability of the channel to carry current is highest when the control junction has zero bias and decreases with increasing reverse bias, as shown in the Fig. 13. Therefore, the polymer JFET, operated at depletion-mode, inherently is a normally-on device, which is turned on with no control exerted, and is turned off with increasing reverse bias. The transconductance characteristic is plotted in Fig. 14.
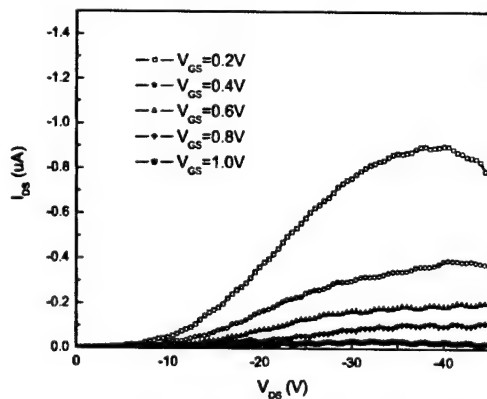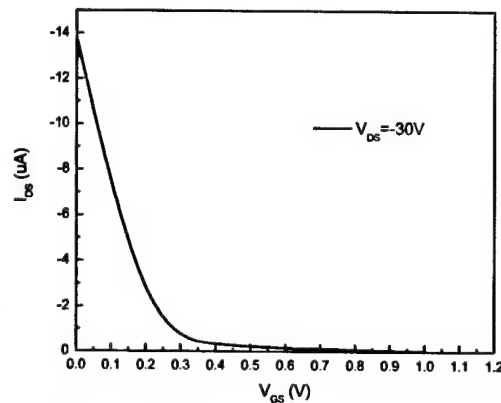
Figure 13. Drain characteristics
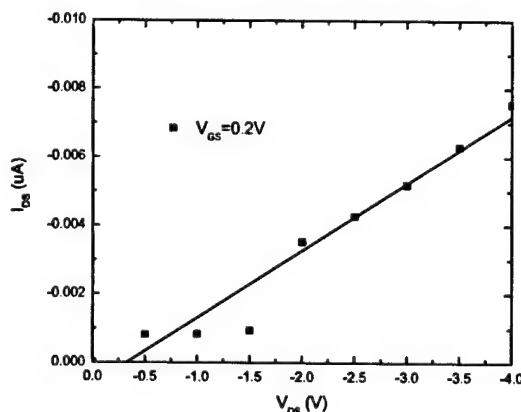
Figure 14. Transconductance characteristics

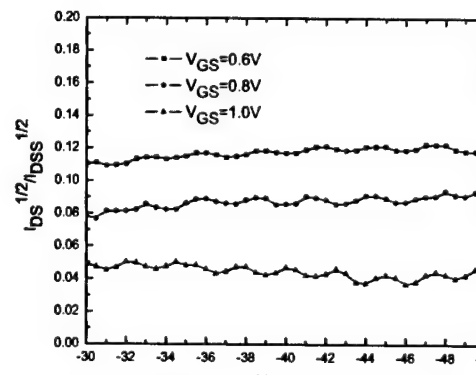Figure 15. I_{DS} independent of V_{DS} at saturation region   Figure 16. Forward-biased I-V curve of the junction

In the linear region, one can obtain the relationship among I_{DS}, V_{DS} and V_{GS} as

$$I_{DS} = G_0 (1 - \sqrt{\frac{\psi_0 - V_{GS}}{V_{PO}}}) V_{DS} \qquad (1)$$

Here, G_0 is the channel conductance without any depletion layers, ψ_0 is the built-in potential and V_{PO} is the sum of the pinch off voltage V_P and the ψ_0.

$$G_0 = \frac{2qaWu_p N_a}{L} \qquad (2)$$

L is the channel length, W is the channel width and a is the half of the channel height. The drain current is proportional to the drain voltage at small V_{DS} as shown in Fig. 15.

From the Eq. (1), we know the slope is K,

$$K = G_0 (1 - \sqrt{\frac{\psi_0 - V_{GS}}{V_{PO}}}) = \frac{2qaWu_p N_a}{L} (1 - \sqrt{\frac{\psi_0 - V_{GS}}{V_{PO}}}) \qquad (3)$$

Which is a parameter relating to the mobility of the conducting polymer channel if the dimension and material were set.

In saturation region, the relationship between I_{DS} and V_{GS} can be expressed as

$$I_{DS} = I_{DSS} (1 - \frac{V_{GS}}{V_P})^2 \qquad (4)$$

Where V_P is the pinch-off voltage, and I_{DSS} denotes the drain saturation current at zero gate voltage. I_{DSS} was 13.8uA from testing when V_{GS} is 0V. From the drain testing curves and Eq. (4), we derived the following Fig. 16, and it shows that the I_{DS} is independent of the V_{DS}, and it was determined by the V_{GS}. Also, we can obtain the V_P values at each V_{GS} condition.

PN Junction
To characterize the pn junction at the gate region, the I-V characteristics of the gate junction was tested, as shown in the Figs 17 and 18. The breakdown voltage and rectification ratio of the PEDT/PSS/CNPPV junction diode are about 10 V and 2.89, respectively.
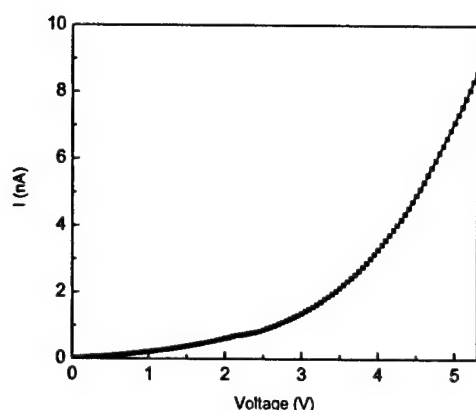
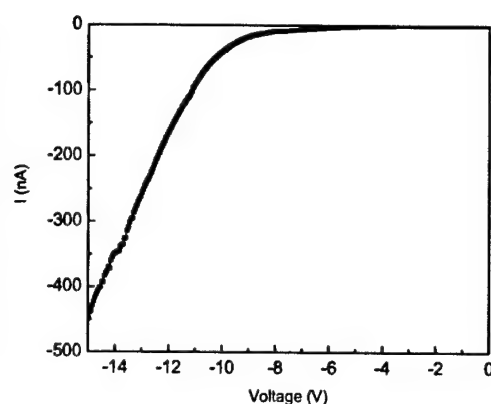Figure 17. Forward-biased I-V curve

Figure 18. Reverse-biased I-V curve

Al/PEDT/PSS Interface

It has been reported that the Al and PEDT/PSS can form Schottky diode. Here we test the interface of Al and PEDT/PSS and found that it has the diode feature as shown in Figs. 19 and 20. for forward and reverse biasing. The breakdown voltage and rectification ratio of the Al/PEDT/PSS junction diode are about 22 V and 3.1, respectively.
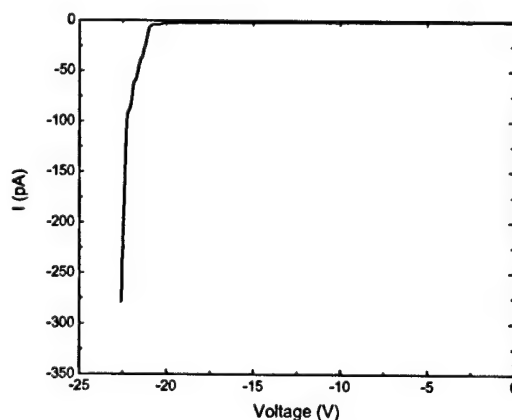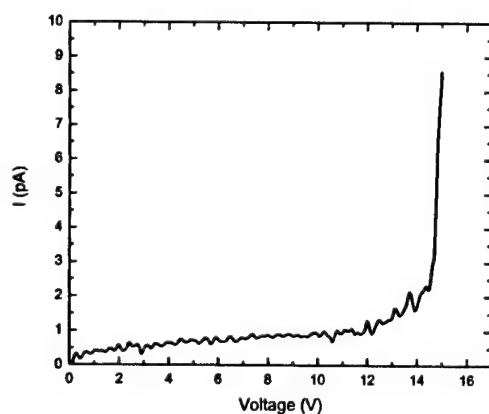

Figure 19. Forward bias of Al/PEDT/PSS interface

Figure 20. Reverse bias of Al/PEDT/PSS interface

Polymer JFET and Conventional JFET

Polymer electronic devices are currently in their infancy, like semiconductor devices when they first appeared decades ago. As a result, current performance of these devices is hardly comparable to the state-of-the-art semiconductor devices. Though it is difficult to make a comparison, we still found some similarities and differences between the two types of JFETs that are listed in Table 2.

Table 2. Comparisons between polymer JFET and inorganic JFET

Similarity		Polymer-JFET	Inorganic JFET
		working mechanism	
		analyze methods	
		Polymer works in depletion-mode	
Difference	Fabrication	UV lithography (Experimental stage)	The state-of-the-art industry fabrication
	Structure	Vertical structure	Lateral structure
	Materials	Conducting polymers	Inorganic semiconductors, such GaAs
	Performance	Needs to further improved with the immerging of novel polymer materials	Good.
	Applications	Follower circuit in the experimental stage. No commercial products.	Commercial products. High speed, high power circuits.

Perhaps, with the improvement in polymer materials' properties, such as conductivity and mobility, the performance of the polymer microelectronics devices could compete with conventional ones.

3.5. Conclusions

A p-channel polymeric JFET fabricated with UV lithography techniques was successfully realized. The conducting polymer is the active semiconducting component in this microelectronic device, which is found to behave in similar fashion as the inorganic semiconductor counterpart. This work opens a new way to realize JFETs, with broad applications, such as switches and amplifiers.

4. Low Voltage All-polymer Field Effect Transistor by Inkjet Printing Technique

The all-polymer field effect transistor (FET) fabricated with all-inkjet printing technique is presented in this section. Poly(3,4-ethylenedioxythiophene) works as the source/drain/gate electrode material due to its good conductivity. Polypyrrole acts as the semiconducting layer. Polyvinylpyrrolidone K60, a dielectric constant of 60, operates as the dielectric material. All the polymers are diluted with deionized water, and can be printed with a piezoelectric inkjet printer. The device functions at the depletion mode with the threshold voltage of -4.3 V, much smaller than the reported inkjet printed polymer transistors by other research groups. The Polymer FET has a field-effect mobility of 0.1 cm^2/Vs, on/off ratio of 2.9×10^3, and subthreshold slope of 2.81 V/decade.

4.1. Introduction

A variety of approaches have been used to deposit conducting polymer films or organic semiconductors based on the nature of materials. The various techniques commonly employed include solution-processed deposition such as spin coating and printing, electro-polymerization,

and vacuum evaporation. Other techniques (soft lithography, self-assembly, and langmuir-blodgett) have also been applied to the fabrication of conducting polymers. Various printing techniques, including screen-printing, micro-contact printing, and inkjet printing (IJP), are catching more and more attention. Among these printing techniques, IJP is the most promising because polymer devices fabricated by IJP technique have the advantages of simplicity of fabrication, compatibility with various substrates, availability of non-contact, no-mask patterning, and reduction in the amount of materials wasted during processing.

For the inkjet printed all-polymer FET, only the gate (G), source (S), and drain (D) electrodes were printed, while other components such as dielectrics and active layers were still deposited by spin coating and patterned by lithography. The inkjet printed insulating layer of the polymer FET have not been reported, mainly because it is difficult to print out the insulating polymers, which are insoluble or soluble but easy to clog the printer nozzles. Our approach to overcome this problem is to use a water-dissolved insulating polymer solution that can be easily printed out without clogging the nozzles. Since the charge in polymer FET is proportional to both the dielectric constant and the gate voltage, the material with a higher dielectric constant allows the necessary charge to accumulate at much lower voltages.
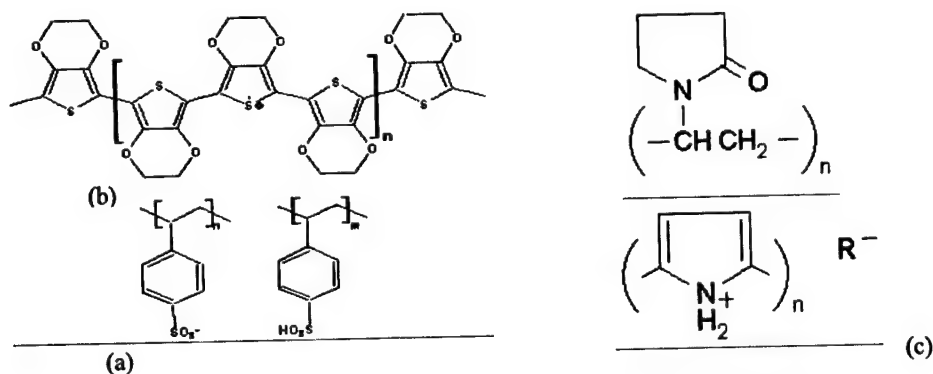

Figure 21: Chemical structures. (a) PEDOT/PSS, (b) PVP-K60, (c) PPy

Polyvinylpyrrolidone K60 (PVP-K60), a water-soluble insulating polymer with a high dielectric constant of 60, meets the above requirements. Combining the inkjet printed poly(3,4-ethylenedioxythiophene) doped with poly(styrene sulfonic acid) (PEDOT/PSS) as the source, drain, and gate electrodes and polypyrrole (PPy) as the active layer, the all-polymer transistors with the all-inkjet printing technique have been fabricated and characterized successfully. As far as we know, this is the first report on a low voltage all-polymer FET with the all-inkjet printing technique.

4.2 Device Fabrication

The inkjet printer employed in the device fabrication is a piezoelectric inkjet printer with an accuracy of ±5 μm (from Microdrop Company). Selection of suitable polymer solutions for inkjet printing is very critical because the solutions have to satisfy the compatibility of inkjet heads and the reproducibility of drop dynamics. The inkjet head compatibility means that a solvent will not block the head nozzles during printing, and the drop dynamics reproducibility

relates to properties of the material including correct viscosity and surface energy to allow the reproducible forming of droplets with the same droplet volume and direction. To satisfy these requirements, we select the polymers dissolved in deionized water. After changing the ratio of polymer to water, the solution can be optimized for printing stably without clogging the nozzles. Figure 21 shows the chemical structure of the conducting polymer PEDOT/PSS, doped semiconducting polymer PPy, and the insulating polymer PVP-K60 used in our FET fabrication.

The schematic of the printed all-polymer FET device is shown in Figure 22. First, a layer of aluminum 2000 Å thick was deposited on the silicon dioxide wafer and patterned with UV lithography to form the contact electrodes. Next, PEDOT/PSS with a concentration of 10% was printed to form the gate electrode. Following that, the 15% of PVP-K60 dispersion in water was dispensed onto the gate electrode. The third printing step is to dispense PPy dissolved in water onto PVP-K60 to form the active layer. Finally, the top source and drain electrodes made of PEDOT/PSS were printed under the same condition as printing the gate electrode. The channel length and width of the polymer FET are 100 μm and 1200 μm, respectively.
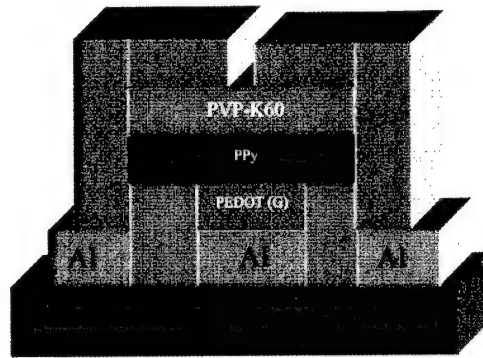

Figure 22: Schematic of the all-polymer FET.

4.3 Results and Discussions

For FETs, the drain current I_D increases linearly with the drain voltage V_D at low V_D regime (linear regime), and the relationship is expressed as

$$I_D = \frac{WC_j\mu}{L}(V_G - V_T - \frac{V_D}{2})V_D \tag{1}$$

where L is the channel length, W is the channel width, C_j is the capacitance per unit area of the insulating layer, V_T is the threshold voltage, V_G is the gate voltage, and μ is the field effect mobility, which can be calculated in the linear regime from the transconductance given by

$$g_m = \frac{\partial I_D}{\partial V_G}\bigg|_{V_D=const.} = \frac{WC_i}{L}\mu V_D \tag{2}$$

When $-V_D > -(V_G - V_T)$, I_D tends to saturate (saturation regime) due to the pinch-off of the accumulation layer, and I_D is modeled by

$$I_D = \frac{WC_j\mu}{2L}(V_G - V_T)^2 \qquad (3)$$

The accumulated charge per unit area is simply V_gC_j. Since $Cj=\varepsilon_0\varepsilon_r/d$, we can see that a polymer with a higher dielectric constant can allow the charge to accumulate at much lower voltages.

The characteristics of I_D versus V_D and I_D versus V_G of the all-polymer FETs fabricated with all-inkjet printing technique are shown in Figure 23a and Figure 23b, respectively. Figure 23a shows that the device works in the linear region when the drain voltage is between -1.5 V and -2.8 V, and approaches to the saturation regime when V_D is larger than -2.8 V. For the region when V_D is below -1.5 V, almost no current passes through the channel. This is mainly due to the rectifying barrier between the Al electrode and the PEDOT S/D electrodes. Since the work function of Al (4.3 eV) is smaller than that of PEDOT (5.2 eV), a rectifying barrier (schottky barrier) will form at the Al/PEDOT interface. Therefore an external potential is needed to overcome the schottky barrier before the current can go through the channel. Extracted from Figure 23b, the threshold voltage is approximately -4.3 V. The on/off ratio is defined at a given negative drain bias as the ratio of the current in a transistor at its "on" state to the current at its "off" state, and can be obtained from Figure 3b at 2.9×10^3. The calculated mobility from Equation (2) is 0.1 cm^2/Vs at $V_D = -3.5$ V. The subthreshold slop is 2.81 V/decade.

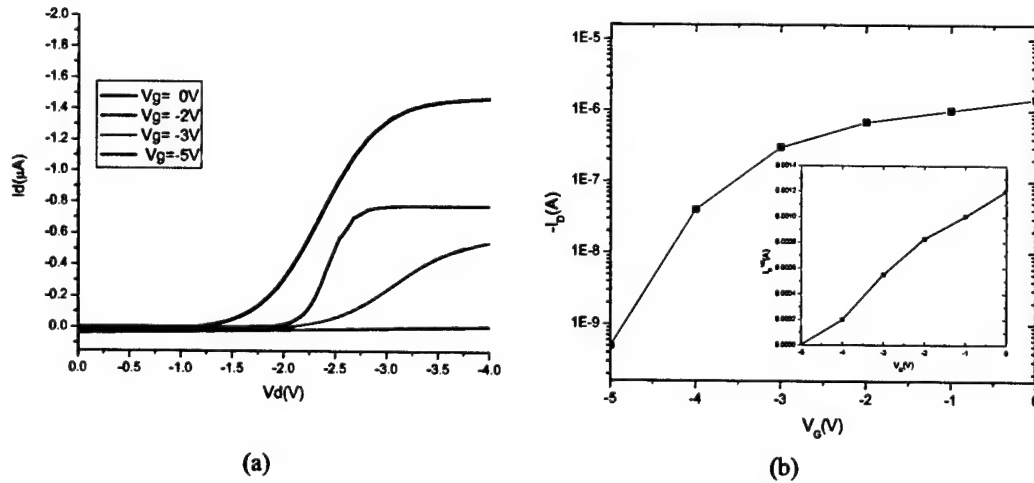(a)   (b)

Figure 23: (a) the I_d verse V_d characteristic of the all-polymer FET,
(b) the transfer characteristic of the all-polymer FET.

One "abnormal" phenomenon of this polymer FET is that the gate voltage sequence is reversed comparing with the p-channel polymer FET reported by other research groups. The device works as a normally-on FET at zero gate voltage, and falls into "off" state when the gate voltage is negatively increased. This is contrary to the conventional definition of "on" state where $V_G = V_D < 0$ V and "off" state where $V_G = 0$ V when $V_D < 0$ V. To understand this "abnormal"

electrical characteristic of the all-polymer FET, we should refer to the device structure, the active material, and the charge transport in the polymer FET. For the p-type semiconducting polymer PPy, there are two types of positive charges in the channel region, the doping component and the field effect component. Since the PPy employed in this FET is doped with toluenesulfonic acid, its charge characteristics will be improved by the dopant anion, enhancing the doping component of charges during the transport. The thickness of inkjet-printed active layer of PPy is 353.20 nm measured with Roughness Surface Tester (From Veeco Company). It is much thicker than the conventional polymer FET in which the active layers were less than 100 nm with evaporation or spin coating. Due to the larger thickness of the active layer, most of the charge carriers (holes) will transport at the channel surface region, as shown in Figure 24a. At zero gate voltage, the holes from the doping component in the PPy will transport from source to drain electrode under negative V_D when V_D is larger than the schottky barrier between the PEDOT/PSS and the Al electrode. When the gate voltage is negatively increased, the field effect charge will be generated at the PPy/PVP-K60 interface due to the band bending in the semiconductor. In the meantime, the positive doping charges transport at the surface region will be attracted to the bulk region by the negative gate bias, as shown in Figure 24b. This will result in less charge carriers at the top surface region, and hence reduce the drain current.
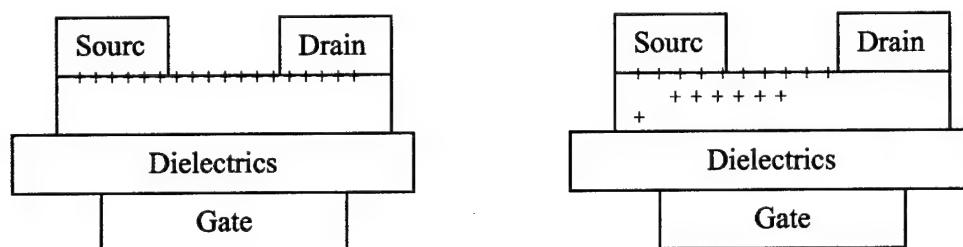

Figure 24: (a) The distribution of charge carriers at zero gate voltage,
(b) the distribution of charge carriers when gate voltage negatively increased.

To confirm the above analysis of the channel formation and to verify how the dielectric material affect the operation voltage of polymer FETs, we also fabricated the polymer FET with the same structure and materials, except that the dielectric material is replaced with another commonly used polymer dielectric, poly (4-vinylphonel) (PVPh), with a dielectric constant of 3.6. From Figure 25, this device with the same active material PPy by the IJP technique works at the operation voltage negatively larger than –15 V. The device also works at "on" state at zero gate voltage and falls into "off" state at higher negative gate voltage. Therefore the polymer with the higher dielectric constant plays a key role in the low operation voltage of all-polymer FETs.
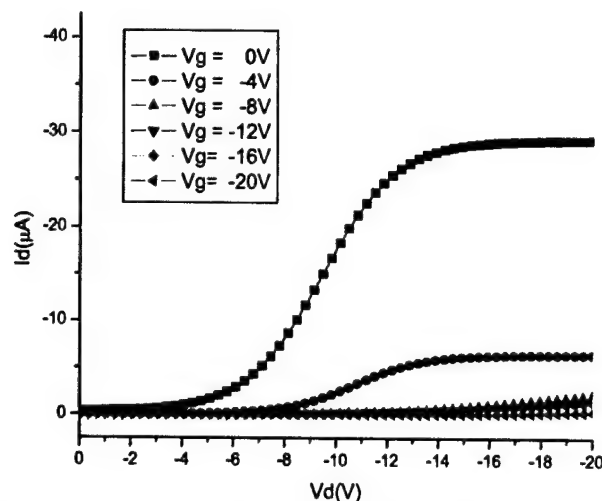
Figure 25: The I_d verse V_d characteristic of a polymer FET with PVPh as the dielectric material.

4.4 Summary

We have demonstrated an all-polymer field effect transistor using all-inkjet printing technique. The threshold voltage of the polymer FET can be as low as –4.3 V using a polymer named PVP-K60 with a high dielectric constant of 60. The higher the polymer's dielectric constant, the lower the operation voltage of the polymer FET with the same structures will be. The thickness of the active layer in the polymer FET can affect the channel region, and thus change the operation mode of gate-field generated charges. Up to date, this is the first report of all-inkjet printed polymer FET with a low operation voltage. Our findings represent an important milestone and can make a great contribution to the fabrication of practical polymer microelectronic devices with the simple all-inkjet printing technique.

5. Project 1 Publications and Presentations

(1) Yuming Ai, Tianhong Cui, and Kody Varahramyan, "Thin Film Deposition of an N-type Organic Semiconductor by Ink-Jet Printing Technology", submitted to Thin Solid Films, 2003.

(2) Mo Zhu, Guirong Liang, Tianhong Cui, and Kody Varahramyan, "Depletion-mode n-channel organic field-effect transistors based on NTCDA", Solid State Electronics, Vol. 47, No. 10, 2003: 1605-1879.

(3) Yi Liu, Tianhong Cui, and Kody Varahramyan, "All-Polymer Capacitor Fabricated by All-inkjet Printing Technology", Solid State Electronics, Vol.47, No.9, 2003: 1543-1548.

(4) Tianhong Cui, Guirong Liang, Kody Varahramyan, "An Organic Poly(3,4-ethylenedioxythiophene) Field Effect Transistor Fabricated by Spin Coating and Reactive Ion Etching", IEEE Transactions on Electron Devices, Vol.50, No.5, May 2003: 1419-1422.

(5) Yuxin Liu, Tianhong Cui, Kody Varahramyan, "Fabrication and Characteristics of Polymeric Thin Film Capacitor", Solid State Electronics, Vol.47, No.5, 2003: 811-814.

(6) Bin Chen, Tianhong Cui, Yi Liu, and Kody Varahramyan, "All-Polymer RC Filters Fabricated by All-inkjet Printing Technique", Solid State Electronics, Vol.47, No.5, 2003: 841-847

(7) Guirong Liang, Tianhong Cui, Kody Varahramyan, "Electrical Characteristics of Diodes Fabricated with Organic Semiconductors", Microelectronic Engineering, Vol.65, No.3, 2003: 279-284.

(8) Guirong Liang, Tianhong Cui, Kody Varahramyan, "Fabrication and Electrical Characteristics of Polymer-based Schottky Diode", Solid State Electronics, Volume 47, No. 4, 2003: *691-694*.

(9) Guirong Liang, Tianhong Cui, and Kody Varahramyan, "Fabrication and Electrical Characteristics of Polymer-based Schottky Diode", the 10th Conference on Polymer Microelectronics, Wilmington, Delaware, 2002.

(10) Yuxin Liu, Tianhong Cui, Kody Varahramyan, "Fabrication and Characteristics of All-Polymer Thin Film Microelectronic Devices", the 10th Conference on Polymer Microelectronics, Wilmington, Delaware, 2002.

6. Project 1 Disclosures

(1) Tianhong Cui, Kody Varahramyan, and Guirong Liang, "All-polymer Vertical Field Effect Transistor", ROI 2002-06.

(2) Tianhong Cui, Kody Varahramyan, and Yuxin Liu,"Polymeric Junction Field Effect Transistor (JFET) and JFET-based Integrated Circuits (IC)", ROI 2003-11, March 2003.

(3) Tianhong Cui, Kody Varahramyan, and Guirong Liang, "Polymer Microelectronic Devices Based on Lithography Techniques", ROI2003-19, April 2003.

(4) Tianhong Cui, Kody Varahramyan, and Yi Liu, "Ink-jet Printed Polymer Microelectronic Devices", ROI2003-20, April 2003.

(5) Tianhong Cui, Kody Varahramyan, and Mo Zhu, "Depletion-mode n-channel organic field-effect transistors", ROI2003-21, April 2003.

Project 2

Ultra-Sensitive Polymer Tunneling Sensor Platform
for Physical Sensing

Executive Summary

Since the submission of the Semi-Annual Report in January 2003, the project on Ultra-Sensitive Polymer Tunneling Sensor Platform for Physical Sensing (Project 2) has been carried out in accordance with the project objectives and milestones. Details about the work conducted and the results obtained are provided in this section. Specially, the work presented is on the research and development efforts leading to the realization of polymer-based infrared sensor, modeling and design of polymer-based tunneling accelerometer, and polymeric magnetic field sensor based on nanocomposite magnetic thin films.

Objective

The proposed project addresses the military and civilian needs for highly effective infrared, vibration and/or other physical sensing products that are very sensitive and functional, while are also very small, light, and inexpensive. Products with these characteristics are highly needed for applications in the battlefield as well as daily civilian life. Combining micro-electro-mechanical systems (MEMS) technology with nanotechnology, the proposed project, will give a novel platform of polymeric sensors, aimed at satisfying the above sensor requirements. The sensors are tunneling-based, and their polymer microstructure will be monolithic/hybrid integrated with the control circuit to form the desired sensor platform. The work conducted has been focused on the design, simulation, fabrication and characterization of the novel ultrasensitive polymer-based tunneling sensor platform for physical sensing. Details about the work accomplished is provided below.

Project 2 Accomplishments

1. Polymer-based Infrared Sensor

This part of report describes a low-cost polymer-based tunneling infrared sensor fabricated with the hot embossing technique. This report presents the design, the fabrication, and the measurement of the infrared sensor. Electron tunneling transducer is used to detect the deflection of the membrane, which is caused by the variation of the infrared radiation. Due to the high sensitivity of the tunneling transduction mechanism, high performance infrared sensors can be conveniently fabricated. Polymethylmethacrylate (PMMA) is used as the mechanical material instead of silicon. Conventional silicon micromachining techniques are used to produce the silicon molds. Hot embossing technique is used to transfer the patterns from silicon mold to PMMA. By using PMMA and hot embossing, low cost devices with massive and rapid replication can be conveniently realized.

1.1 Introduction

The electron tunneling effect has been widely studied and used in many applications since Binning and Rohrer were awarded the Nobel Prize for their original design of the Scanning Tunneling Microscope (STM) in 1986. By utilizing the tunneling current between the tunneling tip and its counter electrode, various kinds of microsensors and microtransducers can be fabricated. They can be used in many applications such as accelerometer, gyroscope, and uncooled infrared sensor.

Uncooled infrared sensors are widely used in low cost applications such as remote temperature sensing, intrusion detection, and night operations. Generally, uncooled infrared sensors are based on the thermal detection principles. Thermal detectors are used in infrared sensing systems. At room temperature, Golay Cell-based infrared detector offers the highest sensitivity compared with other infrared detectors, such as bolometer-based and thermopile-based infrared detectors.

As originally designed, the Golay Cell had a fragile membrane and a gas cell. The absorption of infrared radiation will heat the gas in the Golay Cell. The gas will expand thermally and force the membrane to deflect outwardly. Optical beam or capacitive displacement transducer has been used to detect the deflection of the membrane. Tunneling based transducer has also been used in infrared detectors to detect the deflection of the membrane. Due to the exponential relationship between the tunneling current and the tunneling distance, tunneling infrared detectors may easily achieve higher sensitivity, higher resolution with smaller size. Almost all the tunneling infrared detectors are based on silicon and silicon micromachining techniques.

Recently, polymer-based MEMS have gained a broad theoretical interest and practical applications. Compared with the traditional silicon-based or glass-based techniques, polymers offer a number of advantages for sensor technology, including low cost, chemical and biological compatibility, easy of fabrication, and material flexibility. Polymer microsensors are becoming more and more important and can be low-cost alternative to the silicon-based and glass-based microsensors. The low cost fabrication methods of polymers include injection molding and hot embossing. These techniques are suitable for mass production, and no need for special clean room and high temperature processes.

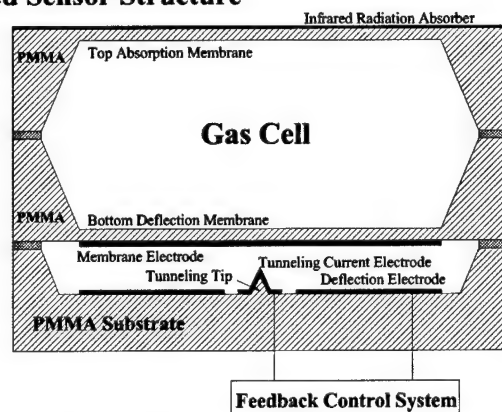## 1.2 Tunneling Infrared Sensor Structure

Fig. 1. Schematic diagram of a polymer-based tunneling infrared sensor.

Fig. 1 shows the cross-section schematic of a polymer-based tunneling infrared sensor. It consists of three mechanical components, a layers of infrared radiation absorber, feedback control system, and several electrodes. A high deflection voltage is applied on the bottom deflection electrode. Electrostatic force is established to attract the bottom deflection membrane bend downward. The distance of the tunneling gap can be controlled by varying the value of the high voltage. Tunneling current is generated when the gap between the tunneling tip and its counter electrode is within the range of 10 Å. The current will remain constant if the gap remains unchanged. In the low bias region, the tunneling current I_t is linearly proportional to the applied junction bias V_B, and exponentially proportional to the distance of the tunneling gap x. It can be expressed as:

$$I \propto V_J \bullet \exp(-\alpha\sqrt{\Phi}x)$$

Where α is approximately 1.025 $\text{Å}^{-1}\text{eV}^{-0.5}$, Φ is the effective local potential barrier height or the work function of the electrode material.

Instead of silicon, an amorphous polymer material Polymethylmethacrylate (PMMA) is chosen as the mechanical material. PMMA offers a number of advantages: it is inexpensove, flexible, and optically transparent. PMMA is much softer than silicon. The Young's Modulus of PMMA and silicon are about 2 Gpa and 165 Gpa, respectively. For some structures like the deflection membranes, PMMA-based structures can achieve higher sensitivity more easily than silicon-based structures. Also, PMMA is a type of thermoplastic polymer, and is suitable for some mass production techniques, such as injection molding and hot embossing lithography (HEL). Hot embossing lithography, also referred to as nanoimprint lithography, is used to fabricate the polymer structures.

Two PMMA structures are bonded together to form the gas cell. The thickness of the gas cell is about 0.2 mm. A thin layer of platinum is deposited on the surface of top absorption membrane, as the infrared radiation absorption material. Gold is used as the electrode material. A thin layer of titanium is used as adhesion layer between PMMA and gold. Sensors with different sizes have been fabricated. The sizes are 1 mm × 1 mm, 2 mm × 2 mm, and 4 mm × 4 mm.

Once the infrared radiation is absorbed by the thin layer of platinum, it is converted to heat. The trapped gas is heated by contact with the top absorption membrane. It expands thermally and forces the bottom deflection membrane to bend downward. The membrane electrode changes its original position and moves relatively to the tunneling tip. The tunneling current is changed due to the variation of the tunneling gap. According to the change of the tunneling current, the feedback control system adjusts the voltage applied to the deflection electrode, thus, the electrostatic force moves the deflection membrane back to its original position. The power of the infrared radiation can be measured by reading out the feedback deflection voltage.
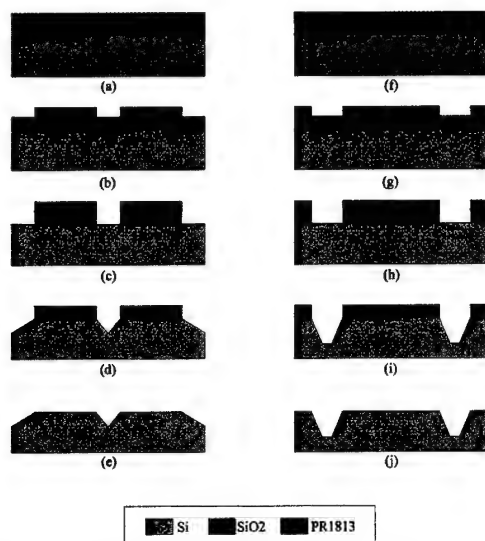
Fabrication of Silicon Mold:

Figure 2. Fabrication process for the silicon molds.

Silicon molds are fabricated using conventional bulk-silicon micromachining techniques. Fig. 2 shows the fabrication processes for the silicon molds. Only two silicon molds are needed. One is for the tunneling tip part (Fig. 2a-2e); the other is for both the top absorption membrane part and the bottom deflection membrane part (Fig. 2f-2j).

The fabrication of the silicon molds for tunneling tip begins with p-type <100> silicon wafers. Both sides of the silicon wafers are coated with 1 μm SiO_2. A thin layer of photoresist (PR1813) is spin coated on the surface of the silicon wafer (Fig. 2a). Conventional lithography is used to pattern the PR1813 (Fig. 2b). Exposed SiO_2 is removed by buffered hydrofluoric acid (BHF) (Fig. 2c). Then the wafer is submerged in a 45% KOH solution which is heated to 85°C. The etch rate is about 0.8 μm/minute. When the silicon pit is formed (Fig. 2d), the KOH etch can be stopped. The final step for making silicon mold is to remove all the SiO_2 with BHF solution. Figure 3 shows the small pit on the silicon mold with the size of 40 μm × 40 μm.

As for the silicon molds for the membranes, it has similar fabrication steps as for the tunneling tip silicon mold.
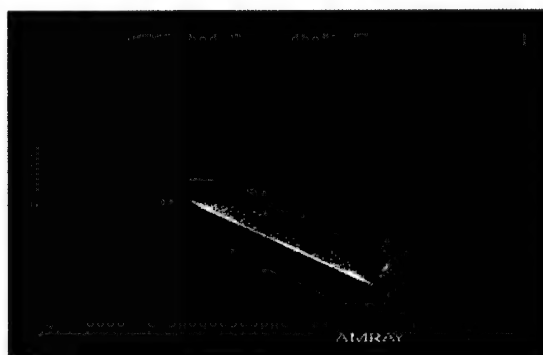
Figure 3. SEM image of silicon pit (with the size of 40 μm × 40 μm).

1.3 Hot Embossing on PMMA
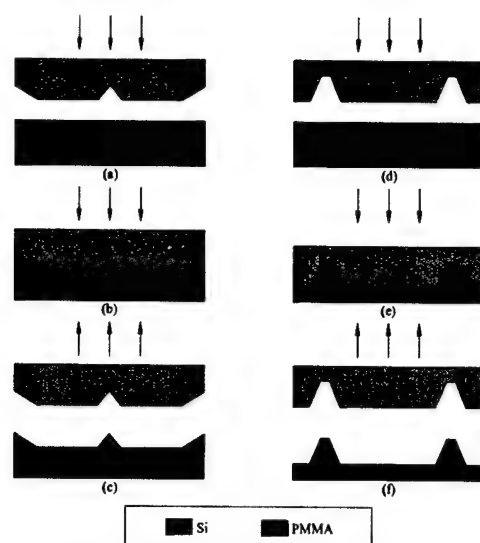
Figure 4. Hot embossing on PMMA.

The patterns on the silicon molds are transferred to the PMMA by hot embossing lithography. The PMMA we are using is Cyro Industries ROHAGLAS Film 99530. It has unique thermal and mechanical properties which make it behave ideally in hot embossing process. The glass transition temperature T_g and the melting temperature T_m of the PMMA are 98°C and 170°C, respectively. The fabrication processes for both the tunneling tip (Fig. 4a-4c) and the membranes (Fig. 4d-4f) are shown in Fig. 4. The fabricated PMMA structures are affected by several parameters. The touch force is set as 500 N, and the maximum contact force is set from 18 kN to 25 kN. The wait time is set from 300 to 450 seconds; making sure that the PMMA has enough time to flow into the silicon structures. PMMA structures with different sizes have been fabricated. The sizes of the polymer tunneling tips range from 40 μm × 40 μm to 90 μm × 90 μm. The sizes of the polymer membranes range from 1 mm × 1 mm to 4 mm × 4 mm. For structures with different sizes, different parameters need to be chosen and optimized. Figure 5 shows a PMMA tip with the size of 40 μm × 40 μm. The fabrication parameters are set as follows: the relative position is -16 mm; the maximum contact force is 25 kN, and the wait time is 300 seconds.

Figure 5. SEM image of PMMA tip pit (with the size of 40 μm × 40 μm).

1.4 Assembly of Polymer Actuator
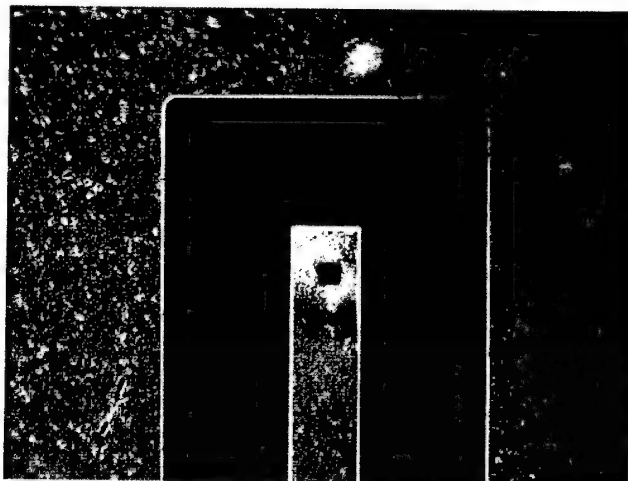
Figure 6. Optical image of the PMMA tunneling tip with electrodes.

The thickness of the PMMA membranes is reduced by Reactive Ion Etching (RIE). The maximum etching rate achieved is 0.5 µm/min, when the plasma consists of 2.5% SF_6 and 97.5% O_2. Then Ti/Au (200 Å/1000 Å) layers are sputtered on the PMMA structures as the electrodes. Ti/Au can be patterned by KI/I_2 solution and BHF. Figure 6 shows the optical image of the PMMA tunneling tip with the electrodes.

The tunneling tip part and the bottom deflection membrane part are bonded with conductive glue. The conductive glue also used for bonding the aluminum wire with the Au electrodes. The top absorption membrane part and the bottom deflection membrane part are bonded with MMA solution to make the gas cell. As shown in Fig. 7, the two parts and the aluminum wires are bonded together with conductive glue. The device is mounted on a standard IC socket. After the measurement of the deflection membrane's properties, the top absorption membrane can be bonded with MMA solution.
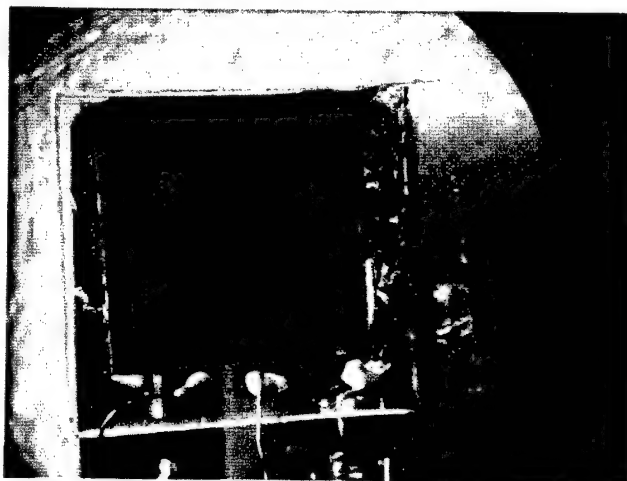
Figure 7. Optical image of the assembled sensor.

1.5 Measurement Results and Discussion:

Fig. 8 shows the measurement result of the bandwidth of the actuator. For this measurement, the membrane electrode is set as GND and a high AC voltage is applied on the deflection electrode. The bottom deflection membrane will vibrate due to the electrostatic force between two electrodes. A laser interferometer is used to detect the small displacement of the deflection membrane. As shown in Fig. 8, the natural frequency of this polymer actuator is about 4500 Hz; and the bandwidth of the actuator reaches about 5500 Hz. The responses are higher than 2.7 nm/V at all frequencies over 5500 Hz.
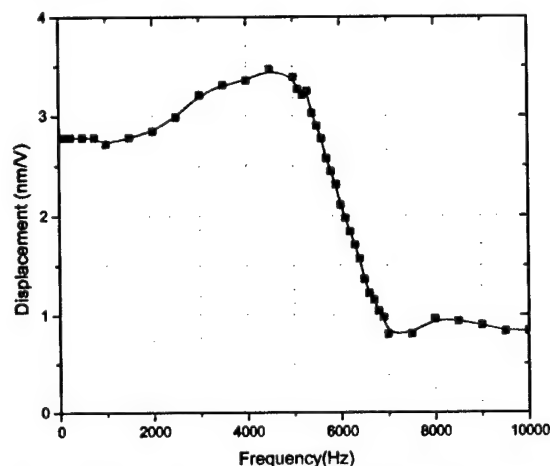
Figure 8. Frequency response of the polymer actuator.

Figure 9 shows the time records of the output of the laser interferometer under different frequencies. The input high AC voltage is a sinusoidal wave. Only when the frequency is 4500 Hz, the actuator is able to reproduce the input signals accurately and the displacement of the membrane reaches the highest value.

(a) f = 2 kHz   (b) f = 4.5 kHz

(c) f = 5.5 kHz   (d) f = 10 kHz
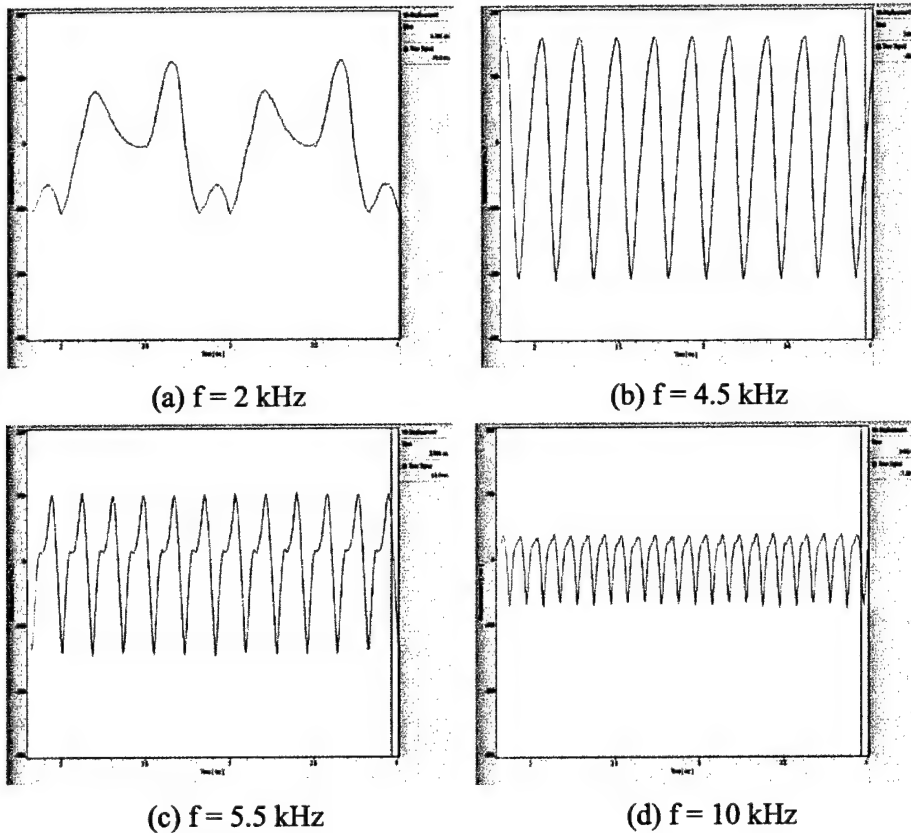
Figure 9. Time records of the output of the laser interferometer under different frequencies.

The actuator is a parallel capacitor and the electrostatic force between two electrodes is proportional to the square of the applied voltage:

$$F \propto V_a^2$$

Fig. 10 shows the measured result of the electrostatic force of the actuator, which fits the quadratic polynomial relation well. The deflection of the membrane is detected by the laser interferometer. The input deflection voltage is a 1000 Hz sinusoidal wave.
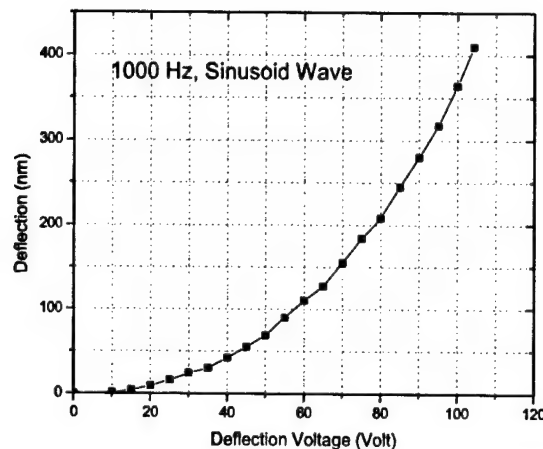
Figure 10. Measurement of electrostatic force between two electrodes.

During the operation of the tunneling infrared sensor, a high DC voltage is applied to the deflection electrode, which is to set the operation point. A small AC output voltage, which is caused by the infrared radiation, will be added to this high voltage. For the dynamic control, since $V_{DC} \gg V_{AC}$, the responsivity is linearly proportional to the V_{DC}. This means the detectable vibration of the deflection membrane is linearly dependent on V_{DC}. During the measurement, the AC component of deflection voltage is fixed at a certain value and the DC component is changed gradually. Fig. 11 shows the responsivity of the electrostatic actuator as a function of V_{DC}. The linear relationship can be proven.
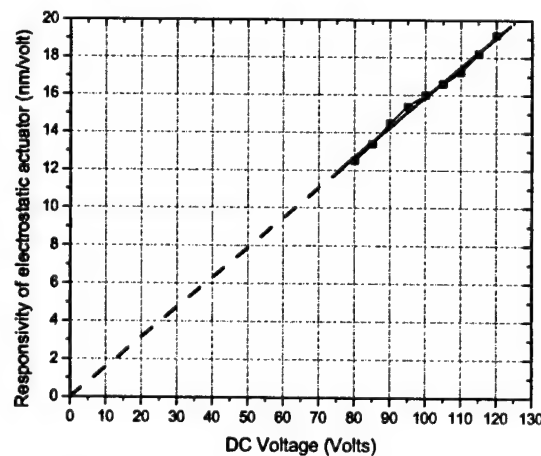
Figure 11. Dynamic responsivity of the electrostatic actuator.

1.6 Conclusions

A low-cost polymer based electrostatic actuator has been fabricated and measured. The design of polymer tunneling infrared sensor has been provided in this report. All the silicon molds were fabricated by conventional lithography and wet etching techniques. Hot embossing lithography was used to make all the PMMA structures. The optimal conditions for the pattern replication have been developed and reported. For the PMMA tip with size of 40 μm × 40 μm, the relative position is -16 mm; the maximum contact force is 25 kN, and the wait time is 300 seconds.

Sensors with different feature sizes have been fabricated, and assembled by conductive glue. The natural frequency of the actuator is about 4500 Hz and the bandwidth reaches 5500 Hz. The electrostatic force between two parallel electrodes has been measured and plotted. The dynamic responsivity of the actuator has been proven to be linearly dependent on the DC component of the deflection voltage.

2. Modeling and Design of Polymer-based Tunneling Accelerometers

This part of the report describes the mechanical-level and system-level modeling and design of a polymer (PMMA) based tunneling accelerometer by integrating ANSYS and MATLAB. The simulation proves that, for the same microstructure, the PMMA-based accelerometer can achieve higher sensitivity than the silicon-based. Several structural factors are obtained by mechanical-level simulation using ANSYS, thus avoiding the need for complicated calculations. These factors are adopted in higher system-level simulation, resulting in the improved development of a high-performance accelerometer. A simple, effective, and linearized mathematical model of accelerometer with feedback controller is established. A transfer function of the system is derived using Laplace transformation. Root locus, step response, bandwidth, and the damping effects of the system are plotted and discussed. The performance of the device can be evaluated by the system-level model using MATLAB. Based on mechanical-level and system-level simulation, the design of the tunneling sensor can be simplified, and stable tunneling accelerometer systems with high sensitivity, high performance, and wide bandwidth can be conveniently developed.

2.1 Introduction

The electron tunneling effect has been extensively investigated, developed, and used in many applications, since Binning and Rohrer were awarded the Nobel Prize for their original design of the scanning tunneling microscope (STM) in 1986. By utilizing the tunneling current between the tunneling tip and its counter electrode, many types of microsensors and microtransducers can be designed and fabricated. They have many applications such as accelerometers, infrared sensors, and gyroscopes. High-performance accelerometers are in great demand in many applications such as acoustic measurement, seismology, and navigation. Considerable research work on accelerometers has been reported by several groups. Compared with some other common and well developed accelerometers, such as capacitive, piezoresistive, piezoelectric accelerometers, tunneling accelerometers may easily achieve higher sensitivity and higher resolution with a smaller size, due to the exponential relationship between the tunneling current and the distance between two tunneling electrodes. However, the tunneling sensors are usually more difficult to be fabricated than others. Since the tunneling current can only be observed when the gap between the tunneling tip electrode and its counter electrode is in the range of 10 Å, a close-loop system is needed to maintain the constant gap at 10 Å in scanning tunneling microscope. Kenny's group developed a μ-synthesis-based controller for a micromachined tunneling accelerometer. Chingwen Yeh and Khali Najafi built a close-loop sensor-circuit system based on their design of CMOS interface circuitry by employing MAPLE V. Aaron Partridge presented an integrated and complete tunneling sensor controller using traditional CMOS techniques.

Recently, polymer-based MEMS have gained a broad theoretical interest and practical applications. Compared with the traditional silicon-based or glass-based techniques, polymers offer a number of advantages for sensor technology, including low cost, chemical and biological compatibility, easy of fabrication, and material flexibility. Polymer microsensors are becoming more and more important and can be low-cost alternative to the silicon-based and glass-based microsensors.

Our objective has been to design and fabricate a polymer-based tunneling accelerometer. Since new polymer material is used and it is complicated to fabricate the tunneling sensor, simulation work can be helpful to estimate the static and dynamic properties of the device. ANSYS and MATLAB are utilized and integrated as the computer-aided tools to make structural and system-level analysis. The integration of these two software benefits the design and development of the tunneling accelerometer. Compared with the research work of other groups and our previous work, more detailed information on the accelerometer can be obtained from our current analysis results. Varieties of accelerometer structures are simulated by ANSYS. With a simple structure, a high sensitivity of 47 nm/g and a high resolution of 1.17 mg/√Hz can be achieved. The advantages of PMMA are proved from the simulated results. A simple but effective system-level functional model of the tunneling accelerometer is established, and the sensitivity, stability, and dynamic range can be evaluated through inputting parameters obtained from mechanical-level ANSYS simulations. By integrating ANSYS and MATLAB, complicated analytical calculation can be avoided, much time for development and experiments can be saved, and the performance of the sensor can be predicted.
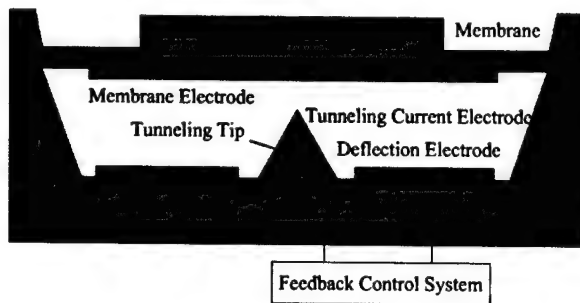
Fig. 12. Schematic diagram of a polymer-based tunneling accelerometer.

2.2 Mechanical-Level Analysis and Discussions

As shown in Fig. 12, the typical tunneling accelerometer includes mechanical components, feedback circuitry, and several electrodes. By applying a high deflection voltage on the bottom deflection electrode, the electrostatic force attracting the top membrane to bend downward can be established, thus the distance of the tunneling gap can be controlled. The tunneling current can be generated when the gap between the tunneling tip and its counter electrode is small enough (within about 10 Å), and the current value will remain constant if the gap is kept unchanged. In the low bias region, the tunneling current I_t is linearly proportional to the applied junction bias V_B, and exponentially proportional to the distance of the tunneling gap. More detailed information about the tunneling principle and other designs of tunneling sensor can be found elsewhere.

Polymethylmethacrylate (PMMA) is used as the main structural material instead of silicon. PMMA offers many advantages, such as low cost, flexibility, optical transparency, and its properties can meet some specific applications. Hot embossing is used to fabricate the microstructures of a PMMA accelerometer. Gold is used as the electrode material. The detailed information on fabricating a PMMA-based tunneling accelerometer can be found in reference section.

ANSYS, an simulation package for general purpose finite element analysis, is used to simulate the structure properties of the device. Static analysis, modal analysis, and harmonic analysis are performed to obtain better understanding of the response of the tunneling accelerometer structure. Many structures have been simulated by ANSYS. A structure of membrane without proof mass is described here for its simplicity. More complex structures can also be simulated based on the same principle.

Fig. 13. Displacement of the membrane based on Static analysis.

By static analysis, the displacement of the membrane can be calculated by ANSYS. For a simple square PMMA membrane with all four sides fixed, a 1 N/m^2 pressure can cause a displacement less than 1 μm in the center of the membrane. Since only the small area opposite to the tunneling tip is important, the whole structure can be simplified, its spring constant is given by $k=F/\Delta z=P \cdot S/\Delta z$, where P is the pressure, S is the surface area of the structure, Δz is the displacement in the center. As shown in Fig. 13, the maximum displacement of the structure is about 0.2 μm, and the corresponding spring constant k is approximately equal to 80 N/m. From W. C. Young's book, the spring constant of this structure is given by

$$k = \frac{E \cdot t^3}{\alpha \cdot l^2}$$

where E is the Young's Modulus of PMMA, α=0.0135 is a constant related to the structure dimension, t and l refer to the thickness and length of the membrane, respectively. From this equation, the spring constant k is about 74 N/m. The small difference between the simulated result and the calculated result may be because the high-aspect-ratio membrane cannot be meshed well. For more complex structures difficult to be calculated analytically, ANSYS can be helpful.

The spring constant of membrane is proportional to the Young's Modulus E and the cubic power of the thickness t^3. PMMA is much softer than silicon. The Young's moduli of PMMA and silicon are around 2-3 Gpa and 165 Gpa, respectively. For the same structure, the spring constant of PMMA is much smaller than silicon. In other words, to obtain the same spring constant, a PMMA-based structure can be much thicker than a silicon-based structure. The requirements for the PMMA structure dimension are not as strict as silicon structures. This will benefit the design and the fabrication processes.

Modal analysis is used to calculate the natural frequency and mode shapes of the membrane structure. For a 4-side fixed square membrane, several vibration modes can be obtained by ANSYS. As shown in Fig. 14, (a) is the simple bending mode at 3049 Hz, (b) is another twisted vibration mode at 6217 Hz. For the accelerometer, the simple bending mode is the right choice for the membrane structure. The natural frequency of this structure is given by

$$ f = \frac{K_1 \cdot t}{2\pi d^2} \sqrt{\frac{E}{12(1-v^2)\rho}} $$

where K_1=36 is a constant related to the 1st mode of vibration, v is the Poisson's ratio of PMMA, and ρ is the density of PMMA. Natural frequency f=3020 Hz can be derived from this equation, almost the same as the simulated result.
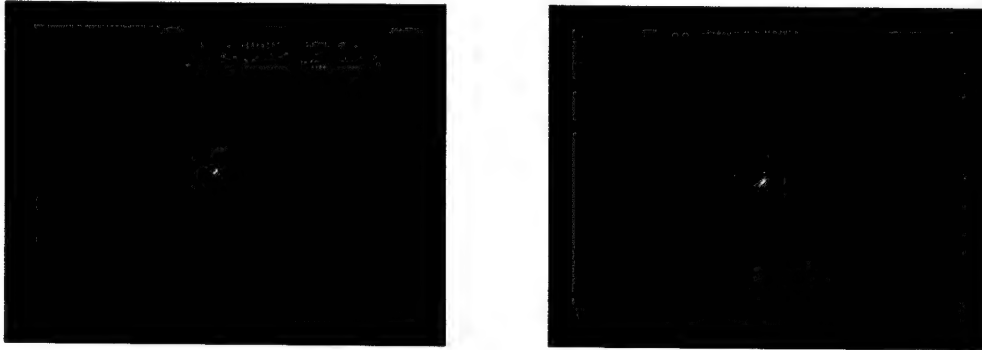
Fig. 14. Two vibration modes of the membrane.
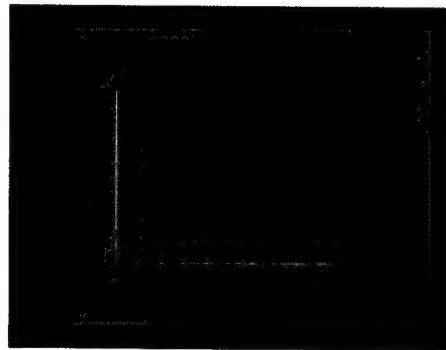
Fig. 15. Membrane response for external acceleration at different frequencies.

Harmonic analysis is used to determine the response of the membrane structure in different frequencies. Fig. 15 shows the frequency-amplitude response of the membrane. When the frequency is about 3050 Hz, the membrane has the largest displacement. This value is consistent with the result obtained from modal analysis. Mostly, the tunneling accelerometers operate under a vacuum environment, thus mechanical quality factor Q usually has a high value of 100 or more. Since the relation between the quality factor Q and the damping ratio ξ is $Q \cdot \xi = 1/2$, low $\xi = 0.01$ is used here.

The mass of the PMMA membrane is $m = \rho \cdot V$, where ρ is the density of PMMA, V is the volume of the structure. The spring constant of the structure can be calculated from the results of the ANSYS static analysis. The damping coefficient needs to be calculated by some other methods such as specific formulas for different structures. All these values can be used in MATLAB. For simple structures such as rectangular and circular membranes, it is easy to get the spring constant, natural frequency, and some other values related to the structure through analytical methods. However, for more complex structures, which cannot be solved by simple formulas, ANSYS will be the numerical tool to solve the problem.

From the equation $S = \Delta z / a = m / k$, where S is the sensitivity of the structure, a is the external acceleration applied on the structure surface, the sensitivity is inversely proportional to the spring constant k. Compared with the silicon-based structure, it is easier for the PMMA-based structure to get a higher sensitivity due to its smaller Young's modulus and spring constant.

To estimate the right thickness of PMMA, Sequential Coupled-Field Analysis is used. Since the actuator is a parallel capacitor with the electrostatic force described as

$$F_{es} = \frac{\varepsilon S_o V_a^2}{2(g + \Delta x)^2}$$

where ε is the permittivity, S_o is the overlap area of actuator electrodes, V_a is the applied voltage on the actuator to set the operation point, g is the nominal gap between the electrodes, and Δx is the displacement caused by the external acceleration. Since tunneling current can only be established when the tunneling gap is about 10 Å, an electrostatic force is used to set this gap. For the 4 mm x 4 mm structure, a high voltage about 100 V is needed to attract the center of the membrane bending downward by 2 μm, thus setting the operation point. The results from Sequential Coupled-Field Analysis can also be used in the system-level simulation by MATLAB.

For this 4 mm × 4 mm × 20 μm structure, the sensitivity is about 47 nm/g, and the total noise equivalent acceleration (TNEA) of thermalmechanical noise is given by

$$TNEA = \sqrt{\frac{4 k_B T \omega}{mQ}}$$

where k_B is the Boltzmann constant, T is the temperature, ω is the resonant frequency of the membrane, m is the proof mass, and Q is the mechanical quality factor. If Qi is set as 100, the calculated value of the noise is about 1.17 mg/ $\sqrt{}$ Hz.

From the simulation results of mechanical-level simulation, many factors of the structure can be obtained. Consequently much calculations and time can be saved, especially for the complicated structures.

2.3 Mathematical Model of a Tunneling Accelerometer

MATLAB Simulink is used to establish the mathematical model according to the structures and transfer functions of the tunneling accelerometer. The model is composed of different function blocks based on Laplace transformation. However, the whole system is a nonlinear system, and several function blocks are difficult to be modeled. Assumptions and approximations are necessary to linearize the whole system.

The membrane as well as the proof mass is the sensing part of the accelerometer. It can be considered as a suspended mass-spring-damping system, thus it can be expressed as

$$m \cdot a_{ext} = m \cdot \frac{d^2 \Delta x}{dt^2} + b \cdot \frac{d \Delta x}{dt} + k \cdot \Delta x$$

where m, b, k represent the mass, damping coefficient, and spring constant of the membrane/proof mass, respectively, a_{ext} is external acceleration, Δx is the center point displacement of the membrane/proof mass. Through Laplace transformation, the dynamic performance of the suspended structure can be expressed as

$$\frac{\Delta x}{a_{ext}} = \frac{1}{S^2 + \frac{b}{m}S + \frac{k}{m}}$$

The mathematical model of this formula is shown in Fig. 16. Through this model, the external acceleration is transferred to the displacement at the center of the membrane/proof mass.
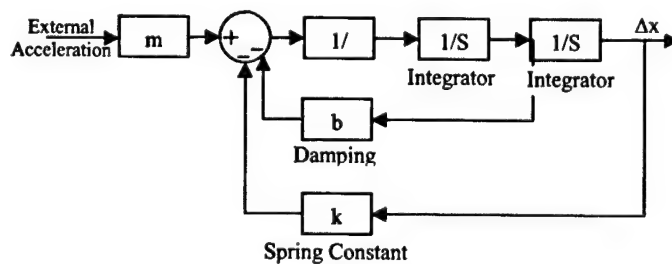
Fig. 16. Mathematical model for suspended membrane/proof mass.

In the tunneling accelerometer, the tunneling current is exponentially proportional to the change of the tunneling gap, which is given by

$$I = I_0 \bullet \exp(-\alpha\sqrt{\Phi}\Delta x)$$

The whole device works as a close-loop system, and the feedback control circuit adjusts the electrostatic force to balance the external force caused by acceleration, thus the operation tunneling gap 10 Å can be maintained. Compared with the tunneling gap, Δx is very small. Therefore the current can be developed by Taylor series as

$$I = I_0(1 - \alpha\sqrt{\Phi}\Delta x)$$

The change of the output voltage ΔV can be presented by

$$\Delta V = (I - I_0) \cdot R \cdot A = \Delta I \cdot R \cdot A = I_0 \cdot \alpha\sqrt{\Phi}\Delta x \cdot R \cdot A = C \cdot \Delta x$$

where R is the resistance of a high value resistor, A is the amplitude of the amplifier, and C is a constant. The tunneling mechanism is linearized due to the small displacement of the membrane/proof mass.

For the actuator, the electrostatic force is proportional to the square of the applied voltage, which is composed of DC constant voltage V_{dc} and the feedback voltage V_{fb}. Since V_{dc} (about 100 V) is much higher than V_{fb} (several millivolts), the electrostatic force can be given by

$$F_{es} \propto V_a^2 = (V_{dc} + V_{fb})^2 = V_{dc}^2 + 2V_{dc}V_{fb} + V_{fb}^2 \approx V_{dc}^2 + 2V_{dc}V_{fb}$$

The first item is used to set the operation point, and the second item is related to the feedback force applied to the membrane. The feedback force can be simplified as

$$F_{fb} = \frac{\varepsilon S}{g^2}V_{dc}V_{fb} = K \cdot V_{fb}$$

where K is the feedback constant. A possible value is 3.54×10^{-3} N/V with an overlapped area of 4 mm × 4 mm, a nominal gap of 2 μm, and a high DC voltage of 100 V. This value is estimated by Sequential Coupled-Field Analysis of ANSYS.

Based on the above approximations, the entire system can be linearized and modeled. The detailed function block diagram is shown in Fig. 17 (a). By the combination of several components, it can be simplified as shown in Fig. 17 (b).

Through the function block diagrams, the transfer function of the whole system can be expressed as

$$\frac{\Delta V}{a} = \frac{m \cdot H_1(S)}{1 + K \cdot H_1(S)H_2(S)} = \frac{m \cdot g^2 \cdot I_0 \cdot \alpha\sqrt{\Phi} \cdot RA}{(mS^2 + bS + k) \cdot g^2 + \cdot \varepsilon S_0 \cdot V_{dc} \cdot I_0 \cdot \alpha\sqrt{\Phi} \cdot RA \cdot H_2(S)}$$

$H_1(S)$ represents the mechanism of the suspended membrane/proof mass and the electron tunneling, which is

$$H_1(S) = \frac{I_0 \cdot \alpha \sqrt{\Phi} \cdot RA}{mS^2 + bS + k}$$

Both of the items in $H_1(S)$ are related with the structure of the accelerometer. Most of the parameters can be extracted from ANSYS simulation. Feedback constant K can also be estimated from ANSYS simulation.

$H_2(S)$ is the feedback control system to transfer the output voltage ΔV to the feedback voltage V_{fb}, which can be optimized by MATLAB simulation. The objective of this feedback control system is to enhance the system stability and responsibility while broadening the bandwidth.
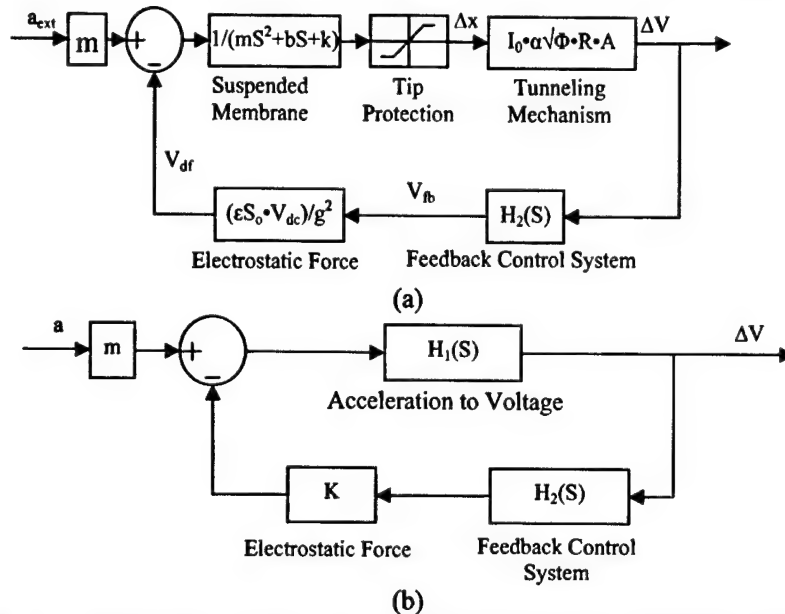
Fig. 17. Mathematical model of the tunneling accelerometer: (a) Block diagram of the close-loop system. (b) Simplified block diagram of the close-loop system.

Compared with several other models of the tunneling sensor developed by other groups, our model is not only simple but also effective, since many factors of this model can be obtained from the ANSYS simulation. For example, compared with the robust μ-synthesis based controller designed by C.H. Liu, our model is simpler, and almost all the dynamic properties of the accelerometer can be evaluated. Compared with our previous model designed by J. Wang, dynamic function blocks of membrane is adopted instead of static function blocks, which will generate more accurate results.

2.4 System-level Simulation Results and Discussions

After modeling, the system can be simulated and the characteristics of a tunneling accelerometer can be evaluated. Many structures were simulated from this mathematical model. Here the simple structure with dimension of 4 mm × 4 mm × 20 μm is used.

Based on the ANSYS simulation, the spring constant k can be approximately equal to 80 N/m, its mass is about 368 μg, and high DC voltage is 100 V to set the operation point. A damping coefficient b=0.3×10^{-2} N•s/m is used for the simulation.
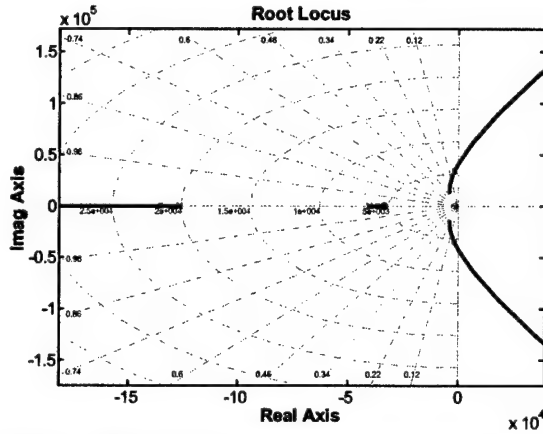
Fig. 18. Root locus of the accelerometer system.

Root locus is a powerful graphical method to determine the poles of a close-loop system. For a stable system, all the poles are required to stay in the left side of the s-plane. Fig. 18 shows the root locus and all the poles of the accelerometer. The poles may have some possibilities to lie in the right side of the s-plane. By adjusting the feedback control system $H_2(S)$, all the poles are moved to the left side, thus the system is stable. The system stability can also be seen from the close-loop step response, as shown in Fig. 19. The close-loop system will become stable in less than 4 ms. The response time will be determined by the feedback control $H_2(S)$ and damping ratio.
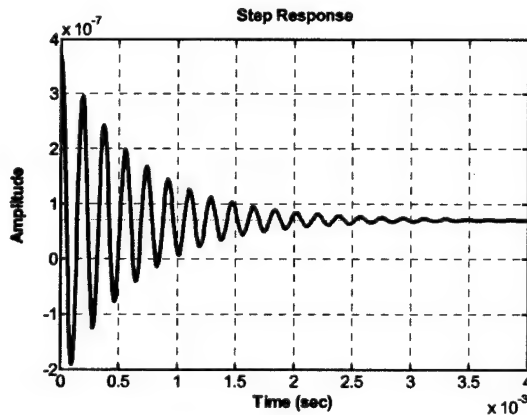
Fig. 19. Step response of the close -loop system.

For the system stability and responsibility, there are many expressions of transfer function $H_2(S)$. A well designed transfer function with one zeros and two poles is enough to satisfy the requirements. It can be easily realized by several electronic components such as resistors, capacitors, and amplifiers. The circuit itself is quiet simple.

The tunneling accelerometer is operated in a close-loop mode. The bandwidth of the system can be extended due to the feedback control system. As shown in Fig. 20, (a) is the bode diagram of a open-loop system, the bandwidth is about 3 kHz, and for the close-loop system (b), the bandwidth is broadened to about 8 kHz. It means that the tunneling accelerometer can operate in a wider range.
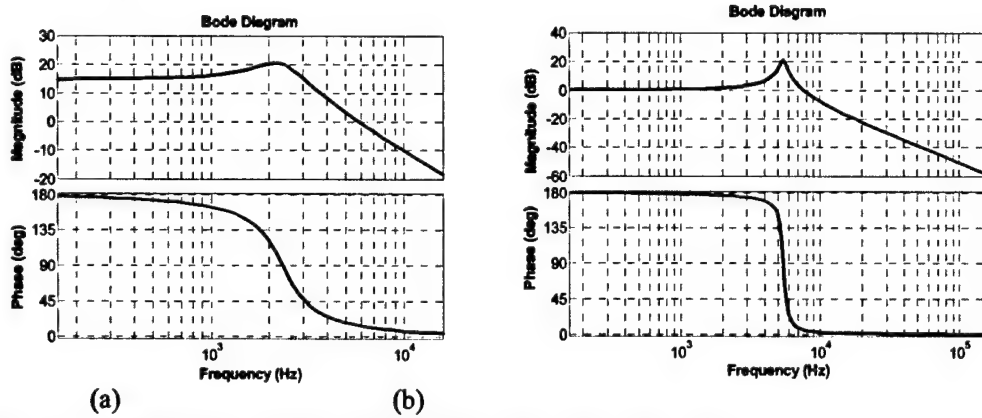
Fig. 20. Bode diagram. (a) Open-loop system. (b) Close-loop system.
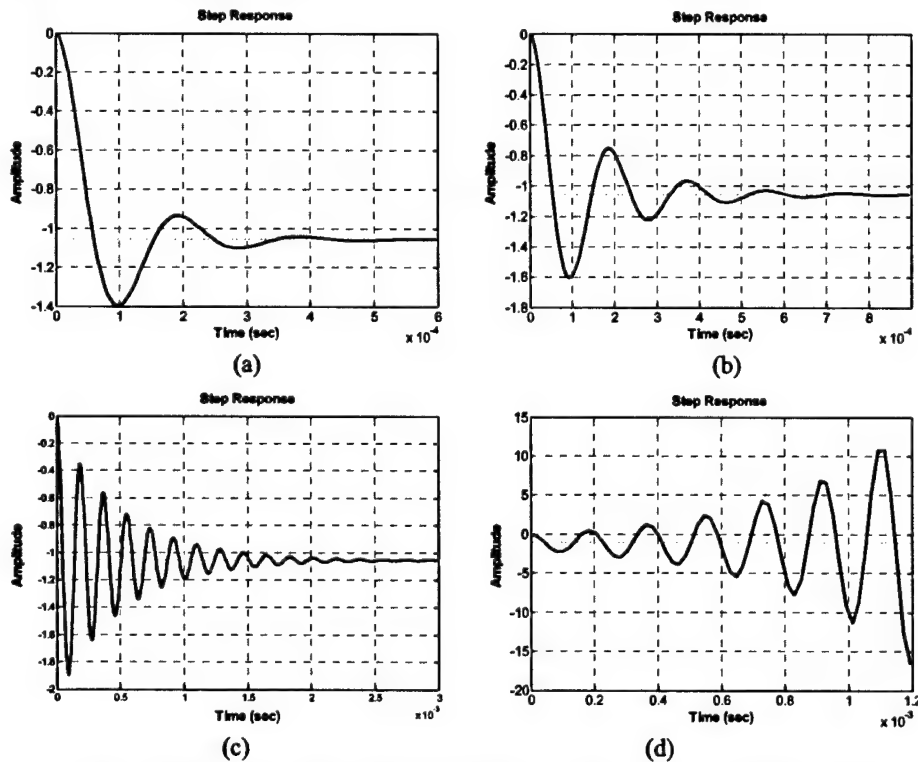
Fig. 21. Step response under different damping ratios. Their effective damping ratio and settling time are: (a) ξ_{eff} =0.9, t_s=0.5ms. (b) ξ_{eff}=0.6, t_s=0.8ms. (c) ξ_{eff}=0.3, t_s=3ms. (d) ξ_{eff}=0.01, system unstable.

Because the tunneling accelerometer often works under a vacuum environment, the device has a high Q and a small damping coefficient. It may cause a longer settling time of step response or even instability of the system. Fortunately, the effective value of Q_{eff} can be reduced in a close-loop system. Consequently, both of the effective damping coefficient b_{eff} and damping ratio ξ_{eff}

can be increased. Several results of step response with different damping ratios are shown in Fig. 21. A smaller damping ratio causes longer settling time.

To understand the damping effect on the system, all other transfer functions except the suspended membrane/proof mass are defined in the mathematical model. By modifying the value of damping coefficient, the influence of damping on the final performance of the system can be learned. Based on the simulation results, a number of conclusions can be reached:

♦ The damping coefficient has no effect on the loop gain of the system, thus, the damping has no relationship with the sensitivity of the device.
♦ The damping can affect the stability of the system. The root locus of this model has some part in the right hand of the s-plane, a very small damping coefficient may cause the roots move to the right side, thus, the system becomes unstable.
♦ The damping almost has no effect on the bandwidth of the close loop system. Compared with the wide bandwidth of the system, the small change can be ignored.

2.5 Conclusions

A simple method by simulation for designing polymer-based tunneling accelerometer is described in this report. ANSYS is used for mechanical-level analysis. PMMA is used as the mechanical material instead of silicon. Based on ANSYS simulation, it is proved that PMMA has several advantages over silicon: high sensitivity, simple fabrication process, and the requirements for dimension are not so strict. For a simple membrane structure with dimension of 4 mm × 4 mm × 20 μm, a high sensitivity of 47 nm/g and a high resolution of 1.17 mg/√Hz can be achieved. Several factors such as spring constant, natural frequency, and electrostatic force of the structure can be obtained from the simulation results, which can be used in higher level simulation. MATLAB is used for the system-level analysis. A simple but effective mathematical model is described. Each function blocks of the model are discussed and analyzed. Based on small signal variation of the sensor, the model is linearized. Transfer function of the system is derived by Laplace transformation. Simulation results about root locus, step response, bandwidth, and damping effect have been described and discussed. By integrating ANSYS and MATLAB, complicated calculations can be avoided, time for development and experiments can be saved, and the performance of the sensor can be predicted.

3. Polymeric Magnetic Field Sensor Based on Nanocomposite Magnetic Thin Films

This section reports on a magnetic field sensor that is based on the polymer tunneling sensor platform developed. The sensor structure includes nanocomposite magnetic thin films obtained from Drs. E. I. Meletis and X. Nie at Louisiana State University. The all-PMMA-based magnetometer has been designed, and the relations between magnetic field, magnetic force, and displacement changes have been calculated and derived.

Based on the theoretical work conducted, the best displacement resolution of tunneling sensor is about 1×10^{-4} Å$/\sqrt{Hz}$, which can produce a magnetic noise level of 0.3 nT/√Hz. The all-PPMA tunneling sensor magnetometer is designed due to its simple processing and low cost. The

magnetometer included a 250 nm to 300 nm membrane structured magnetic film, tunneling tip, counter electrode, deflection electrode, and measurement circuit. The calculated value of DC magnetic field matched the measurement result very well and the AC magnetic field was up to ± 20 G ($2 \times 10^{-3} T$). The relationship between the magnetic field and the force was also derived. The force is propotional to the overlap area and the square of the field.

The remarkable displacement sensitivity of the scanning tunneling microscope has inspired the development of a new class of sensors: tunneling sensor. For these transducers, displacement is measured by the small changes in tunneling current between two electrodes. Typically, the original displacement is biased at 1.5 nA, and the tip-to-electrode gap is set to be about 1 nm. For the gold electrodes at room temperature and atmosphere, the 1% change in tunneling current corresponds to a separation change of 0.003 nm. From calculation, the best resolution of displacement is 1×10^{-4} $\text{Å}/\sqrt{Hz}$. With the modern silicon micromachining techniques, mechanical structures with micron dimensions are easily achieved. The high sensitivity of the tunneling transducer allows a micro mechanical structure to offer sensor performance normally obtained only from much larger devices. Thus, the tunneling sensor platform offers a new opportunity for the miniaturization of a class of physical sensors.

The tunneling sensor platform has been used as accelerometers, displacement meters, and seismometers. Tunneling magnetometers based on silicon have been reported with a resolution of 0.3 nT/√Hz at 1 Hz, which offered a unique combination of high resolution and small size. The goal of this work is to develop a magnetometer, which can perform a high resolution and can be integrated with other circuits. The innovation of this research is to use PMMA instead of silicon material to reach the highly sensitive tunneling platform.

3.1 Structure Design

The all-PMMA-based tunneling sensor platform has been fabricated successfully. The fabricated tunneling sensor platform holds a membrane structure with a proof mass on the center. The counter electrode is set at a proper distance from the tip. The tip will produce tunneling current if it is biased at proper voltage (about 200 mV). By applying a force on the proof mass, the displacement change will incur a current change. The tunneling current change is then amplified. The output voltage will be as the feedback onto the deflection electrodes. The deflection voltage produces electrostatic force onto the counter electrodes to keep the gap between the electrode and the tunneling tip constant. Finally, the deflection electrode voltage, which is linearly proportional to the applied force, is read as the signal value.

In our designed magnetometer, a layer of ferromagnetic film (either Cobalt or Cobalt-Carbon composite) is deposited on the tunneling membrane. The tip-to-electrode displacement changes when a magnetic field is applied on the ferromagnetic film. The thickness of ferromagnetic film is from 250 to 300 nm, thick enough to be treated as "bulk" material. The illustration of the tunneling magnetometer cross section is shown in Figure 22.
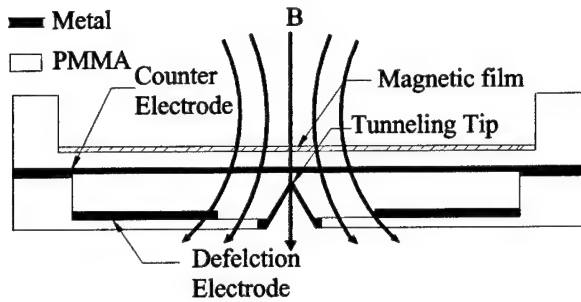
Fig. 22 Cross section view of tunneling magnetometer

3.2 Generation of Magnetic Field

There are two types of magnetic fields, the DC field and the AC field, which can be measured. The measurement of AC field is difficult because it needs a high quality magnetron shield instrument. The measurement of DC field is easier because the earth field has almost no effect on it even in an open environment. Usually, the AC field is generated by AC current in solenoid coils. The parameters of our solenoid coils are $30\times30\times48$mm in dimension, 300 turns. Calculated by formula, the DC field is $B_o = \mu_o NI/L = 78.5$G/A, where the μ_o is equal to $4\pi \times 10^{-7}\ Hm^{-1}$, defined as the permeability of the air. In order to enhance the field intensity, a ferromagnetic metal core is inserted into the coils. The measured value of DC field is about 950G/A, twelve times stronger than the calculation.

The generation condition of AC field may be challenging. There are two reasons. One reason is that the self-inductor of solenoid (the impedance of coil) is larger, which causes extremely small current. The other reason is that the bandwidth of Gauss meter is about 1 Hz. The high frequency AC field can not be measured by Gauss meter directly. Because the measurement of low frequency AC field (0-1 Hz) matched well with the calculation, the AC magnetic field used was then given by calculation.

3.3 Calculation of Magnetic Force

It is necessary to know the relationship between the magnetic intensity and the magnetic force. A calculation of magnetic force is from the view of magnetic energy gradient. The magnetomotive force is defined as mmf=NI, where N is the number of coils turns. The flux is $\Phi=BA$, where A is the area. The reluctance is $R=l/\mu_oA$, where l is the distance. The magnetic energy W is then:

$$W = \frac{R\Phi^2}{2}.$$

Due to $dW=0.2\Phi^2 dR+R\Phi d\Phi$, the magnetic force is derived as:

$$F = dW/dx = -\frac{1}{2}\Phi^2 \frac{dR}{dx} = \frac{\Phi^2}{2\mu A} = \frac{B^2 A}{2\mu}.$$

The force is propotional to the overlap area and the square of the field.

3.4 Measurement System

The measurement of mechanical response has been performed. The measurement system is shown in Figure 23. It includes a laser vibrometer, solenoid coils, and a Gauss meter. The purpose of this measurement is to obtain the displacement change of the membrane when magnetic force is applied. A monitor was used for the displacement measurement, and a current meter was used for magnetic field control. Although the signal was too weak to be measured, the measurement system was proven to be workable. The second-generation samples have been sent out for film deposition with different membrane thickness.
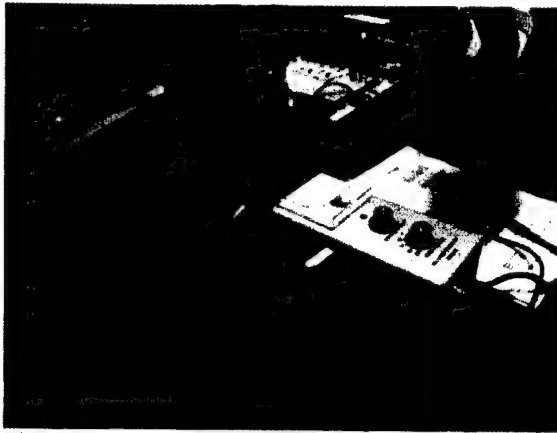
Fig. 23. measurement system for mechanical response

In summary, the all-PMMA-based magnetometer has been designed. The relations between magnetic field, magnetic force, and displacement changes have been calculated and derived. The measurement system has been set up.

4. Project 2 Presentation and Publications

(1) Jing Wang, Tianhong Cui, and Kody Varahramyan, "Synthesis and Fabrication of PMMA Tunneling Accelerometer", the fifth Texas MEMS Workshop, Texas, May 6, 2003.
(2) Yongjun Zhao and Tianhong Cui, "High-aspect-ratio Polymer-based Electrostatic Comb Drive by Hot Embossing Process", the fifth Texas MEMS Workshop, Texas, May 6, 2003.
(3) Jing Wang, Wei Xue, and Tianhong Cui, "A Combinative Technique to Fabricate Hot Embossing Master for PMMA Tunneling Sensors", accepted by journal of Microsystem Technologies.

5. Project 2 Patent Application

Tianhong Cui, Jing Wang, and Yongjun Zhao: "Polymer Based Tunneling Sensor", Application Serial No. 10/648,927 (filed on August 27, 2003).

Project 3

Bio-Inspired Optical Lens Materials and Structures with Dynamically Varying Refractive Index

Executive Summary

This presents the summary of the research conducted for developing the bio-inspired dynamically varying refractive index lens materials and miniaturized optical systems with reversibly varying focal lengths. Since the previous report, significant accomplishments have been made in the area of design and fabrication of dynamic lens system, and testing the mechanical and optical properties of polymer based lenses. In the initial phase of the research, experiments were conducted using a set of glass lenses to identify the right combination and configuration of lenses that can provide a wide angle of view. These results showed that a set of three concave lenses together with a single focusing convex lens can produce images with increased angle of view. The design concepts for fabricating the dynamic lens systems with different actuation mechanisms were developed and analyzed. One simple approach that was pursued to develop a variable focus lens involved the use of microfluidic lens structures. Some microfluidic driven lens structures were fabricated and the mechanical deflections of these lens structures have been tested. The change in fluidic pressure alters the radius of curvature and results in a change of the refractive power of the lens. Refractive optical fluids are either pumped into the lens compartment or removed from the already liquid filled compartment to have the convex and concave lens effects, respectively. The lens structures are made in several sizes to check the viability of activating the lenses, and also to characterize their imaging performances. In parallel, process technology was developed to fabricate the lenses on micro scale by microfabrication techniques. Efforts have also been made to fabricate dynamic optical systems by approaches highlighted below. The entire report consists of five parts. The first part discusses the fabrication and testing of the fluid-enabled optical lens system with variable focal length and wide angle of view. Several miniature lenses were fabricated and tested successfully. In the second part of the report, a variable focal length optical lens system is demonstrated by combining both fluidic and electrical actuation. Here a fluidic actuated micro lens system is integrated with the liquid crystal cell (LC) to further fine tune the focal length of the designed system. In the third part of this report, the efforts carried out on the integration of an electrowetting with a liquid crystal cell to form a variable focal length optical lens system is presented. The fourth part of the report focuses on the gradient refractive index lens structure development, followed by the fifth part of the report on actuator design and fabrication for refractive index control.

PART I: Design and Fabrication of Fluid Controlled Dynamic Optical Lens System

Introduction

The objective of this research has been to design and fabricate a novel miniature optical lens system which can mimic biological vision system and provide dynamically varying focal length and wide field of view. For advanced optical systems and devices such as, optical data reading scanners, focal plane arrays, security cameras, surgical instrumentation, etc., integrated microlenses with dynamic focal lengths and field of view are required.

Most animal eyes are based on the combination of curved lens surfaces and a radial symmetric variation of the refractive index within the bulk of the material. Although such graded lenses (GRIN) are well suited for imaging purposes, the difficult fabrication processes severely limits the wide spread use of GRIN lenses. Modern micro optical design and manufacturing are closely related to concepts and technology developed for semiconductor industry. This includes the general restriction to flat building parts (planar lens and receptor array), a matrix oriented patterning and the use of bulk materials which inherently limits the possibility of index modification.

Diffractive, refractive and graded index lenses are the three main types of microlenses which are commonly fabricated and commercially available to some extent. Diffractive microlenses are generally not well suited for imaging tasks as their focal length and efficiency depends strongly on the wavelength of the light and limits the lenses to monochromatic application. On the other hand, refractive lenses that can be used for imaging task are manufactured using resist reflow or melting resist techniques. However these lenses have limited field of view and do not exhibit dynamic features. Therefore an approach has been devised to design simple lens structures which can provide wide angle of view and tunable focal length. In this project, a novel system design with biconvex and biconcave lenses has been demonstrated as a variable focusing optical lens structure. The relation between the focal length of these lenses and the field of view has been studied and an optimum integrated system has been designed to have both wide field of view and dynamic focusing. The main application of this type of device can be in surveillance camera where both dynamic focus and wide angle view are required. Other application of this device can include endoscope surgical tools, and vertical optical scanners.

INITIAL EXPERIMENTATION

Preliminary experiments were conducted using different sets of double concave (DCV) and double convex (DCX) lenses with different focal lengths to understand the relationship between the field of view (FOV) and focal length of the lenses, and to find out the specific combination of lenses that can provide a wider FOV. These lenses were chosen because it is relatively easy to fabricate and make the polymer lens system adapt to one of these configurations. For the construction and characterization of fluid enabled optical systems, we realized that these simple experiments were critical to optimize the design process.

In one set of experiments, combinations of one DCX lens of fixed focal length and a second DCX or DCV glass lens of different focal length were used to image the object and determine the variation of FOV with the focal length of the second DCX or DCV lens (Figure 1a & 1b).

The first DCX lens was placed at a fixed position in front of the CCD camera to image the object. The position of the second DCX or DCV lens was varied to focus the object when lenses with different focal lengths were used.
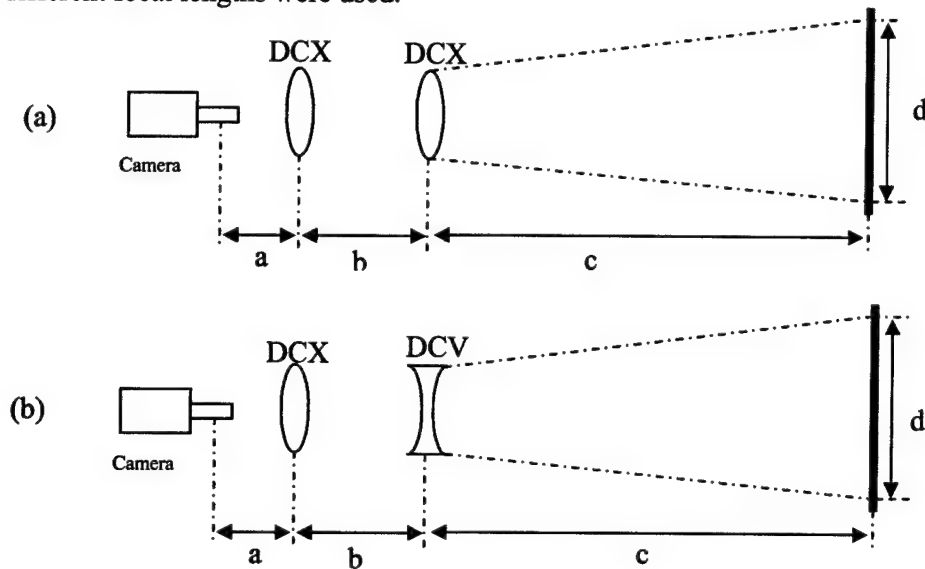

Figure 1: Illustrations of the optical arrangements: (a) DCX lens with another DCX lens; (b) DCX lens with a DCV lens.

Figure 2a shows the images taken using the setup shown in Figure 1a where the focal length (f) of first DCX was 10 cm and the focal lengths of the second DCX were 5 , 10, 15, 20 & 30 cm. Figure 2b shows the f of second DCX lens vs. field of view (FOV). It can be observed that as the f of DCX lens decreases, the FOV increases.

(a)

f = 30 cm   f = 20 cm   f = 15 cm

f = 10 cm   f = 5 cm
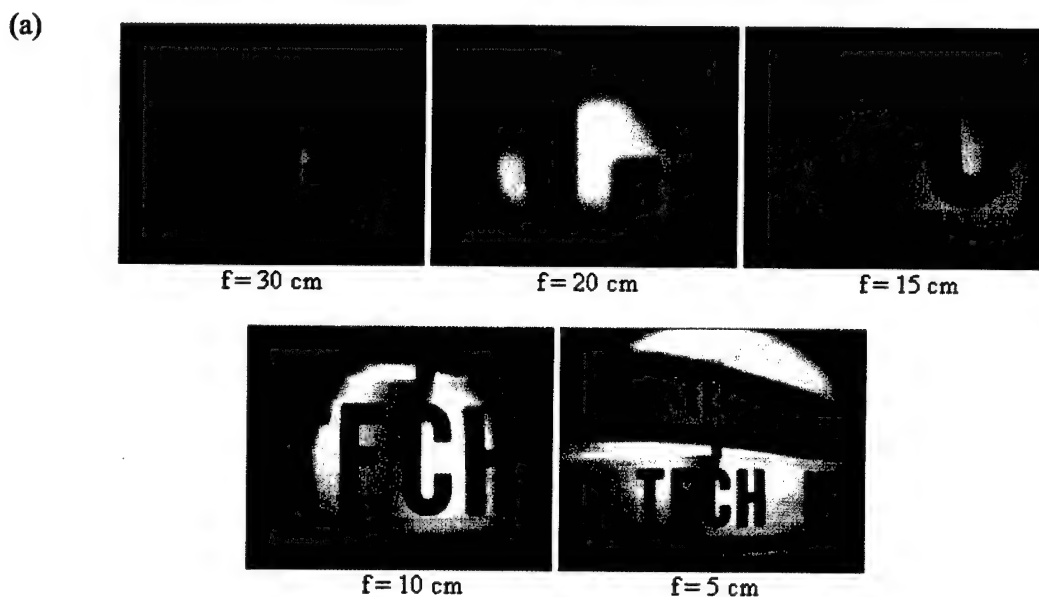
(b)
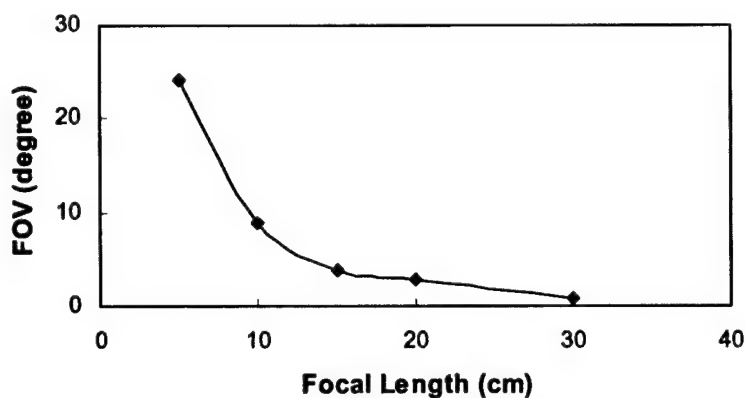
Figure 2: Images taken using the setup shown in figure 1a with first DCX lens of f = 10 cm and second DCX lens of different focal length. (b) Focal length vs. field of view (FOV) from two DCX lenses.

Figures 3a and 3b show the images captured using the setup shown in Figure 1a and 1b respectively, with first fixed DCX lens of focal length 20 cm in front of camera along with DCX and DCV lenses of different focal length (f = 10, 15, 20 cm), respectively. Figure 4 shows the plot of focal length vs. field of view for both DCX and DCV lenses. Although the observed FOV with these lenses are significantly lower, it should be noted that when DCV lenses are used to image the object one can achieve higher FOV, and as the focal length of DCV lenses decreases, the FOV increases.

f = 20 cm   f = 15 cm   f = 10 cm

(a)

f = 20 cm   f = 15 cm   f = 10 cm

(b)
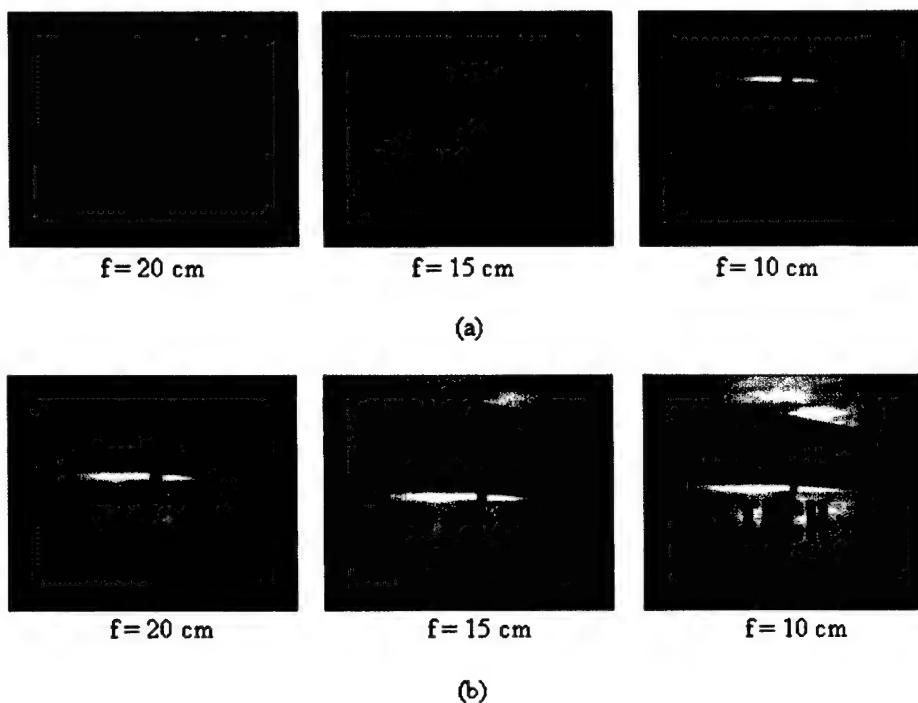
Figure 3: (a) Images taken using the setup shown in figure 1a with first DCX lens of f = 20 cm and a second DCX lens of f = 10, 15, and 20 cm; (b) Images taken using the setup shown in Figure 1b with first DCX lens of f = 20 cm and a second DCV lens of f = 10, 15, and 20 cm.
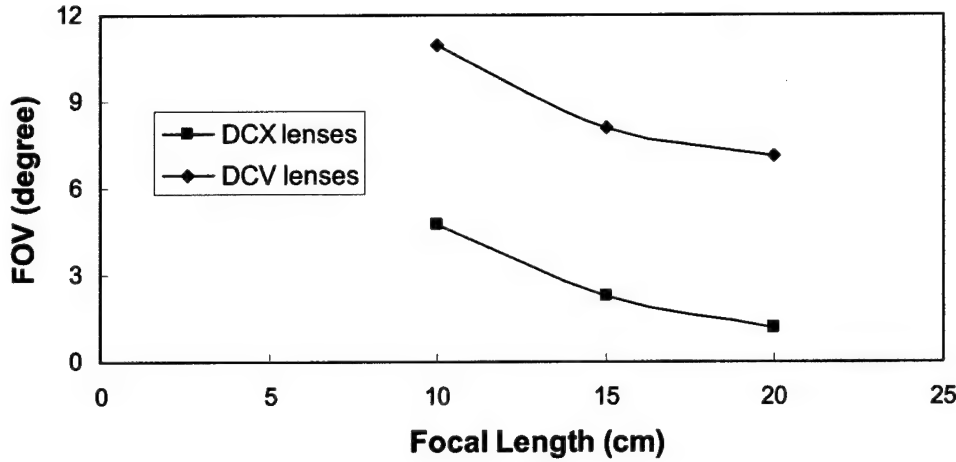
Figure 4: Focal length vs. field of view (FOV) from DCX and DCV lenses.

The focal length of the lenses can be further reduced by placing the two or three lenses in contact. The effective focal length (f_) of two DCV lenses of focal length $f_{c1\_}$ and $f_{c2\_}$ in contact is given by Equation 1.

$$\frac{1}{f_-} = \frac{1}{f_{c1-}} + \frac{1}{f_{c2-}} \tag{2}$$

Since it was found that the DCV lenses give higher field of view than DCX lenses, DCV lenses were chosen for further experiments to determine the variation of FOV with respect to the focal length of first DCX lens and with the combination of two or three DCV lenses of different focal lengths as shown in Figures 5a and 5b.

The focal lengths of first DCX lenses were 10, 20, or 30 cm, where as the focal lengths of DCV lenses were 10, 15, or 20 cm. In all the different arrangements of lenses, four different distances were marked. As shown in figure 5, 'a' is the distance between the camera and the DCX lens; 'b' is the distance between the DCX and DCV lens; 'c' is the distance between the DCV lenses and the object; 'd' is the length of the object that is viewed by the camera. The FOV (θ) is measured by using the formula given in Equation 2.

$$\theta = 2 * \tan^{-1}\left[\frac{(d/2)}{c}\right] \tag{2}$$

Table 1 and Table 2 show the measured FOV when the object was imaged using different configuration and combination of DCX and DCV lenses of different focal length as shown in Figure 5a and 5b.

Table 1: Angle of view measured using single double convex lens of focal length 10 cm and the different combinations of double concave lenses of focal length 10, 15 and 20 cm.

Single Convex lens F.L (cm)	Single Concave lens F.L (cm)	Two concave lens F.L (cm)	Three concave lens F.L (cm)	a (inches)	b (inches)	c (inches)	d (inches)	Angle of view (degrees) (θ)
10	10	-	-	2	0.5	37	9.5	14.5
10	-	10	-	2	1.5	35	18	29
10	-	-	10	2	2.5	34	26	42
10	15	-	-	-	-	-	-	-
10	-	15	-	2	1.5	37	12	18
10	-	-	15	2	1.5	34	13	21.5
10	20	-	-	-	-	-	-	-
10	-	20	-	-	-	-	-	-
10	-	-	20	2	1.5	35	12	19.5

Table 2: Angle of view measured using single double convex lens of focal length 20 cm and the different combinations of double concave lenses of focal length 10, 15 and 20 cm.

Single Convex lens (cm)	Single Concave lens (cm)	Two concave lens	Three concave lens	a (inches)	b (inches)	c (inches)	d (inches)	Angle of view (degrees) (θ)
20	10	-	-	2	3	30	25.5	46
20	-	10	-	2	3.5	31	32	54.5
20	-	-	10	2	4.5	32	52	78
20	15	-	-	2	1	36	22	34
20	-	15	-	2	2	34	24	39
20	-	-	15	2	3.5	33	28	46
20	20	-	-	2	0.5	36	21	32.5
20	-	20	-	2	2.5	33	22	37
20	-	-	20	2	4	32	23	40
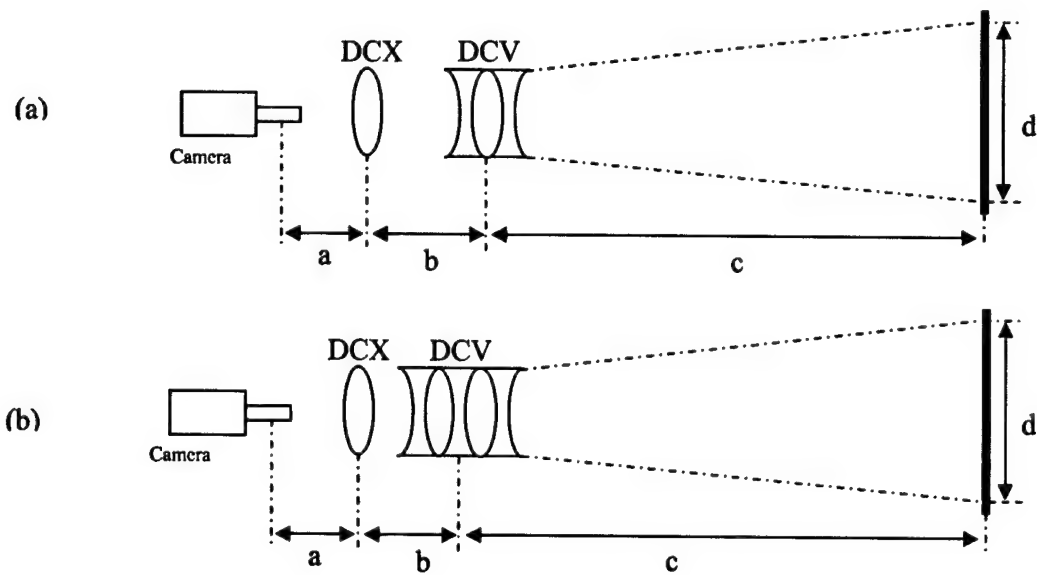
Figure 5: Illustrations of optical arrangements: (a) one DCX and two DCV lenses;
(b) one DCX and three DCV lenses.

Figure 6 shows the variation in the field of view as a function of focal length of DCV lenses. It can be observed that the FOV varies systematically depending on the focal length and the type of lenses used. The FOV from three DCV lenses joined together is much larger than that from a single DCV lens or two DCV lenses. These results indicate that the FOV increases with the decrease in the focal length of the DCV lenses used to image the object. Interestingly, the FOV also increased with the increase in the number of DCV lenses. The focal length of the first DCX lens used in front of camera to image the object also plays an important role in determining the FOV. If the focal length of this lens is higher, then the FOV will also be higher. The optical image with a minimum and a maximum FOV achieved from the above mentioned lens configurations are illustrated in Figure 7a and 7b, respectively.
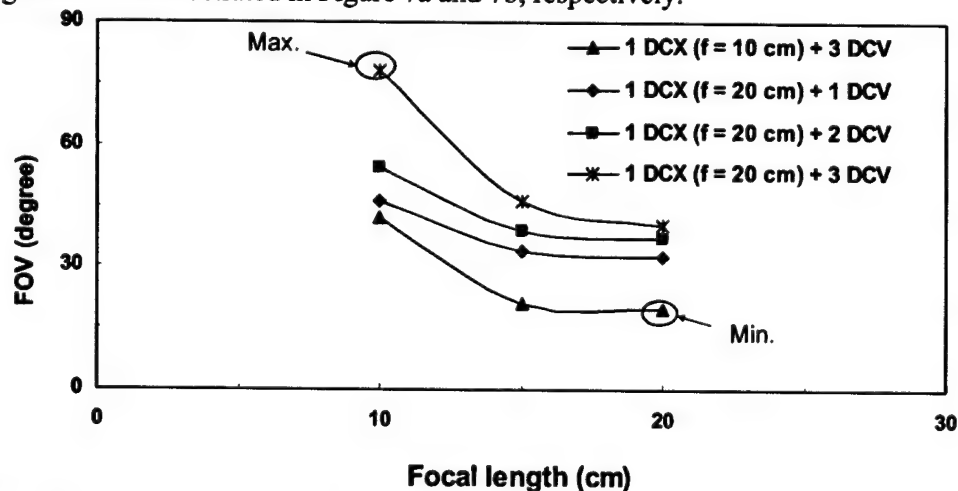
Figure 6: Focal length of DCV lenses vs. FOV for different combinations of DCX and DCV lenses. The focal length of DCX lens is fixed in each series of imaging experiment.
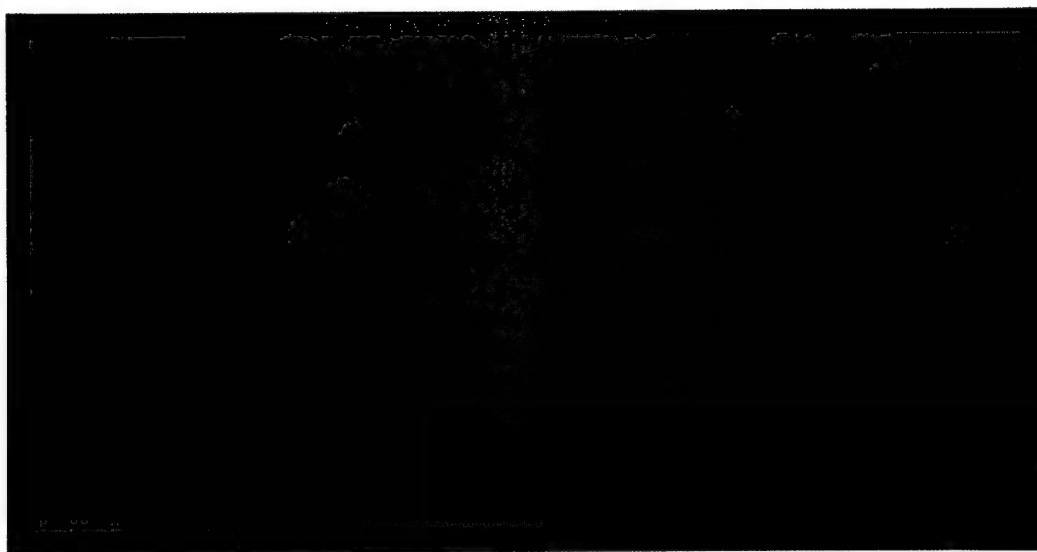
(a)
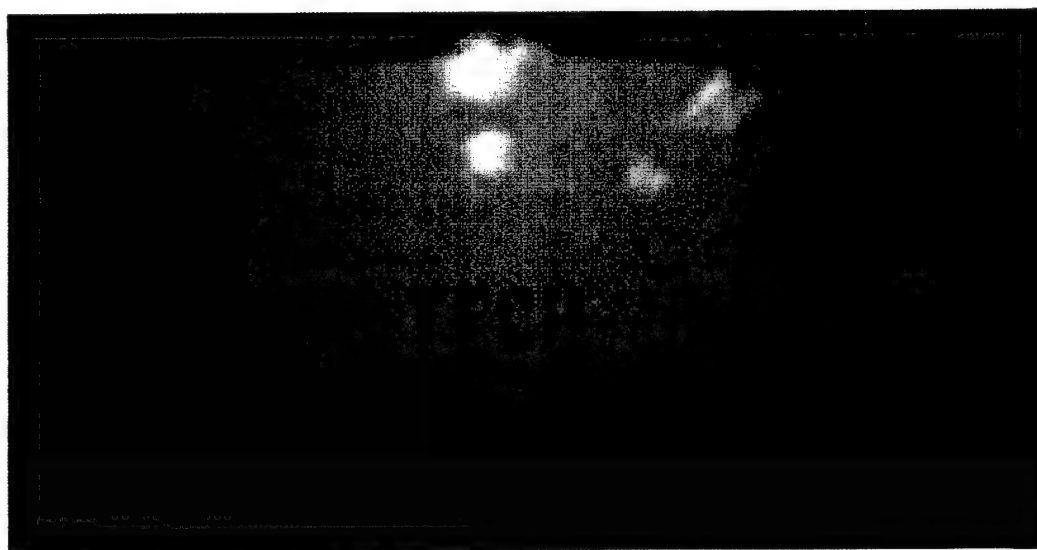
(b)

Figure 7: Image of the object captured using (a) a DCX lens (f = 10 cm) and
a DCV lens (f = 10 cm); (b) a single DCX lens (f = 20 cm)
and three DCV lenses (f = 10 cm).

DYNAMIC (VARIABLE) FOCAL LENGTH SYSTEMS

The results obtained from the above mentioned experiments were found to be useful for designing and fabricating an optical system with similar combination of lenses as tested above using optically transparent flexible materials. The reason behind using the flexible lens material is that, by varying the radius of curvature of these lenses dynamically by pumping liquid into and out of the lens chamber, one can achieve variable focal length and FOV. Since

polydimethylsiloxane (PDMS) is the choice of material for optical transparency, durability, flexibility and bio-compatibility films, several polymer lenses were made in different sizes by casting PDMS material in suitable size of circular molds. After curing, two PDMS membranes were combined by placing a spacer in between, and the whole assembly was sealed and made leak proof. A small hole was made in the spacer unit to fabricate the channel for pumping liquid with high refractive index (in this case DI water), into and out of the chamber formed by the spacer unit by means of a syringe pump.

For each size of the lenses, the volume (v_c) of the lens chamber was calculated by determining the diameter and the thickness of the spacer unit, by assuming the PDMS membrane is flat. However, in reality, the PDMS membrane does not remain flat. First, the optical fluid (DI water) was pumped into the lens chamber until the chamber was filled and the membrane becomes flat. At this point, the volume of the liquid (v_1) necessary to fill the chamber without any noticeable curvature of the membrane was monitored. The small discrepancy between the calculated (v_c) and measured values (v_1) can be attributed to the sealing joints inside the chamber that would reduce the available space. As mentioned earlier, pumping more liquid into lens the chamber will make it behave like a DCX lens. Whereas removal of the liquid from the lens chamber will make it behave like a DCV lens.

In the case of DCX lens configuration, the maximum amount of liquid (v_2) that can be pumped into the lens chamber without rupturing the lens membrane is measured. If we define v_3 as the difference between v_2 and v_1 ($v_3 = v_2 - v_1$), then v_3 represents the amount of liquid that was actually used to cause the deflection of the membranes to form DCX lens. Similarly, in the case of DCV lens configuration, the maximum amount of liquid (v_4) can be defined as the amount that can be pumped out from the already liquid filled (v_1) lens chamber. Theoretically, v_1 and v_4 are expected to be same. The difference (v_5) between v_1 and v_4 would represent the amount of liquid trapped in the chamber ($v_5 = v_1 - v_4$).

The geometrical deflection of the membrane as a result of pumping liquid into the lens compartment is shown in the Figure 8, and the associated volume of the lens chamber above the spacer chamber is calculated by using the formula for a spherical cap as given in Equation 3.

$$\frac{v_3}{2} = (\frac{\pi}{6})(3r_1^2 + h^2)h \qquad (3)$$

From Equation 3, when the volume (v_3) and the radius of spacer unit (r_1) are known, then maximum deflection at the centre of the membrane (h) can be calculated. Once h is known, the radius of curvature of the lens chamber (r_2) can be calculated using the Equation 4.

$$r_2 = \frac{(h^2 + r_1^2)}{2h} \qquad (4)$$
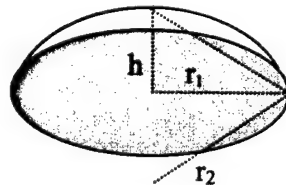
Figure 8: Schematic diagram showing the lens chamber above the spacer chamber;

From the radius of curvature of the lens, the focal length (f) can be calculated using the formula given in Equation 5. Figure 9 shows the plot of focal length vs. volume of liquid pumped-in when a lens unit with spacer of 7.9 mm radius is used.

$$f = \frac{n_2 \times r_2}{n_2 - n_1} \tag{5}$$
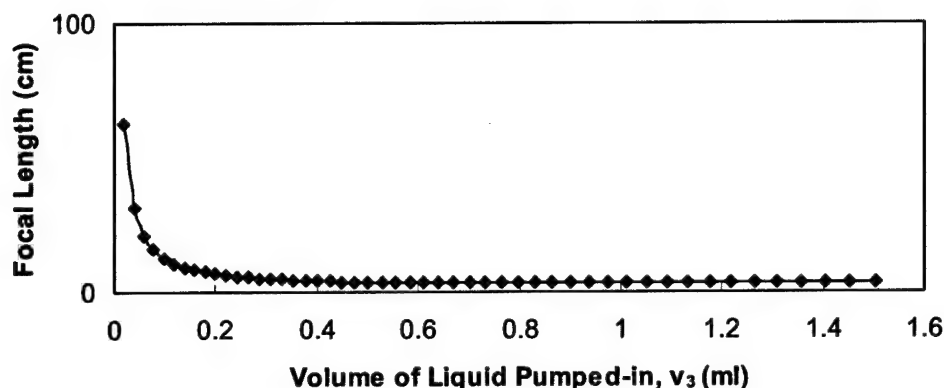
Figure 9: Focal length (f) vs. Volume of liquid pumped-in (v₃).

Imaging of the object was done with different combinations of dynamic lenses. Syringe pump was used to increase or decrease the liquid in the chamber each time, and the image was captured for each liquid level.

First a single dynamic lens was used in DCX configuration by pumping liquid into the lens chamber (0.02 ml each time) to view the object. A static DCX glass lens was placed between the dynamic lens and the camera to image the object along with a dynamic lens configured as DCX lens as shown in figure 10. Figure 11 shows the images captured by pumping different volume of fluid into the lens chamber.
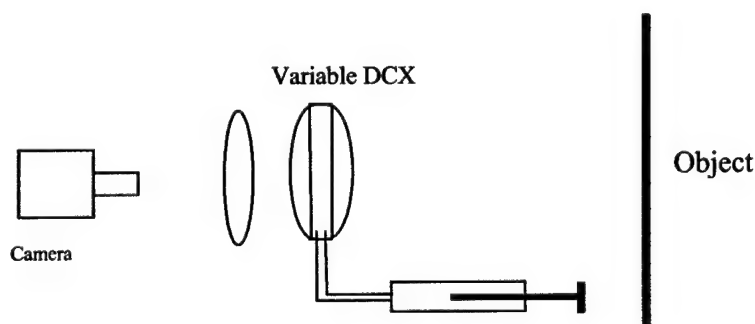
Figure 10: Setup for fixed DCX glass lens of focal length 10 cm and a single dynamic DCX lens.

v₃ = 0.1 ml   v₃ = 0.2 ml   v₃ = 0.3 ml

v₃ = 0.4 ml   v₃ = 0.5 ml
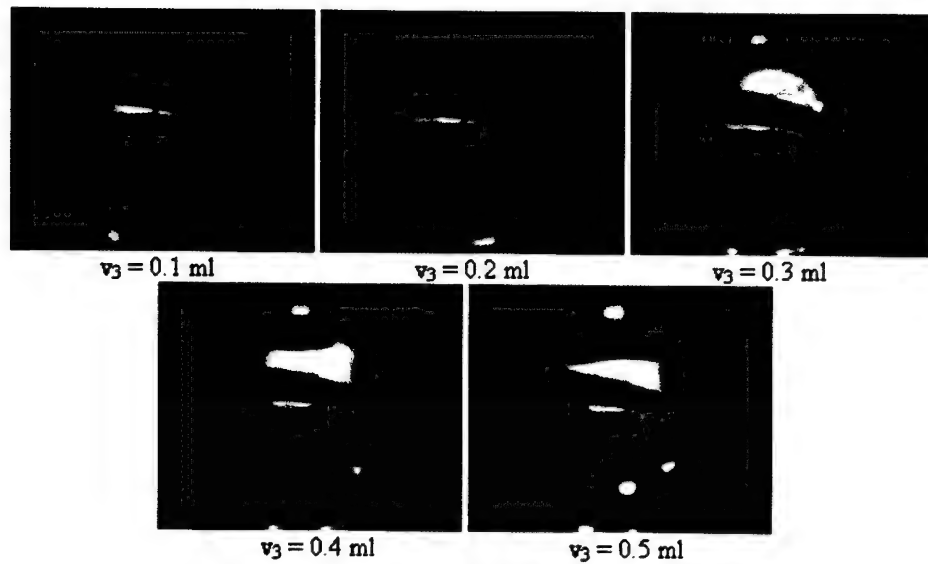
Figure 11: Images captured at different volume of fluid (v_3) pumped into the lens chamber using a variable focal length DCX lens.

Figure 12 shows the variation of FOV and focal length with respect to the volume of liquid that was pumped-in. It can be observed that as the liquid was pumped into the lens chamber, the focal length of the lens decreases as a result of decrease in the radius of curvature. It can also be observed that as the focal length of this dynamic DCX lens decrease the field of view increases as in the case of static lenses. Figure 13 shows the variation of distance between the first fixed DCX lens and the variable focal length at each volume of liquid pumped-in (focal length) to bring the fixed object into focus.
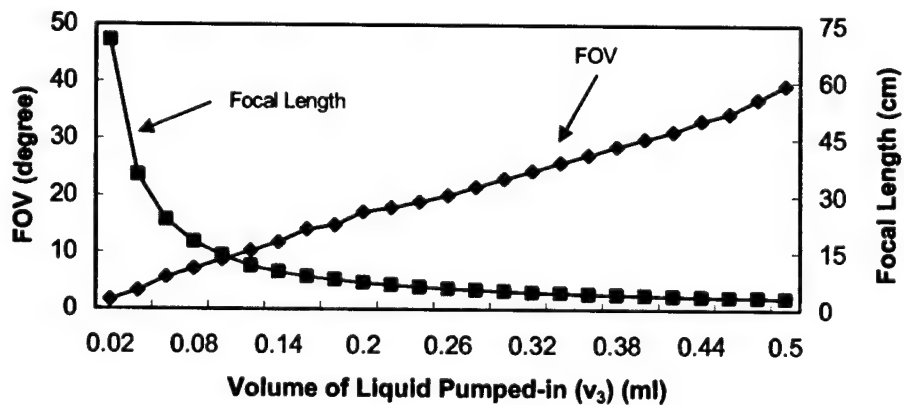
Figure 12: (a) Variation in the FOV and focal length as a function of the volume of liquid (v_3) pumped into the lens
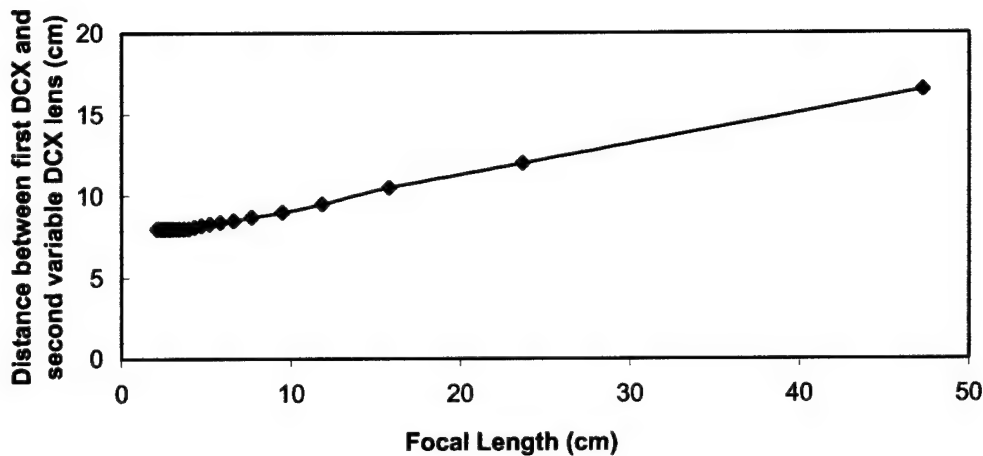
Figure 13: Focal length vs. Distance between the first fixed DCX and single second variable DCX lens.

In another experiment a single dynamic lens was used in DCV configuration by pumping liquid out of the lens chamber (0.02 ml each time) to view the object. The same static DCX lens (f = 10 cm) was used in front of the camera to image the object. In the set of experiments that followed, the object was imaged using two or three dynamic lenses in DCV configuration by pumping liquid out (0.02 ml each time) identically from all the lenses. Figure 14a shows the images of the object captured when the dynamic lens was used as DCV lens by pumping liquid out of the lens chamber. It should be noted that for this particular lens structure, a maximum of 0.18 ml, could be pumped out. Since it was found that two or three DCV lenses are essential for achieving wide angle view, the two or three dynamic lens structure was made by assembling identical lens structures on top of one another. For the sake of simplicity, all the lens chambers were activated in the same manner. Figures 14b and 14c show the images captured using two and three dynamic DCV lens in contact respectively. It can be observed from Figures 14b and 14c that as the liquid was pumped out of the lens chamber, the focal length of the formed concave lens decreases and larger field of view can be imaged as observed with the static lenses.
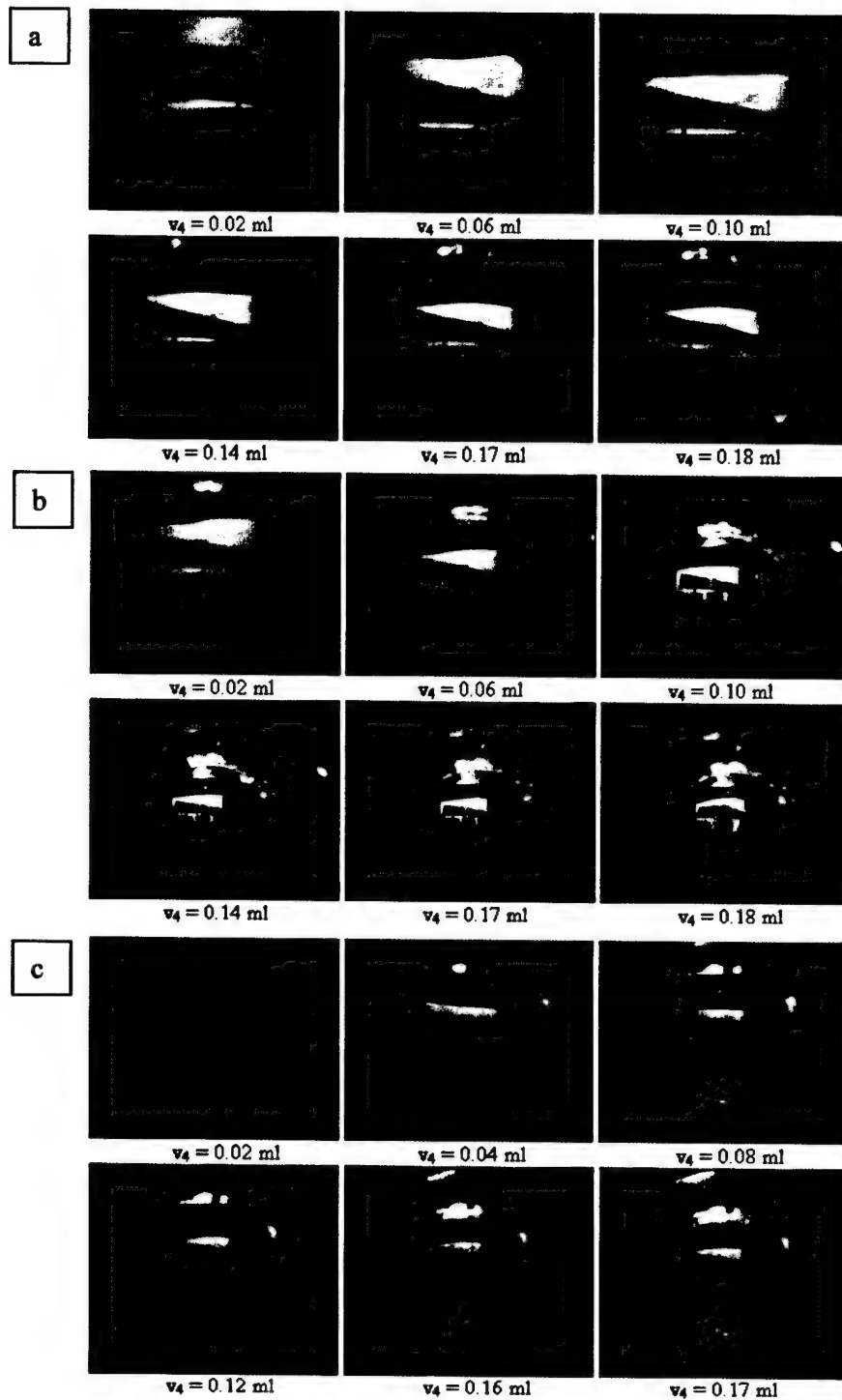
Figure 14: Images of the object captured with (a) single variable DCV lens; (b) two variable DCV lens system; (c) three variable focal length DCV lens system at different volume of fluid (v_4) pumped-out.

Figure 15a shows the three DCV lens system fixed on an optical post. Figure 15b shows the image captured using this three lens system by pumping-out maximum amount of liquid (0.17 ml) before the lenses were ruptured. It can be observed that when the FOV is increased, the images became small. Thus, further increasing the number of concave lenses to increase the FOV will make the image smaller which make it difficult to distinguish the fine details of the object.

(a)   (b)
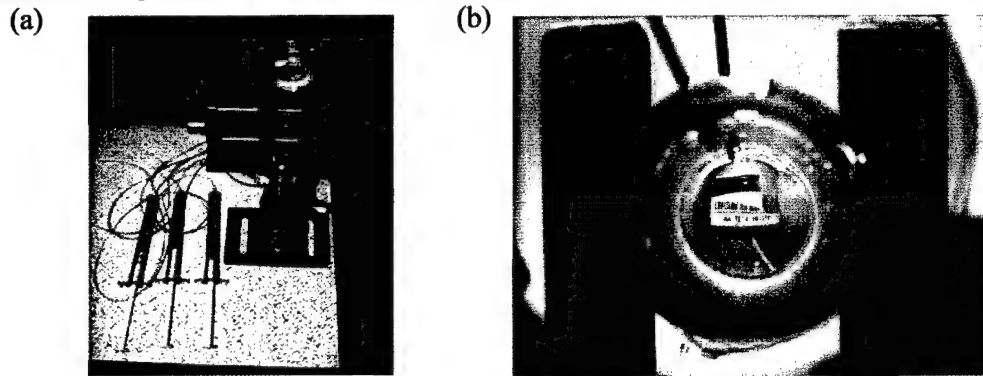
Figure 15: (a) Three lens system with fluidic connections; (b) Object imaged through dynamic hree DCV lens system.

The field of view achieved using single, two and three dynamic lens structures was measured at each level of volume of liquid pumped-out. Figure 16a, 16b and 16c show the variation in effective focal length and FOV with respect to the volume of liquid pumped out of the lens chamber for single, two and three dynamic lens systems, respectively. The maximum FOV achieved with single dynamic lens was 60^0. It should be noted that the FOV increases when two DCV lenses are used to image the object rather than one DCV lens or DCX lens as observed for static glass lenses. With these two DCV lens system, the maximum FOV that can be achieved was 104 degree. The FOV further increased when three DCV lens were used to image the object rather than two or one DCV lenses as observed in case of static glass lenses. With this lens system the achievable FOV was 120 degree. Figure 16a, 16b and 16c show the plot of variation in the distance between the first fixed DCX lens and the single, two and three dynamic varying DCV lens system, respectively to bring the object into focus with respect to the focal length.
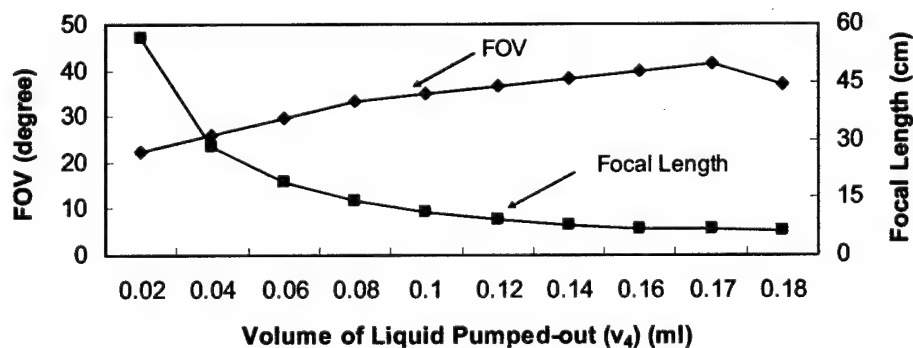
(a)
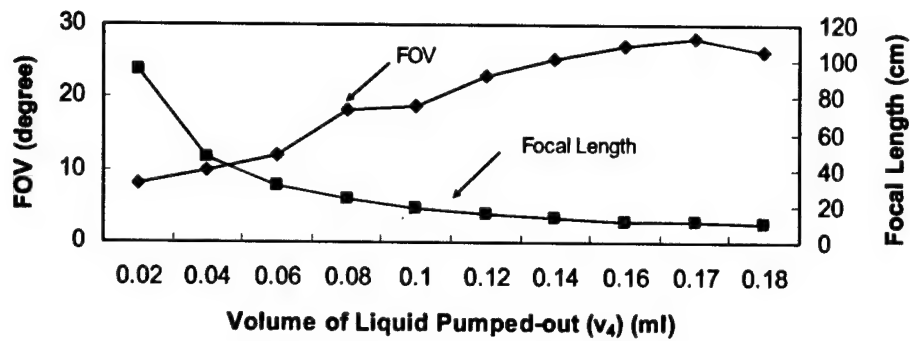
(b)
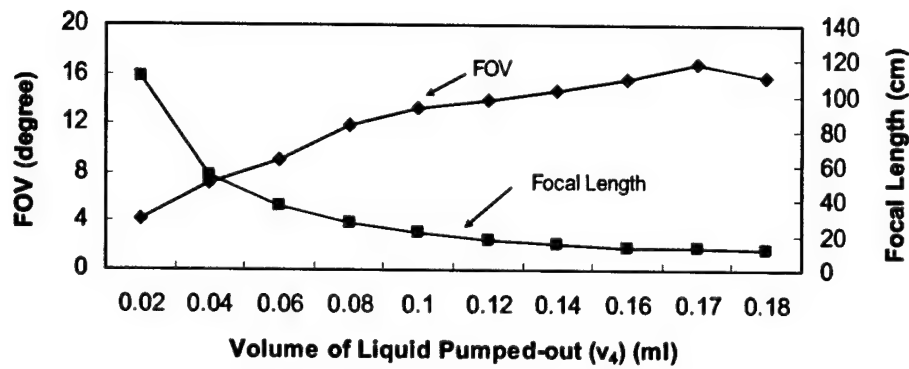
(c)

Figure 16: Variation in the focal length and the field of view (FOV) achieved as a function of the volume of liquid (v_4) pumped out of the lens chamber using (a) single DCV lens; (b) two DCV lenses; (c) three DCV lenses.
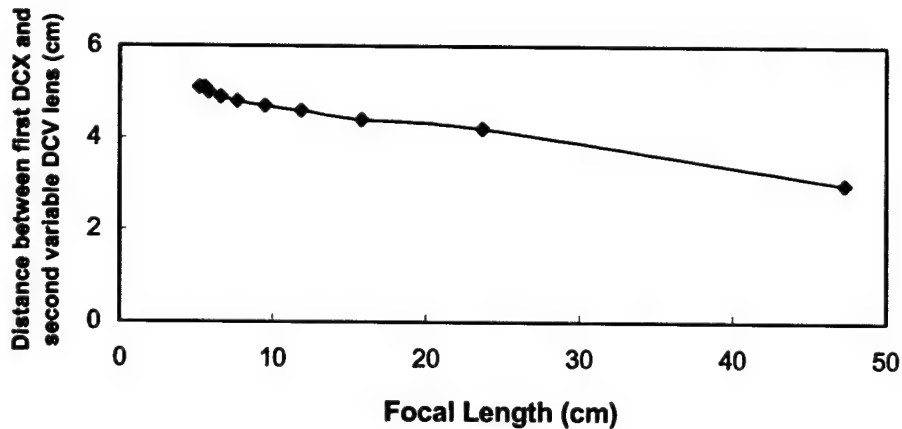
(a)
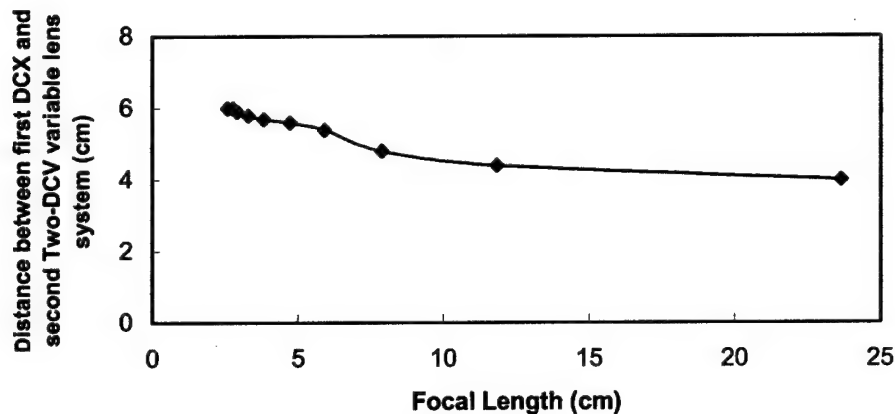
(b)
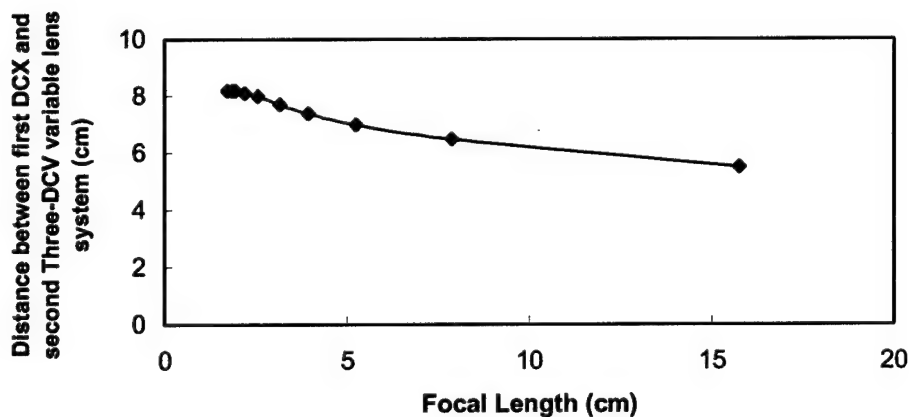
(c)

Figure 17: Focal length vs. Distance between the first fixed DCX and (a) single variable
DCV lens; (b) Two DCV lens system; (c) Three DCV lens system.

DYNAMIC VARIABLE FOCAL LENGTH MICROLENSES

The designed dynamic varying focal length lens systems were fabricated in microscale and their
characteristics were tested. First a mask was designed to fabricate the lens chamber and the
fluidic channels of different dimensions using L-Edit. L-Edit mask designing program is a part of
complete integrated circuit design tools suite offered by Tanner Research Inc. It is a low-level,
fully customized mask editor. It does not perform automatic layer transformations. That is, there
is no automatic wee or selected generation for CMOS processes. Although wells and selects
must be generated manually, this can be done more quickly than with other "high-level" tools
because of L-Edit's intuitive user interface. In addition, using L-Edit one can construct special
structures to utilize a technology without worrying about problems caused by automatic
transformations. Figure 18 shows the layout of the lens chamber and spacer with fluidic channel
of different dimensions.
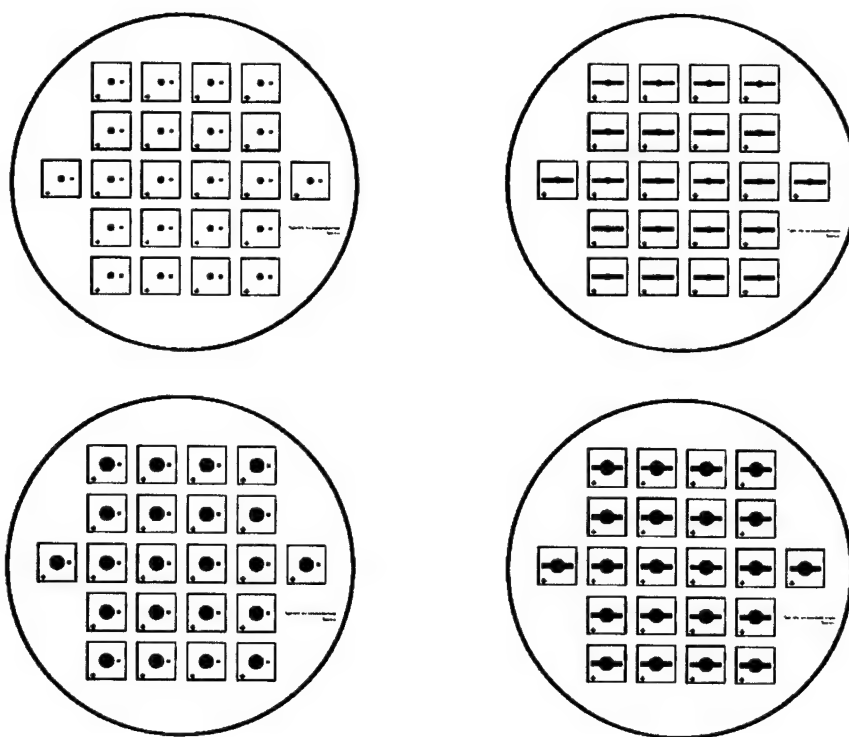
Figure 18: Mask layout for different dimension of lens chamber with inlet and spacer with fluidic channel.

FABRICATION PROCESS

The fabrication steps involved to fabricate the dynamic varying focal length lens system are shown in Figure 19.
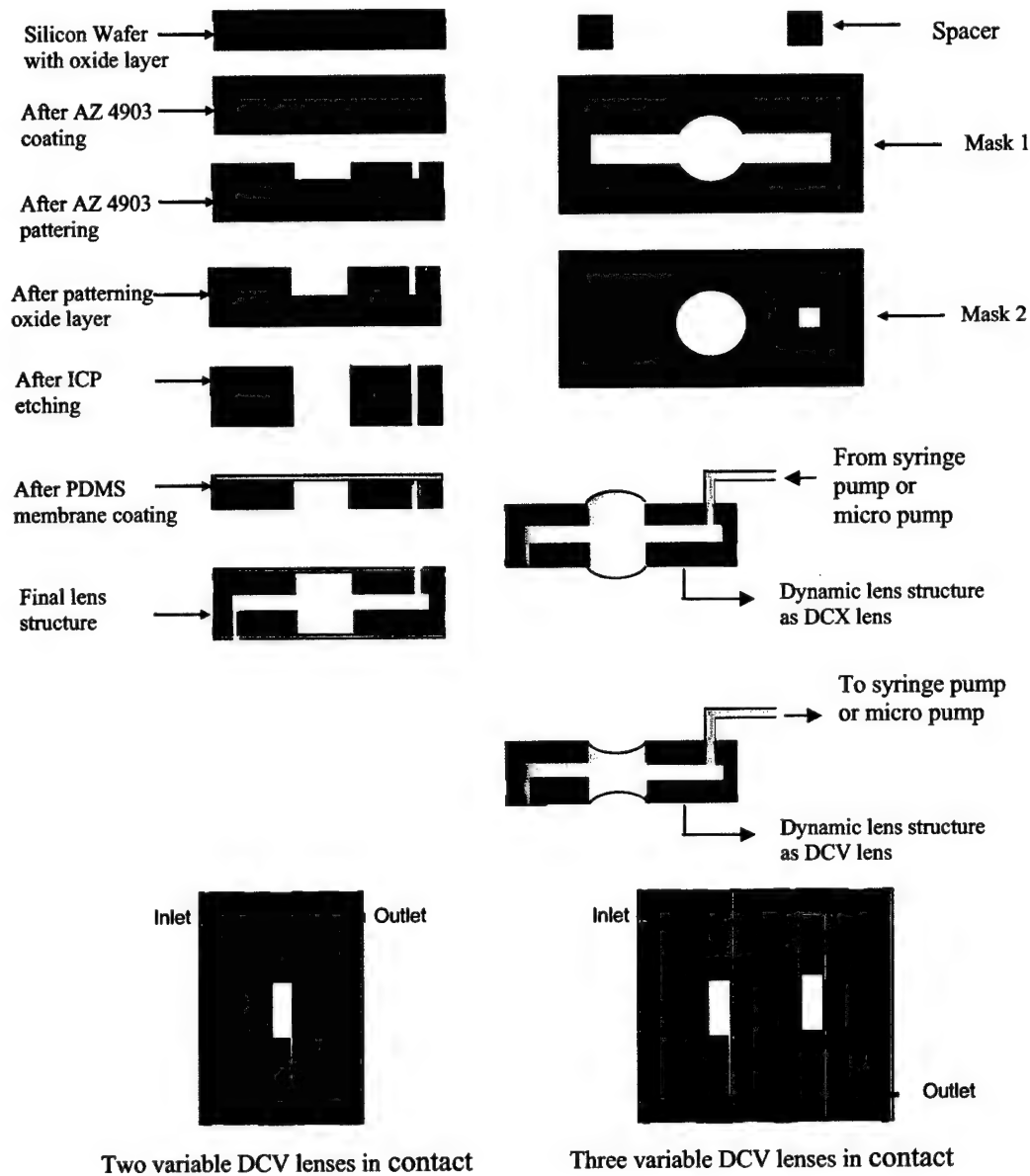
Figure 19: Fabrication steps for dynamic varying focal length lens systems.

LITHOGRAPHY AND ICP ETCHING

The silicon wafer <100> used for the fabrication had an oxide layer of 2 um. This oxide layer can be used as mask for ICP etching process. Also it is known that PDMS stick well with SiO_2 layer. A positive photoresist can be used for masking the oxide layer during both BOE etching (to pattern the oxide layer) and ICP etching (to etch through the silicon). Before ICP etching the oxide layer was patterned using the designed mask layout. The pattern transfer was performed lithographically on a commercially available AZ 4903 positive resist using the I-line of Hg-lamp. Since this new resist is quite viscous, it could be spun into thick layers on silicon wafers at a spin rate of 700-2000 rpm. All the silicon wafers used for the lithography process were first cleaned with acetone and isopropyl (IPA) to remove any organic impurities from the surface, before actually starting the lithographic process steps. Then the substrates were pre-baked at 115°C for 10 min. After they reached room temperature, they were coated with an adhesion promoter known as HMDS which increases the adhesion between the positive photoresist and the substrates. The spin curve for HMDS coating is given in Figure 20.
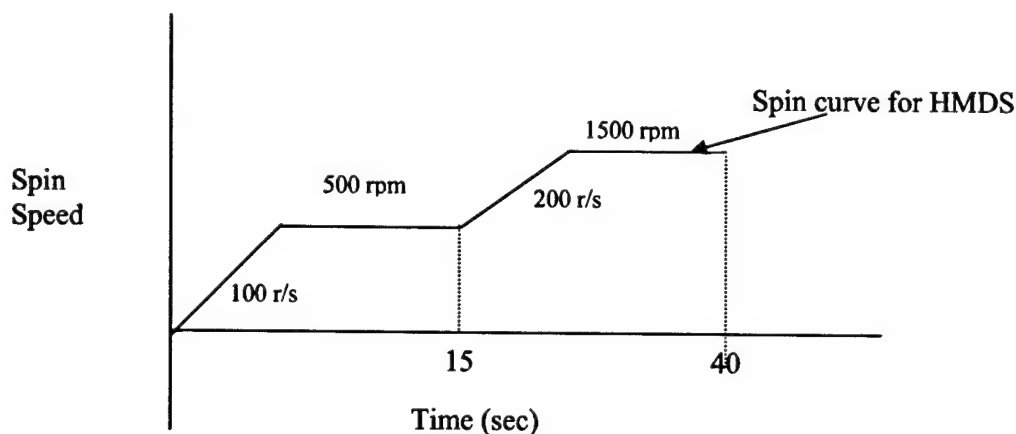
Figure 20: Spin curve for the adhesion promoter (HMDS) coating.

Approximately 4 ml of AZ 4903 was dispensed on the wafer and spun according to the spin curve shown in Figure 21. Soft baking was done at 60 degrees for 4 min, 70 degrees for 1 min, 90 degrees 2 min and 110 degrees for 3 min. After alignment with a photomask, the resist-coated substrate was exposed to UV-light for 100 sec. For the resist samples developed using MF 319 developer, the patterns were not well-developed leaving many residues on the developed area, whereas those developed with AZ 400K developer were found to be fully developed and transferred onto the substrate.
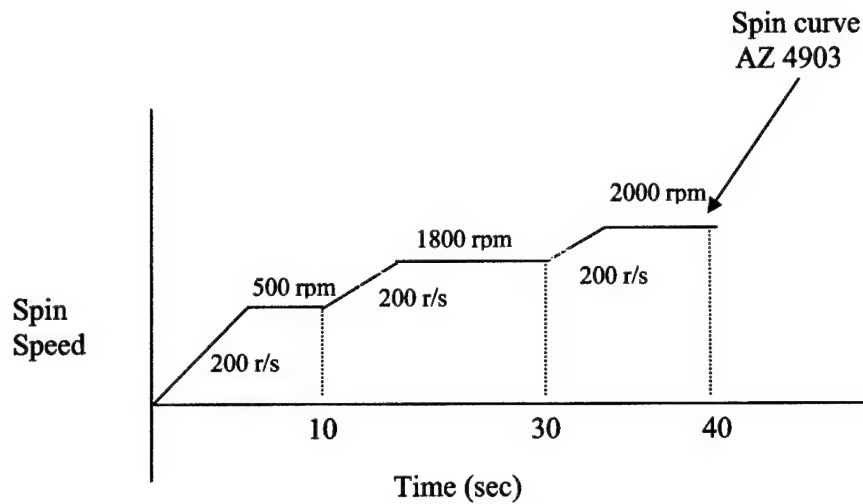
Figure 21: Spin curve for AZ 4903 resist used in the process.

The thickness of the resist layer was measured, and patterned structures were examined by optical microscope and scanning electron microscope (SEM) to check for any deformities. Figure 22 shows the SEM images of the test patterns after lithography process.
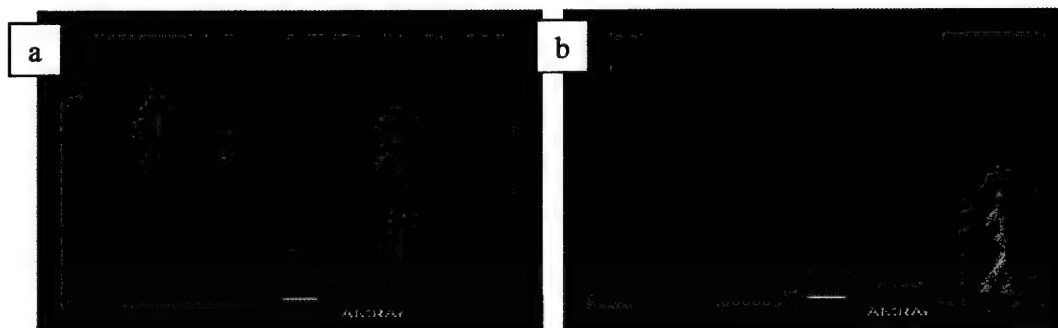
Figure 22: SEM images of the patterned AZ 4903 resist.

Figure 22b shows the SEM image of the test pattern under high magnification. This figure shows that the sidewalls of the pattern are nearly vertical and rough. The average thickness of the AZ 4903 patterns was measured to be 22.79 μm. Figure 23 shows the step profile measured using Tencor step profilometer.

Pos (L)	643.61 µm
Pos (R)	1253.2 µm
Height (L)	-22.884 µm
Height (R)	-0.091374 µm
Width	609.63 µm
Height	22.793 µm
TIR	22.82 µm
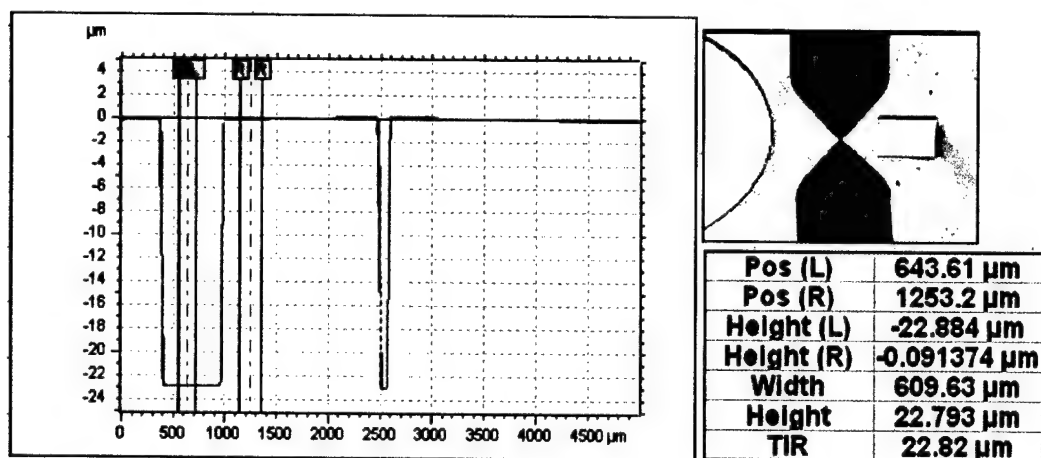
Figure 23: Step profile of the AZ 4903 pattern measured using Tencor.

After the lithography process the sample was subject to BOE etching to remove the oxide layer from the patterned structure. Then the sample was given for ICP etching. The processing conditions used for ICP to etch through the patterns in the silicon wafer are given below.

Table 3: Parameters used for ICP etching

Power	1800 W
Bias	30 W
SF_6 Flow rate	300 ccm/sec for 7 sec
C_4F_8 Flow rate	50 ccm/sec for 3 sec
Pressure	18 % open area of the valve.
Temperature	18.6 °C
He regulation	7.5 E +03
Etching time	1 h 15 min

The patterns after ICP etching are shown in Figure 24. It can be observed that photoresist was able to withstand in ICP thereby protecting the oxide layer under it. Figure 25 shows the step profile of the photoresist AZ 4903 after ICP etching. The step height was measure to be 18.51 um that is only 3 um of AZ 4903 layer was etched during ICP process. Therefore it can be implied that AZ 4903 has a very low etch rate in ICP and can be used as good masking layer.
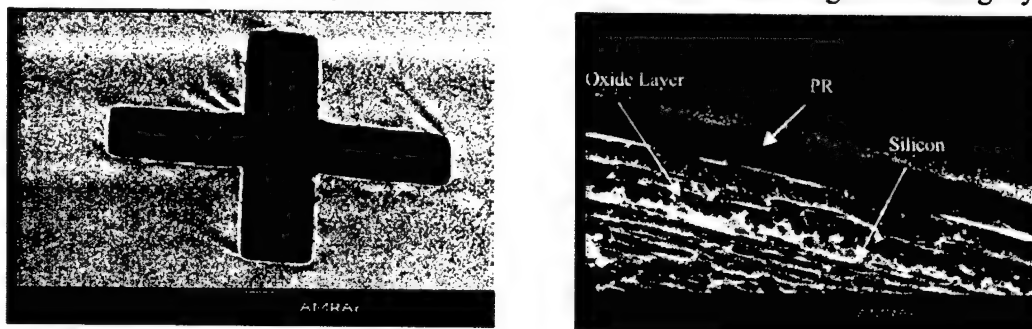
Figure 24: Patterns after ICP etching.

Pos (L)	603.81 µm
Pos (R)	2568.2 µm
Height (L)	-0.011224 µm
Height (R)	-18.521 µm
Width	1964.4 µm
Height	-18.51 µm
TIR	18.69 µm
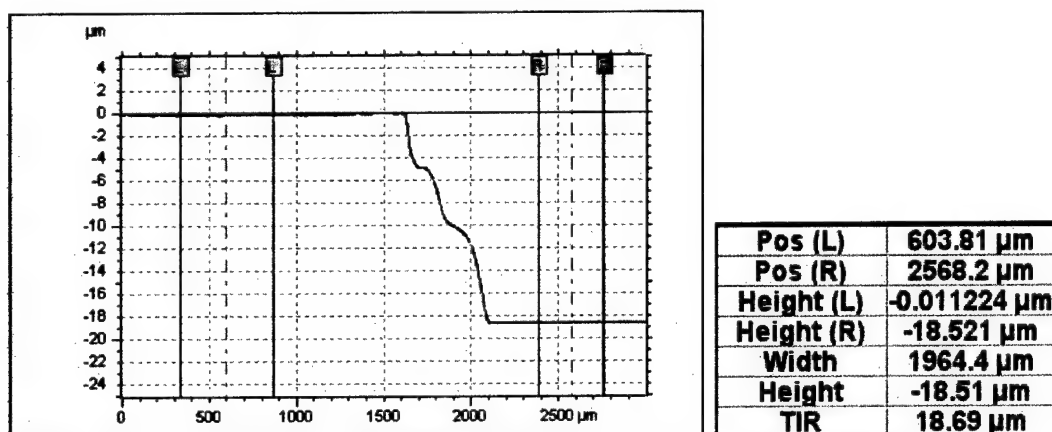
Figure 25: Step profile of AZ 4903 after ICP etching process.

Figure 26 shows the optical image of the lens chamber and fluidic inlet after ICP etching process. From Figure 26a it can be observed that the photoresist did show any sign of burnt or pealing of during the process. Figure 26b shows the pattern after complete ICP etching and washing away the photoresist. Figure 27 shows the SEM micrograph of the lens chamber with inlet and spacer with fluidic channel.
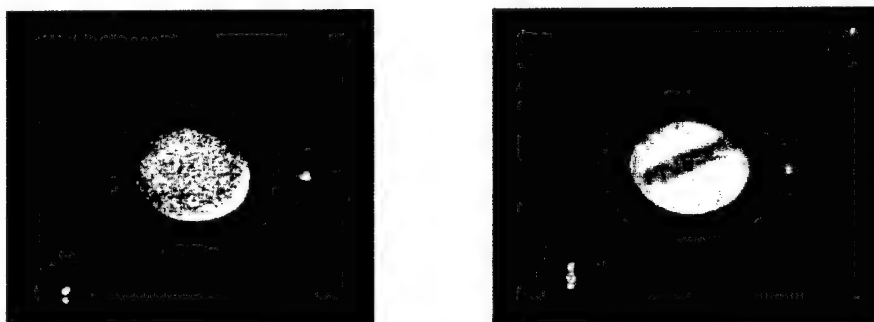
Figure 26: (a) Lens chamber and fluidic inlet after ICP etching with photoresist;
(b) Lens chamber and fluidic inlet after complete ICP etching and removing photoresist.
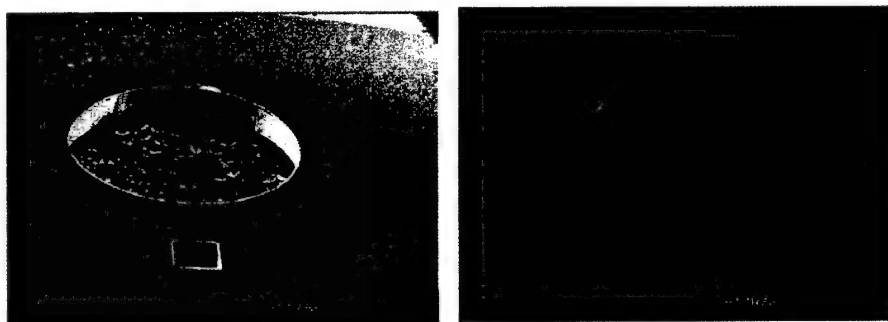
Figure 27: SEM micrograph of (a) Lens chamber with fluidic inlet; (b) Spacer with fluidic channel.

INTEGRATION AND PACKAGING

To form PDMS membrane a silicon wafer was pretreated with Trichlorosilane (Tridecafluoro-1,1,2,2-Tetrahydrooctyl) under vacuum for 2 hour. PDMS was spun on this wafer at 1500 rpm for 45 sec. PDMS membrane so formed was cured at 50 $^{\circ}$C for 30 min and 90 $^{\circ}$C for 15 min. After curing this membrane was transferred to the ICP etched sample with the lens chamber to form flexible membrane. When two lens chamber with PDMS membrane were formed they were stick together with a spacer aligning the fluidic inlet and channel. To protect the PDMS membrane an extra peace of lens chamber was fixed on either side of the lens structure. The final lens with fluidic connection is shown in Figure 28. The total size is 1 cm x 1 cm x 1.5 mm. The lens is 2 mm in radius.
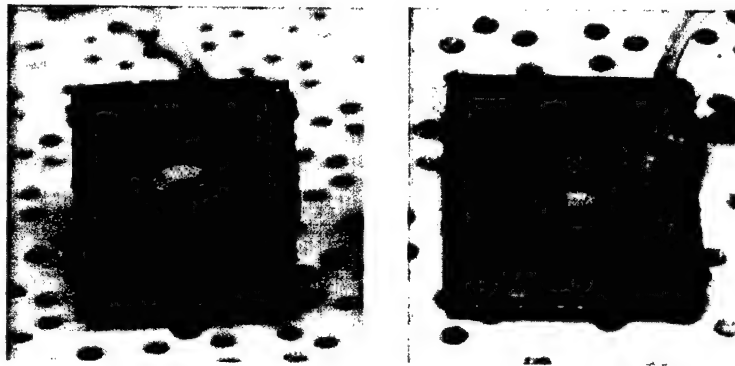
Figure 28: Dynamic focus lens structure with fluidic chamber and inlet connection.

TESTING

The dynamic lens structure was first activated as DCX lens by pumping optical fluid (DI water) with the help of syringe pump. Initially the lens chamber was filled with fluid (v_1). The images were captured by directly viewing the object through the lens structure. The liquid was pumped in at the rate of 3 μl/min and images were capture every 10 sec that is at every 0.5 μl (v_3) of fluid pumped into the lens chamber. Next the lens was activated as DCV lens by pumping-out fluid from the lens chamber from initial point. The liquid was pumped-out at the rate of 3 μl/min and images were capture every 10 sec that is at every 0.5 μl (v_4) of fluid pumped out of the lens chamber. Figure 29a and 29b shows some of the images taken by activating the lens as DCX and DCV lens respectively. Figure 30a shows the variation in focal length and FOV with respect to the volume of liquid pumped-in. It can be observed that as the liquid was pumped into or out of the lens chamber, the focal length of the DCX or DCV lens decreases as a result of decrease in the radius of curvature. It can also be observed that as the focal length of this dynamic DCX lens decrease the FOV increases. The maximum FOV achieved with single dynamic DCX lens was 61^0. Figure 30b show the variation in effective focal length and FOV when the lens structure was activated as DCV lens with respect to the volume of liquid pumped out of the lens chamber. The maximum FOV achieved with single dynamic DCV lens was 68.2^0. Figure 31a and 31b shows the variation of distance between the variable focal length lens at each volume of liquid pumped-in and pumped-out respectively to bring the fixed object into focus.
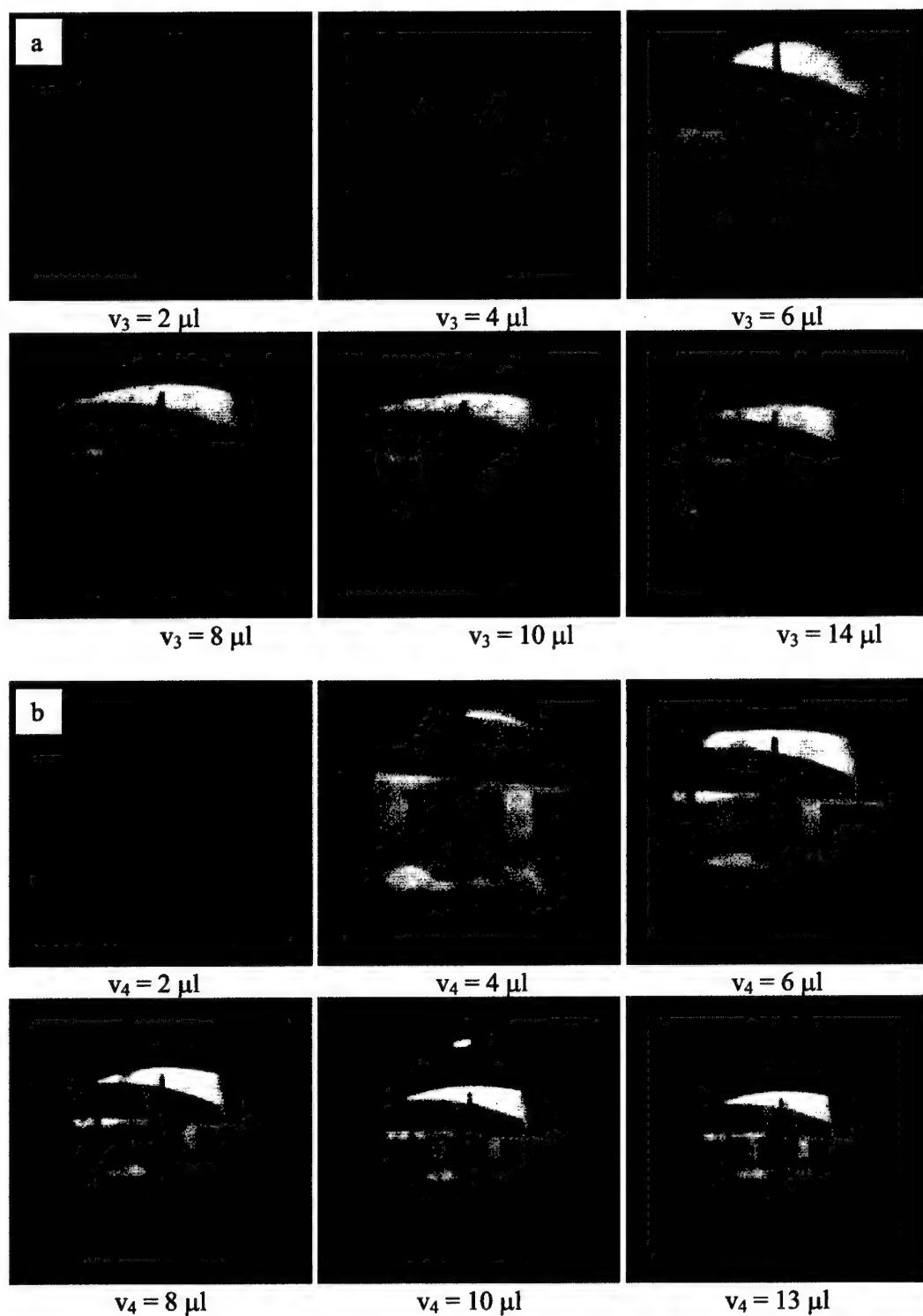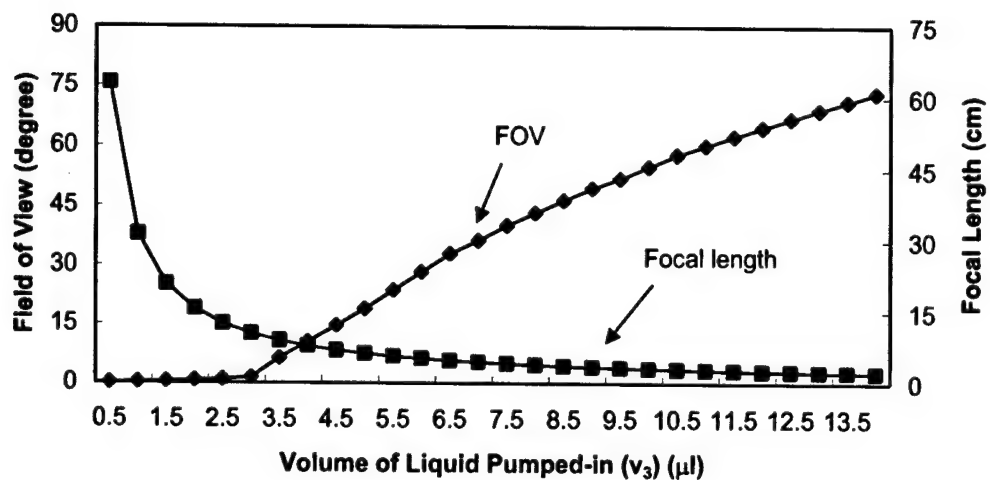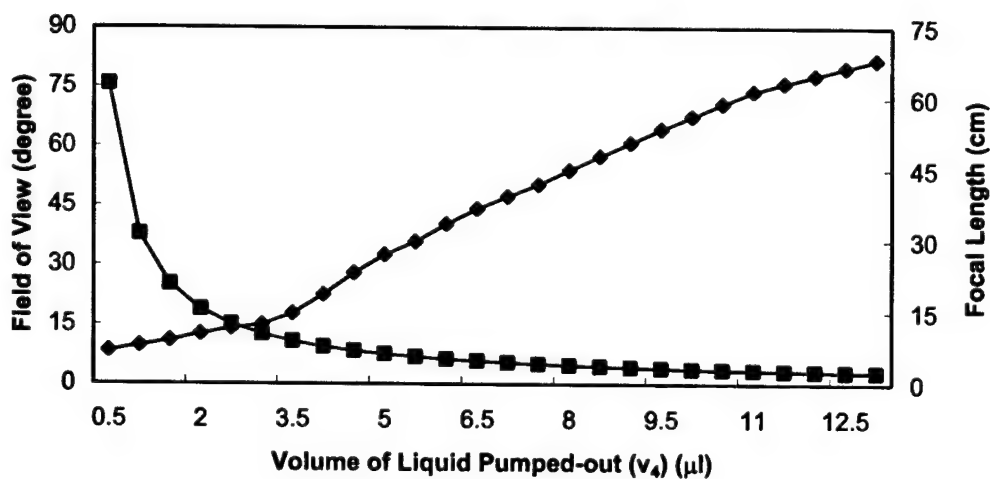
Figure 29: Images taken at different volume of fluid by activating the lens as
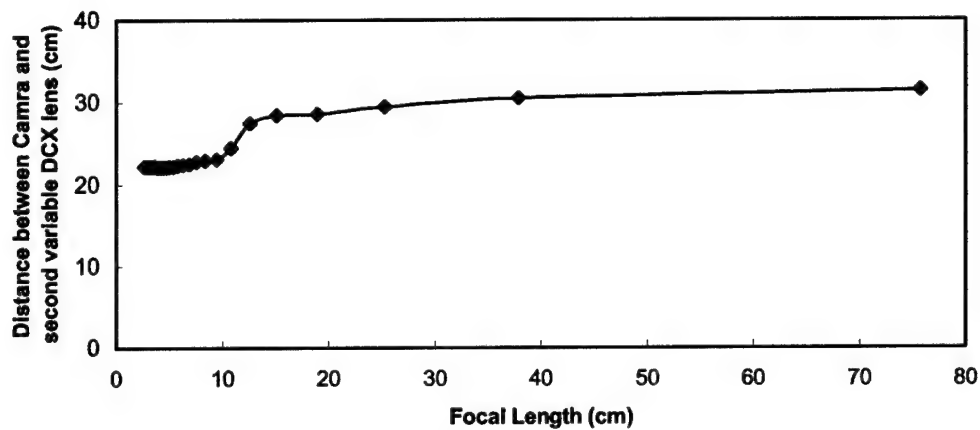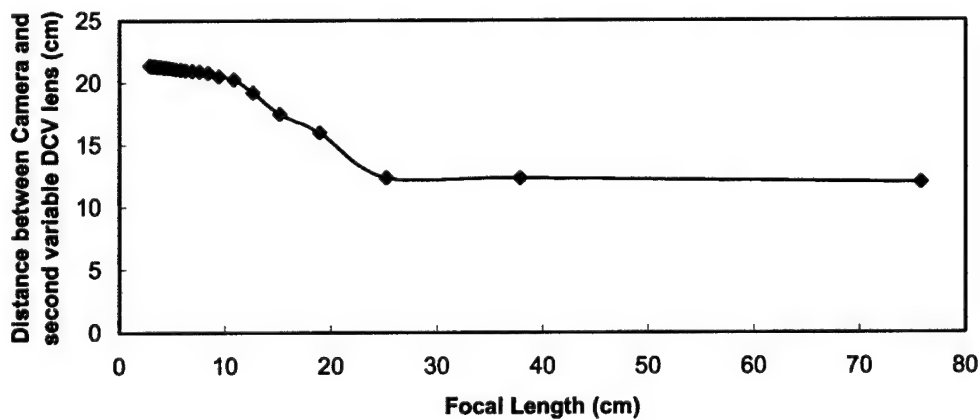(a) DCX lens; (b) DCV lens

Figure 30: Variation in the focal length and the field of view achieved as a function of the volume of liquid (a) Pumped-in (DCX lens); (b) Pumped-out (DCV lens).

(a)

(b)

Figure 31: Focal Length vs. Distance between the camera and the dynamic lens.
(a) DCX lens; (b) DCV lens.

Fabrication of optical lens system with variable focal length capability and wide angle of view at micro scale is been carried out by integrating two or three variable focal length DCV lenses that is by further reducing the focal length of DCV lens system.

PART II : Variable Focal Length Micro Lens with Electrical and Fluidic Actuation

Among the most recent methods to fabricate variable refractive index lenses, Liquid Crystal (LC) lenses have become very popular. Various aspects of this material have been probed for its use as variable refractive index material. Lenses have been prepared using this material to form concave as well as convex structures by simply varying the operating voltage.

The lens structure that is discussed here combines two methods of activation, fluidic as well as electrical. Through the initial work done on the glass lenses it was concluded that a DCX lens with higher focal length followed by a series of DCV lens with lower focal length (tested up to 3 lenses) gives a wide FOV. Thus the lens fabricated here has a DCX lens with fluidic activation followed by a DCV lens with LC activation. The number of DCV lenses can be increased according to the requirement. The schematic of the lens is shown in Figure 32.
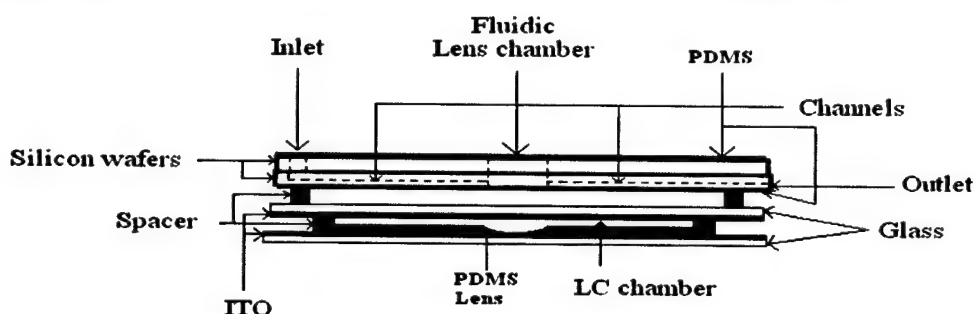
Figure 32: Structural layout of the lens based on the combination of fluidic cell and LC cell.

The primary purpose of this lens is to provide a wide FOV with a variable focal length. The first layer of this lens was of PDMS which is cast on the diced Si wafer which consist of two through holes, one for the inlet and one for the lens opening. The PDMS forms a flexible structure on top of the through hole for lens. After the first wafer chip lies the second chip which is glued to it using either photoresist, PDMS or epoxy. This part consists of a through hole in the center for the second one half lens and two channels for the fluidic flow. The inlet side channel, on the bottom wafer, starts from under the inlet of the lens on the top structure and runs across the lens. The outlet side lens runs from the lens right up to the end of the chip. This opening at the outlet is kept for the removal of the air in the compartment which is there prior to the fluid being pumped in. This opening is sealed using an epoxy, after the requisite amount of fluid is filled in to occupy the lens chamber, so that no fluid flows out of the unit causing a reduced pressure in the lens chamber. The secondary lens is integrated to the fluidic lens. A plastic or kapton spacer is used to separate the fluidic lens from the LC lens. On the other side of the spacer an ITO coated glass plate is glued, which forms one of the electrode of the LC lens. For the formation of the LC cell and to separate the two electrodes with an insulating material a spacer is formed on the PDMS layer by using either photoresist (SU8), Kapton, commercially available plastic spacers or epoxy itself. The spacer thickness is approximately 20 μm to 100μm up to 300μm, depending upon the diameter of the lens. The final layer is also of a glass plate with ITO coated on top of it for forming the second electrode for the LC lens. The resistance of the ITO film on

the glass plate is 10Ω. The LC is then filled in the cell using either a syringe, capillary force mechanism or directly dropping it using syringe.

The construction of the LC lens is relatively easy. This lens is formed as an integral part of the fluidic lens. The structure of the LC lens was described earlier. In order to separate the two electrodes and to form the LC compartment a spacer is to be formed. The thickness of the spacer is very critical for the optimum performance of the lens. The ratio between the cell thickness and the lens diameter should not exceed 1:3. Thus a circular spacer of 5 mm diameter or a square spacer of 5mm, and 300μm in thickness was cut out of kapton tape and glued using an epoxy that can be cured in 5min. The second electrode of the LC lens is also formed by indium tin oxide (ITO). This ITO layer is sputtered on a transparent glass plate and has a resistance of 10Ω. The ITO, facing the inside of the LC lens forms the transparent bottom electrode. A concave lens structure is formed in the LC chamber, with the concave side facing the fluidic lens, so as to give a variable focal length concave lens. When the LC are filled in the chamber they do not have any particular orientation and every crystal is aligned in some random direction. In order that all the LC properly align in the direction of the field it is necessary they have one particular direction of alignment prior to the application of the electric field, preferably perpendicular to it. In order to achieve this, before the spacer is bonded to the top electrode a thin layer of PVA is formed on top of both the electrodes and is rubbed by a cotton swab. PVA is soluble in cold water and so 3 (wt%) of PVA is added to the water and is mixed in ultrasonic bath for 15 min. The rubbing with cotton swab is so done that when the two electrodes are joint together; the direction of rubbing is opposite to one another. This gives an initial orientation to the LC in the rubbing direction which is perpendicular to the direction of applied electric field. The individual electrodes are then heated at 160°C for 30 min and then glued together. In order to fill the LC in the chamber the spacer is cut from one side just enough to accommodate a syringe needle. The LC are then filled in the chamber using a syringe or directly dropping it on the lens before sealing it. The opening in the spacer is closed by using the epoxy. Voltage is then applied between these two electrodes which brings about the reorientation of the liquid crystals along the direction of the field and hence changes the optical path length of the light, which is translated as a change in the refractive index.

RESULTS

The experimental setup for pumping fluid in the fluid activated lens is shown in the Figure 33a. The setup consists of a syringe pump on which a 10ml syringe is mounted. The syringe is connected to the lens with fine tubing, which is directly inserted in the inlet of the lens. The first lens that was put to test was a 4mm diameter lens and is shown in the Figure 34b.

Figure 33: (a) Fluidic lens connected to the syringe mounted on the syringe pump.
(b) Fluidic lens fabricated on silicon wafer having a diameter of 4mm.

The chamber volume for this 4mm lens was calculated to be 12.56µl. This is the volume of the fluid required to fill the chamber such that the two films are exactly parallel to the each other, with no deflection at all. The lens was mounted on the optical rail and the object, a board with "LOUISIANA TECH UNIVERSITY" written on it, was viewed through it using a Si-Camera and frame grabber system. The fluid was gradually filled in using a syringe pump at an interval of 2µl. The series of images taken are shown in the Figure 35.

| 0µl | 2µl | 4µl | 6µl | 8µl |

| 10µl | 12µl | 14µl | 16µl | 18µl |

| 20µl | 30µl |
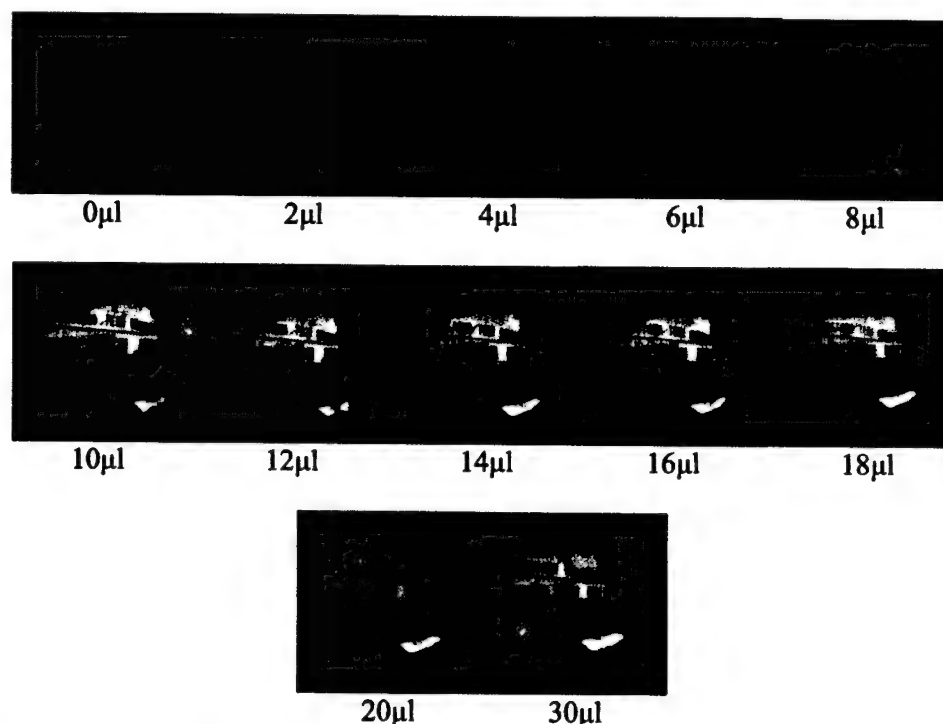
Figure 35: Images taken using a 4mm diameter fluidic lens for the corresponding values shown.

The field of view was calculated using the formula stated above and is tabulated below in Table 4.

Table 4: Reading of the calculated F.O.V for the corresponding values of the amount of fluid pumped in the lens for a 4mm diameter lens.

Number	Volume (µl)	F.O.V
1	0	6.92
2	2	8.53
3	4	10.52
4	6	12.5
5	8	14.8
6	10	17.45
7	12	19.65
8	14	21.8
9	16	23.54
10	18	24.22
11	20	24.56
12	30	25.24

These results were plotted on a graph of volume against FOV and is shown in Figure 36.
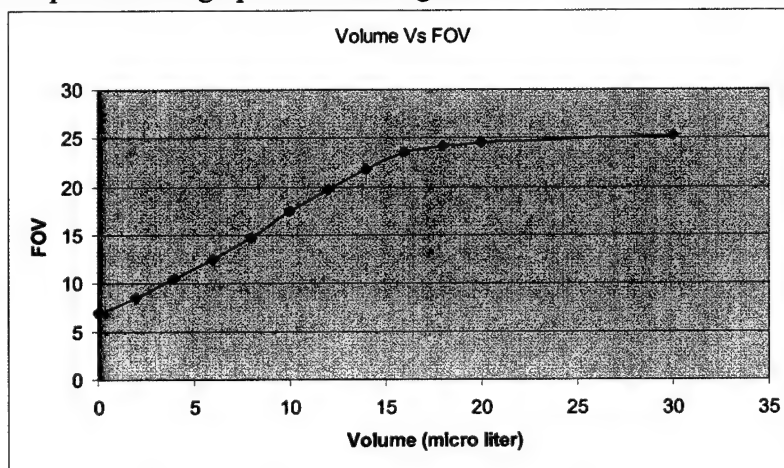
Figure 36: Graph of the Volume of the liquid pumped in the lens against the corresponding FOV.

The graph clearly indicated that the FOV increases almost linearly until 19µl and then saturation occurs. With further increase in the fluid volume in the chamber the FOV does not increase much and will eventually not increase at all. This can be explained by the help of the Figure 37. In the Figure 37(a) the lens has low fluid volume and all the rays focus at the focal point, where the LCD of the camera lies, and thus form the image. When this fluid volume increases up to a certain amount, as shown in the Figure 37(b) the rays of light that enter the lens around the periphery come out of the lens at a greater angle than earlier and fall out of the range of the CCD sensor and hence do not contribute to the image formation.
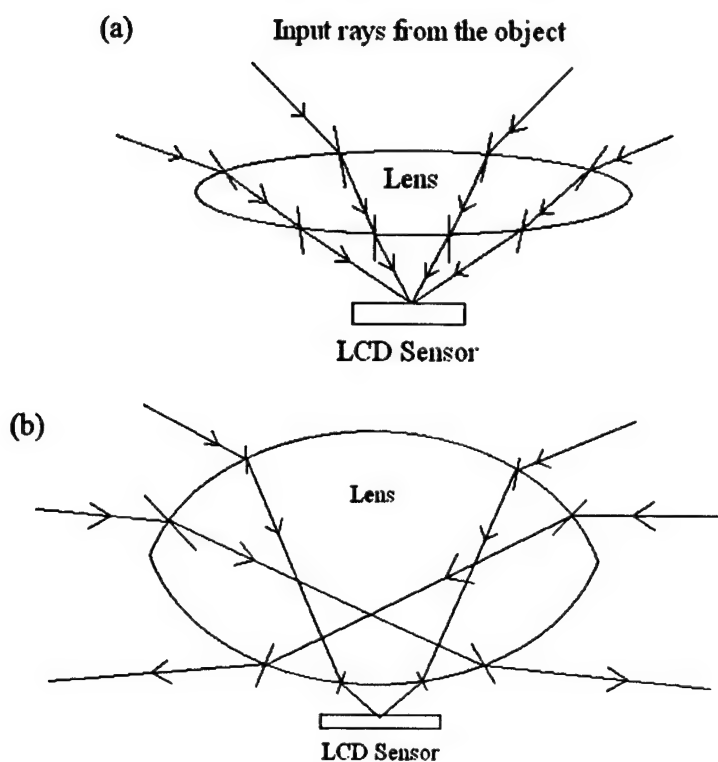
Figure 37: Explanation of the ceasing of the angle of view of the after certain volume of fluid is been pumped in. (a) low volume where the angle of view is still increasing linearly, (b) high volume where the angle of view does not increase linearly with the volume of fluid pumped in.

The next lens that was tested was a 1 mm diameter lens. The chamber volume of this lens was calculated to be 0.785µl. The imaging was not possible using the conventional camera so it was done by keeping the lens under the microscope objective at a distance of 1cm away from the object which was kept under the lens. The fluid pump is then set to stop after pumping in exactly 0.5µl of fluid per minute and then is made to run in the forward direction. This gradually fills the fluid in the chamber, and the images are taken at the same intervals. A series of images that were taken are shown in the Figure 38
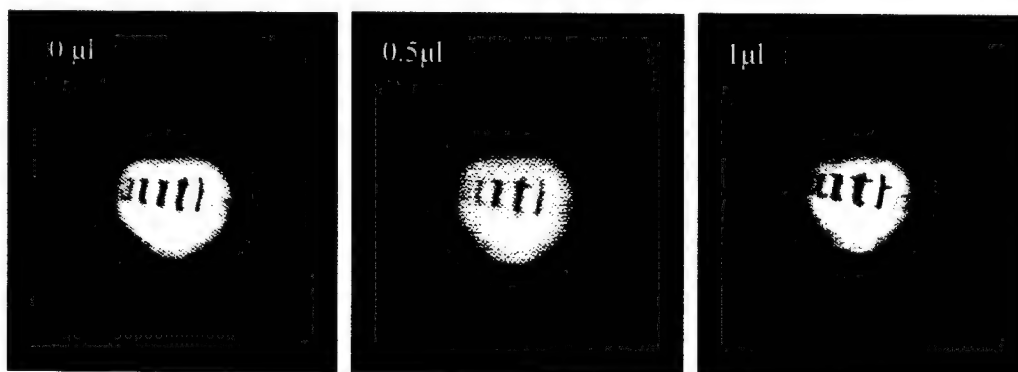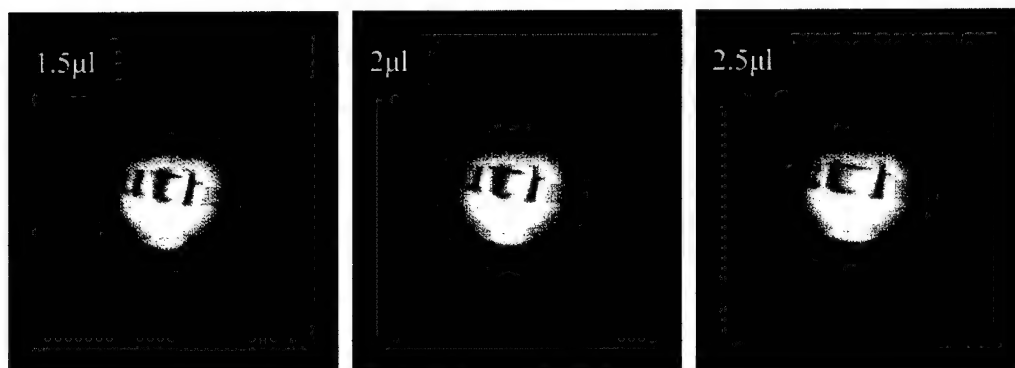
Figure 38: Images taken from a 1 mm DCX lens under a microscope for increasing fluid volume.

The image is of the word "author" which was printed with a font size of 12 (Times New Roman) in Microsoft word. As seen in the Figure 7 the word is almost completely visible at 0μl and as the volume of the fluid is increased the lens's focal length decreases, increasing the magnification and at 2.5μl only "t" and "h" are clearly seen. This is the exact behavior of the DCX lens when its focal length is decreased.

The lens was also tested for contact angle measurement and the figures below (Figure 39) indicate the deflection of the film with the increasing fluid volume. This structure will be combined with the LC cell and the combination will be tested.
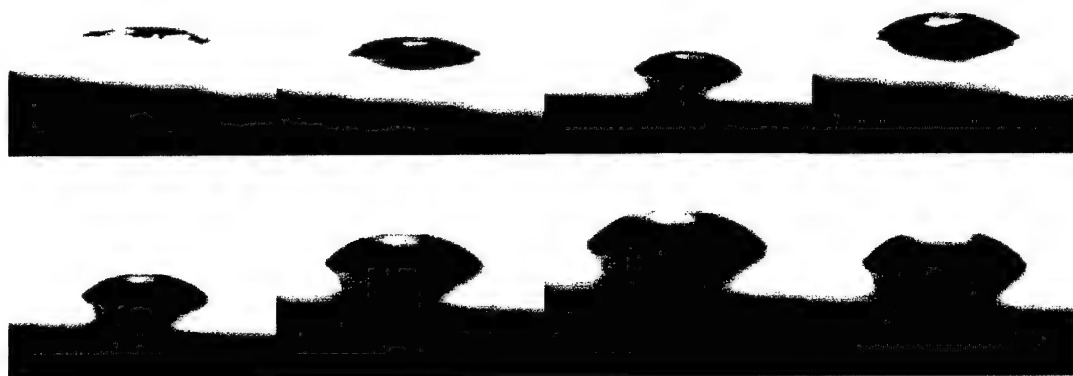
Figure 39: The deflection observed in the 1mm diameter lens when an increasing volume of fluid was filled in the chamber.

Initially the LC lens was fabricated separately for testing the working of the LC. Before the lens could be fabricated, LC cell was made with the pre-alignment layer on it in order to check the behavior of the LC after the application of voltage. Figure 40 shows the image of the working LC cell and Figure 41 shows the experimental setup used to test its performance. The laser source used for the measurement gives the maximum power of 1.5mWatt. The light was allowed to fall on the photo diode, connected to the power meter, through the lens and the meter was showing the output power at all times. Voltage was gradually increased and the corresponding

output power was noted. As the voltage increases the LC are supposed to get aligned in the direction of the field and then the output power should increase. The results obtained in the experiments matched the theory and are shown below.
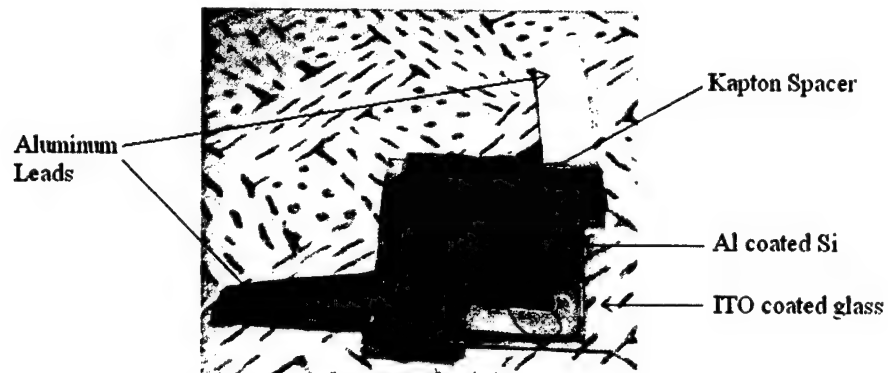

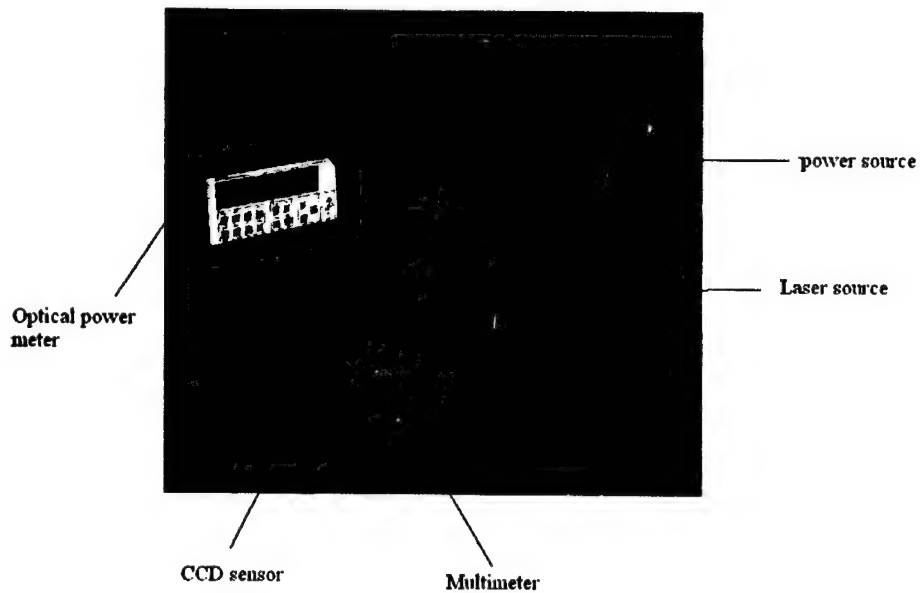**Figure 40**: First working lens using liquid crystals

Figure 41: Experimental setup to test the LC lens performance.

Voltage was given using the AC voltage source shown above at 1.6KHz starting from 0V to 55V and the readings obtained from the test are shown in Table 5.

Table 5: Transmission of light from LC lens at different voltages.

Reading #	Voltage (V)	Power (mW)
1	0	0.903
2	5	0.907
3	10	0.912
4	15	0.918
5	20	0.923
6	25	0.929
7	30	0.933
8	35	0.937
9	40	0.939
10	45	0.942
11	50	0.944
12	55	0.946

The graph below shown in Figure 42 indicates that the optical power increases almost linearly up to 35V. With further increase in the voltage the power increase reduces. After all the liquid crystals are perfectly aligned this graph is expected to saturate, showing no further increase in power. Due to the limitations of the power supply, further probing of the power could not be achieved.
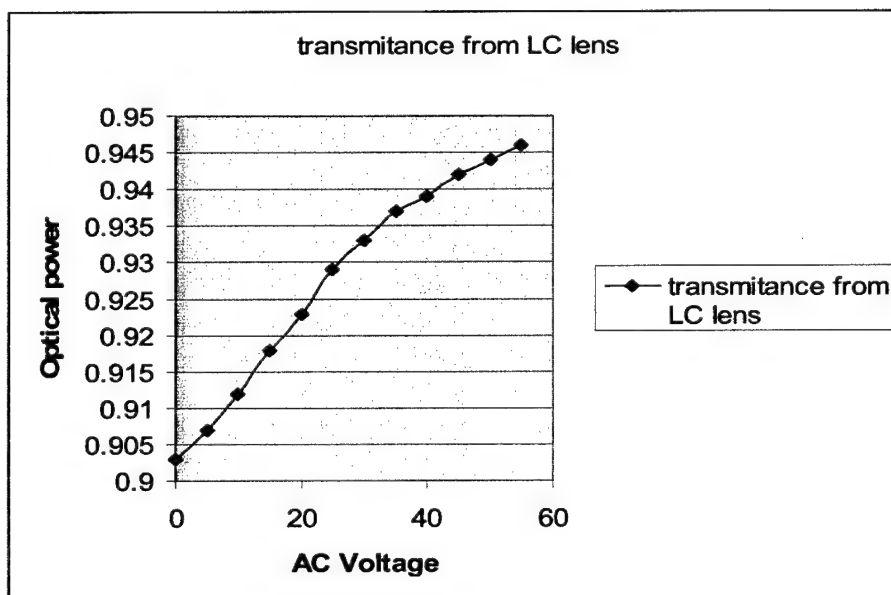
Figure 42: Graph of AC Voltage plotted against Optical power showing the increase in power with voltage.

Figure 43 shows the images taken by gradually increasing the voltage. As it is clear from the images the liquid crystal alignment along the optical axis increases with the increase in voltage.

(a) 0V   (b)5V   (c)10V

(d)15V   (e)20V   (f)25V

(g)30V
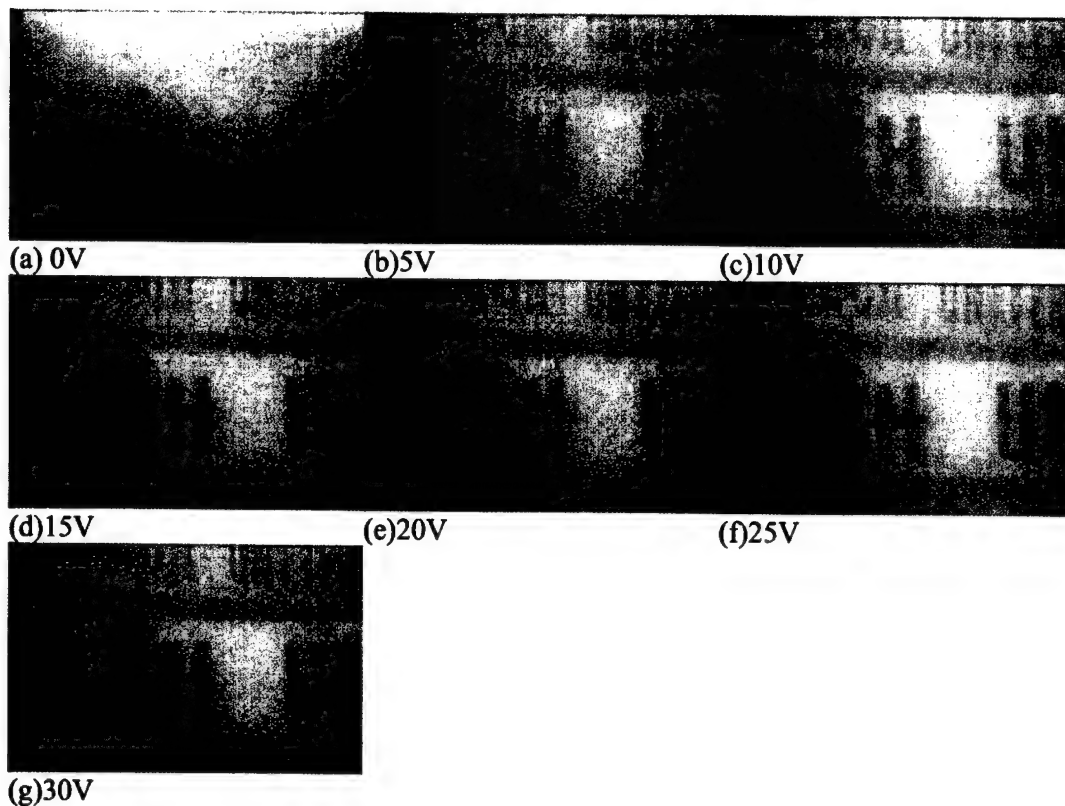
Figure 43: Images taken with a frame grabber system showing the change in the image clarity with increase in the voltage.

This experiment on the LC was done just to check the behavior of the LC with the application of the voltage and no lens effect formation was intended as there was no lens structure in the chamber nor was there any circular pattern on the glass substrates. The next steps involves the fabrication of a concave lens structure on the glass substrate and then building a LC cell on the top of it, which will form a concave lens with a variable refractive index as shown in the Figure 44.
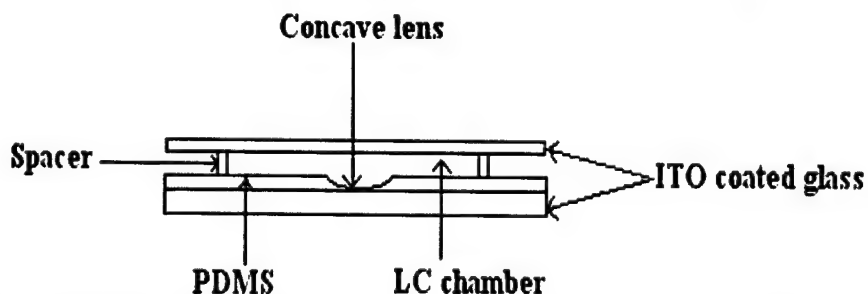
Figure 44: LC chamber with a concave lens structure in it for making a variable refractive index concave lens.

The concave lens was fabricated by making the impression of a convex lens on PDMS as shown in the Figure 45. The convex lens was fabricated by casting a drop of PDMS on a glass substrate. Glass was cleaned properly using acetone and then with water and then dried properly. PDMS was kept for 1hr at room temperature for degassing and minimum curing. The glass plate was then kept on the hot plate at 90°C. The glass plate was then removed from top of the hot plate and kept undisturbed for 15sec. Then, using a syringe needle the PDMS was dropped on the top of the glass plate and was immediately kept on the hot plate again at 90°C. This procedure prevents the PDMS from spreading too fast on the glass plate so that a strong lens is obtained, because at that temperature PDMS cures in appx. 5min. A thin layer of PDMS can first be spin coated on the glass plate and then the plate can be kept on the hot plate so that a smoother surface can be obtained for casting the lens. The final convex lens structure looks as in Figure 46(a). The glass plate was then kept in the desiccator and a few drops of trichlorosilane were added in a separate plate and the vacuum was created in the chamber. The sample was kept there for 1hr. 200μm thick kapton spacer was made and was put on an ITO coated glass plate as shown in the Figure 46(b). This enclosure was then filled with PDMS and PDMS is left untouched for 1hr at room temperature for partial curing. The male mold is then put on top of this enclosure with partially cured PDMS and the combination was cured for another 3hrs at 40°C and at 90°C for 15min. The final concave structure, after carefully pulling out the male mold, looks as in Figure 46(b). Using a syringe, a drop of LC is then put in the concave lens and another ITO coated glass plate is stuck on it using a 5min eopxy. This forms a variable focal length concave LC lens as shown in the Figure 47. The spacer width is approximately 10-20μm.
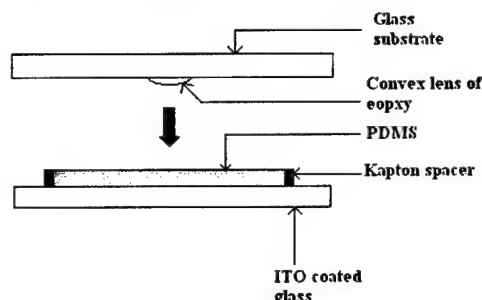

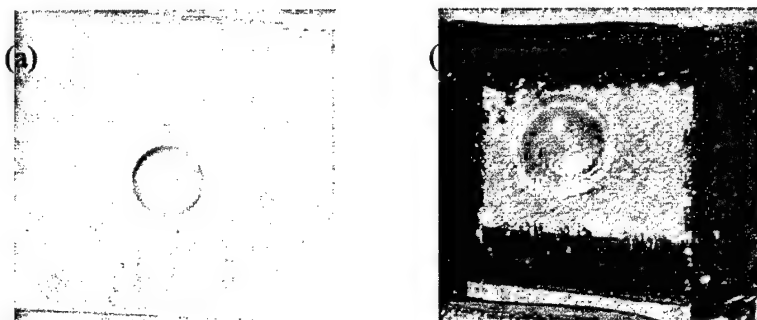**Figure 45**: Method used to fabricate the concave lens structure in a PDMS well using a convex mold.

Figure 46: (a) Male mold for making the concave lens; (b) Final concave structure after removing the male mould.
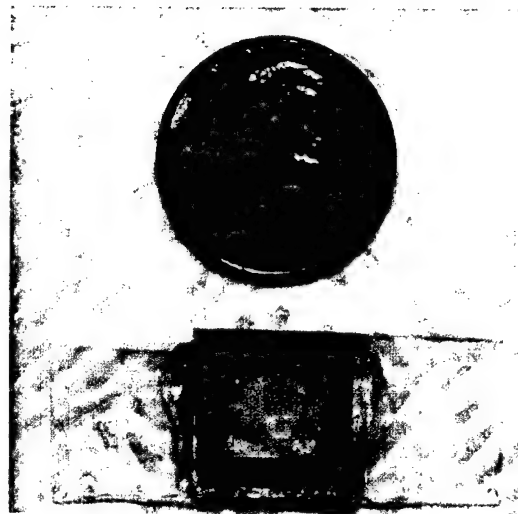
Figure 47: A variable focal length concave lens using LC. The diameter of the lens is
3mm and the spacer thickness between two electrodes is 20-25μm.

This lens was again fixed on the optical table with the frame grabber system for testing. A series
of images were taken along with the application of voltage. The power supply was kept at 1KHz
and the voltage was varied from 0V to 50V in the step of 10V and the images were taken
consecutively. Major difference was clearly seen between image taken at 0V and 50V as shown
in Figure 48.
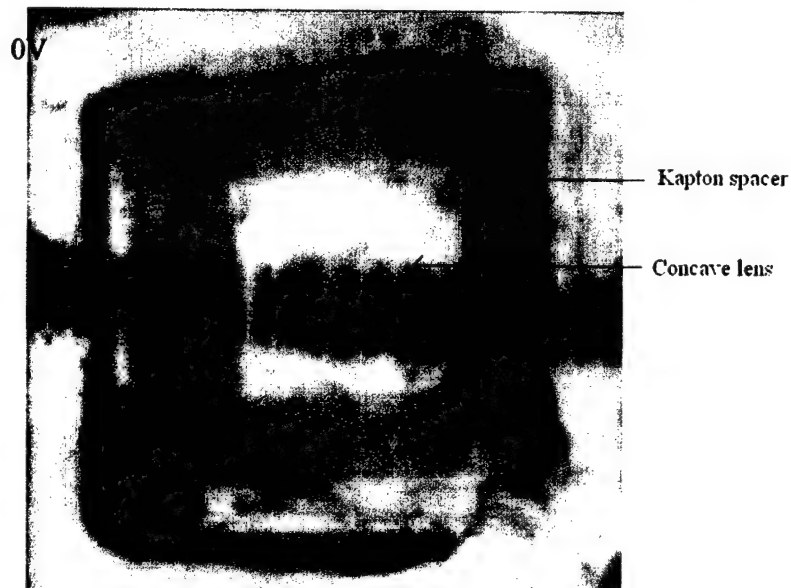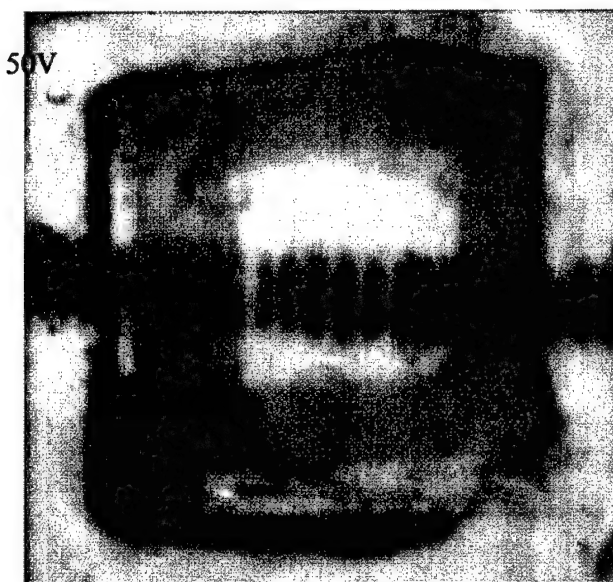
Figure 48: Change in the focal length of the concave lens by applying voltage.

As seen in the figure, when no voltage is applied, approximately three lines are seen inside the circular lens area. With the further application of the voltage the orientation of the LC directors moves along the line of electric field i.e. along the optical axis of the lens. Between the two electrodes, PDMS acts as an insulator. With the lens structure on PDMS the resistance to the field provided by the concave lens shaped PDMS gradually increases radially as we move away from the center because of the potential divider that is formed and the capacitance of the LC layer, thus reducing the field intensity along that line. This leads to a differential alignment of the LC directors along the lens surface and thus forming a lens shape. The optical path of light throughout the lens surface follows the differential curve, even after application of voltage, due to the differential insulation level provided by the PDMS. As the voltage increases the directors align more towards the field and the degree of alignment depends on the intensity of the field at each point in the lens. Due to this alignment the optical path of the light inside the lens reduces making it a strong lens. It is clearly seen in the Figure 48 that 5 lines of the object are visible in the image at 50V and the angle of view has increased. The imaging distance was 4mm and the lines were 1mm each with 1mm gap in between. Calculating the angle of view using the formula stated earlier was 41.1° at 0V and 48.36° at 50V.

Part III : Variable Focal Length Lens System by Integrating Electrowetting and Liquid Crystal Cell

An effort was made to fabricate a focal length variable microlens system using electrowetting method. Electrowetting is a phenomenon which can alter spreading of a liquid droplet by giving voltage to the later. This phenomenon essentially alters the surface tension of the liquid droplet on a dielectric layer when a capacitive force is induced between the droplet and a conductor by applying an electric voltage. This project focuses on the use of this particular phenomenon for fabricating a microlens with variable focal length. This can be achieved by the simple fact that

the applied voltage between the droplet and the conducting surface can be used to change the focus of the droplet. The microlens fabricated using this method is revisable i.e. it can be used for focusing and defocusing. Figure 49 illustrates the method of simple electrowetting and how it can be used as a lens.
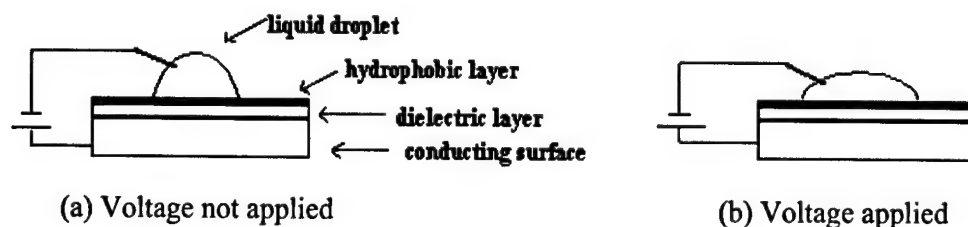

(a) Voltage not applied   (b) Voltage applied

Figure 49: Demonstration of the electrowetting method.

Figure 49 shows a simple electrowetting process in which a capacitive force is induced between the droplet and the conducting surface by applying voltage thereby causing the liquid droplet to spread. The dielectric layer between the liquid droplet and the conducting surface induces the desired capacitive force. This capacitive force changes the wettability of the droplet and makes it spread on the substrate. This simple setup can be used as a liquid droplet lens if a transparent conductive substrate and a transparent dielectric layer is used. This setup can be used to focus and defocus the light ray passing through the droplet i.e. variable focal length. The only disadvantage of the above setup is that the invasive electrode in the droplet causes severe optical distortion in the image focused. This can be rectified if a different electrode pattern is used. An electrode pattern is designed so that the invasive electrode can be eliminated.

EXPERIMENTAL

Initial experiments were conducted to demonstrate the effect of electrowetting using the invasive electrode method. In this experiment a silicon wafer coated with aluminum by sputtering method has been used as the substrate in which the aluminum layer acts as the conducting surface. A thin polyethylene sheet of 50 μm was used as the dielectric layer and 5 μl water droplet was placed on it. A thin copper electrode was used as the invasive electrode to be immersed in the droplet. A voltage of 40v was applied between the conducting aluminum layer and the droplet. A significant deformation in the droplet shape was not observed when the voltage is applied. This may be due to the very large thickness of the dielectric layer, low voltage applied, very less hydrophobicity of the dielectric layer. Figure 50 shows the setup of the initial experiment in which the conducting layer is the sputtered aluminum layer and the dielectric layer is the polyethylene sheet.
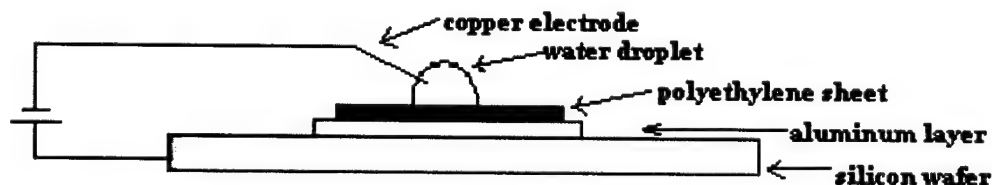

Figure 50: Schematic view of the initial electrowetting experiment.

As discussed above the electrowetting process can be used to fabricate a variable focal length lens by using a specially designed electrode pattern, a transparent conducting material and a transparent dielectric layer. For this experiment an ITO sputtered glass substrate was used which is transparent and conducting. The specially designed electrode pattern is etched on the ITO layer which can used to manipulate the liquid droplet. This special electrode pattern is to eliminate the use invasive electrode which causes severe optical distortion.the transparent dielectric layer which is used in this experiment is polyimide.

FABRICATION STEPS

A mask was designed to pattern the electrodes on the ITO layer coated on the glass substrate. This electrode pattern eliminates the use of invasive electrodes and helps in getting a minimum optically distorted image. This particular design is co-planar and can be directly etched onto the ITO layer. Figure 51 shows the electrode pattern.
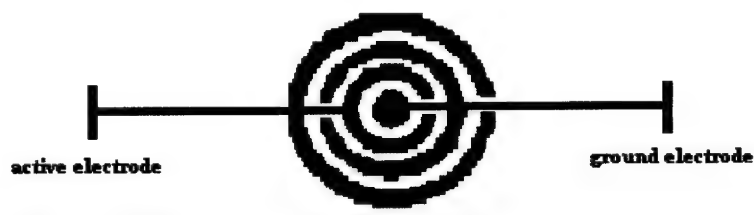
Figure 51: The electrode design for the variable focal length lens.

As can be seen from the Figure 46 both active and ground electrodes lies in the same plane and can be directly etched onto the ITO layer. The liquid droplet will be placed at the centre of the ITO electrode pattern and the voltage is applied between the two electrodes to manipulate it. The electrodes are so designed that it can fit a 2µl droplet and the outer diameter of the active electrode is 2 mm.

A 25 mm X 25 mm, 0.7 mm thick glass substrate sputtered with ITO is used to for the fabrication of the electrode. The resistance of the ITO layer is measured to be 35 Ω. The thickness of the ITO layer is measured by an ellipsometer and it was found to be 115 ηm.
A positive photoresist 1813 was used for the soft lithography. The mask is exposed and the ITO coated glass substrate was developed in the MF 319 developer solution. An aqueous solution of 20% HCL, 5% HNO_3 was used to etch the ITO layer on the glass substrate. A few drops of liquid detergent are mixed in the ITO etchant solution to increase the wettability of the etchant to the ITO layer. The etchant took approximately 45minutes to etch the ITO layer. The etch rate can be increased drastically by heating the etchant to 60 °C. A good etch profile is observed on the substrate after the etching. This profile is observed with an AFM. The Figure 52 shows the etch profile of the ITO layer on the glass substrate.
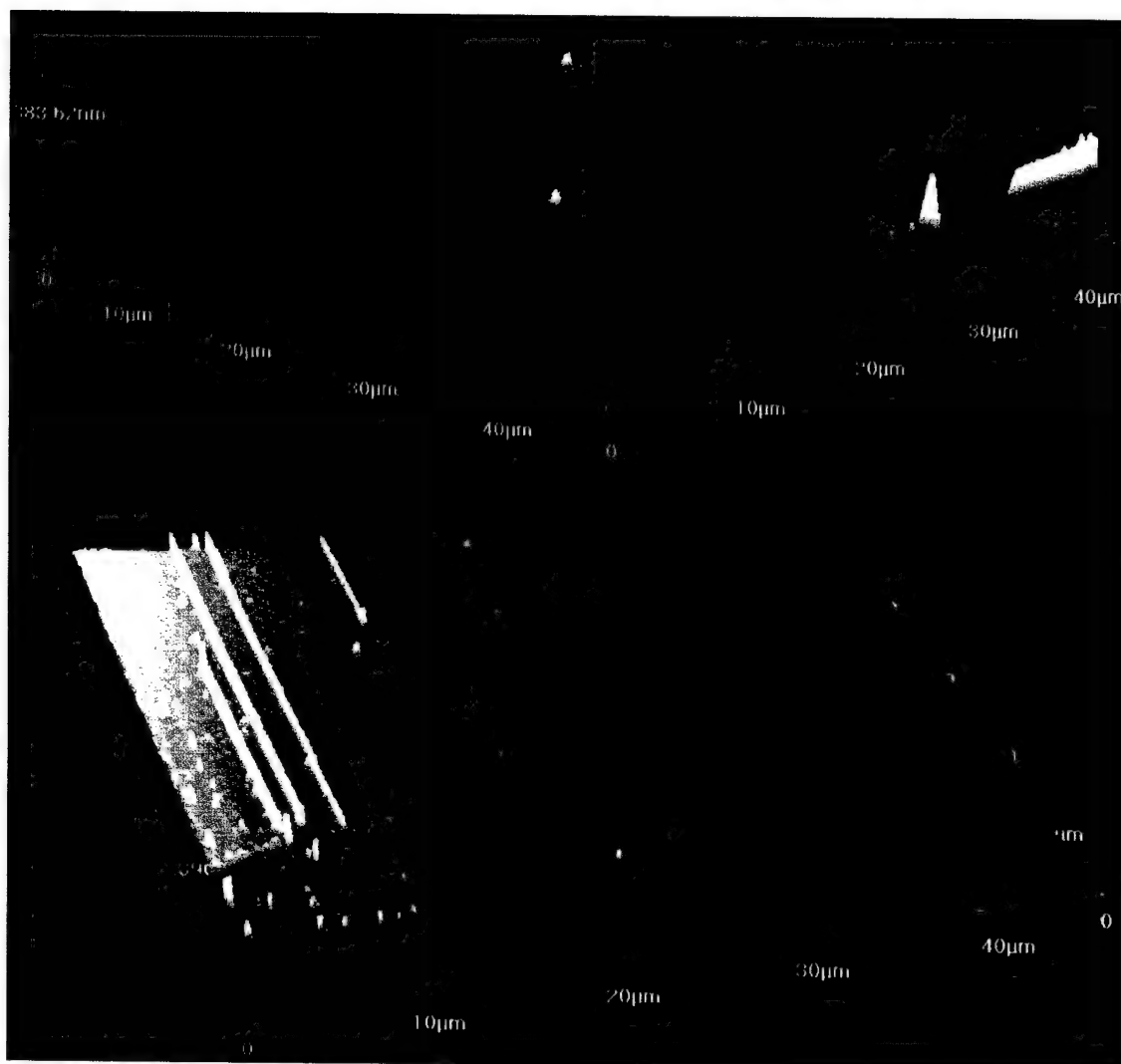
Figure 52: The AFM graphs of the etched ITO layer on the glass substrate.

A clear demarcation between the ITO layer and the glass substrate can be seen in the surface profile shown in Figure 52. An IV measurement was made to observe the conductivity on the etched ITO surface. Figure 53 shows the I-V graph of the ITO electrodes. The resistance on the etched electrodes was measured to be 780 Ω.
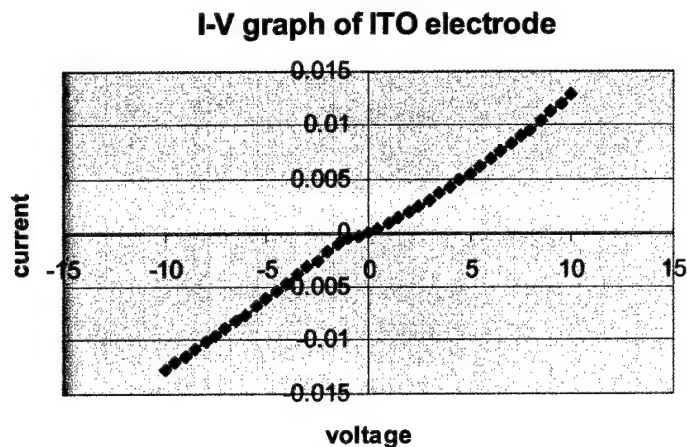
I-V graph of ITO electrode

Figure 53: I-V curve for the etched ITO surface on the glass substrate.

Polyimide was used as the dielectric material that induces the capacitive force between the droplet and the electrodes. A mixture of 1.5g polyimide and 4.5g NMP was prepared to be used as dielectric layer which can be spin coated or dip coated. This mixture was spinned onto the etched ITO electrodes at 3500 rpm for 45 sec to give a thickness of 300µm. The spinned substrate was soft baked for 10min at 90°C and 20min at 125°C. It is subsequently hard baked in a furnace at 350°C for 2 hours in nitrogen environment to get a pinhole free dielectric layer.
Cytop will be used as a hydrophobic layer which gives a large contact angle for the water droplet on the substrate. Cytop can be spin coated to give a very thin layer of hydrophobic layer.

TESTING
After the deposition of the hydrophobic layer a water droplet will be placed at the centre of the electrode pattern. The device will be tested for electrowetting effect by applying the voltage to the two electrodes.

PART IV: Gradient Refractive Index Lens Structures

Different techniques have been reported for the fabrication of gradient refractive index lens structures, such as ion-exchange, chemical vapor deposition (CVD) and molecular stuffing. Most of the radial-GRIN lenses in glass are fabricated by ion-exchange method. Limitations of ion exchange technique include small size of the lenses and time-consuming fabrication. Our research goal has been to develop the GRIN lens with biocompatible polymer, and to have the lens such that it can be easily controlled. Three different approaches have been investigated and tested. The research results describe the possibility of forming GRIN in polymer or dispersed liquid crystal.

Approach 1: Electrophoresis with Nano Particles

This research work has focused on forming the GRIN structure with polymer or hydro gel using electrophoresis to control nanoparticles distribution inside the polymer. Different polymer materials have been tested in electrophoresis running. Miniaturized vertical electrophoresis running setup has been built, and in order to measure the running result, layer-by-layer self-assembly has been used to fluorescently dye sub-10nm nanoparticles when preparing the samples.

Theory and Background

Controlling the loading level of metal-oxide nanoparticles within organic materials or polymers can change the refractive index. The high quality of small size nanoparticles plays an important role in maintaining a low level of light scattering, particularly in the visible to infrared regions. Recently, highly homogeneous nanoparticle-polymer composite materials have been developed to meet the high demands of photonic materials for converting a broad range of the refractive index. However the fabrication processing of the gradient refractive index materials is still a challenge.

Electrophoresis describes the migration of charged particles under the influence of an electric field. Many important biological molecules, such as amino acids, peptides, proteins, nucleotides and nucleic acids, possess ion groups and, therefore, at any given pH, exist in solution as electrically charged species, either as cations (+) or anions (-). Based on this phenomenon, one can charge the nanoparticles such as metal-oxide in solution and then under the influence of an electric field, these charged particles will migrate either to the cathode or to the anode, depending on the nature of their net charge. The distribution of nanoparticles will depend on the particle size, electric field and time.

When a potential difference (voltage) is applied across the electrodes, it generates a potential gradient, E, which is the applied voltage, V, divided by the distance, d, between the electrodes (Fig. 1). When this potential gradient E (electric field) is applied, there is a force that drives a charged particle towards an electrode. However, there is also a frictional resistance that retards the movement of this charged particle. This frictional force is a measure of the hydrodynamic size of the particle, the shape of the particle, the pore size of the medium in which electrophoresis is taking place and the viscosity of the buffer solution. The velocity, v, of a charged particle in an electric field is therefore given by the equation:
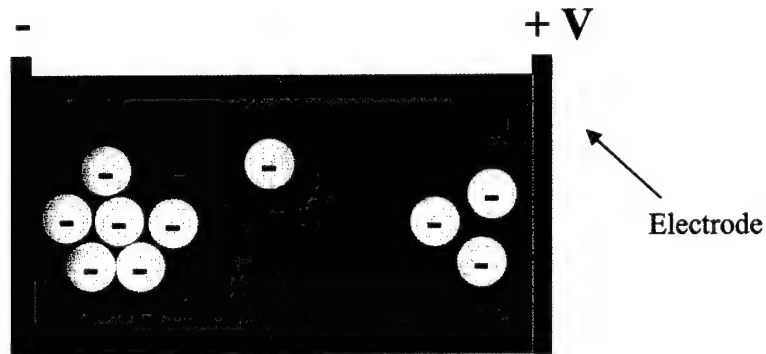
$$v = qE / f$$
where f is the frictional coefficient.


Fig.1 Electrophoresis Running

Normally, a more common term, electrophoretic mobility (u), is used, which is the ratio of velocity of the particle to field strength (v/E). When a potential difference is applied, particles with different overall charges will begin to separate, due to their different electrophoretic mobilities.
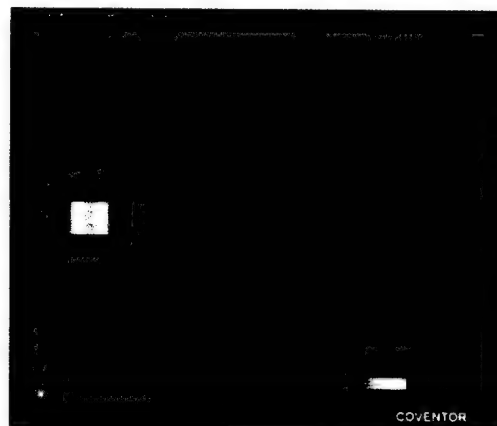
Simulation

Before conducting experiments on electrophoresis, electrophoresis simulations have been done. Figure 2 shows simulation results of species with different mobilities under the same running voltage and time.
Particularly, Fig. 2 shows the running result in 300 μm long channel based on different mobilities from 500 to 50 cm^2/Vs under the same driving voltage (250V) and period of time (1 sec). The running distances are different from each other and species with highest mobility have the longest moving distance. And for each running, after certain time duration, the species running will form a band instead of a line at the beginning.

All of these simulation results indicate that it is possible to use electrophoresis to form parabolic concentration distribution of different particles.
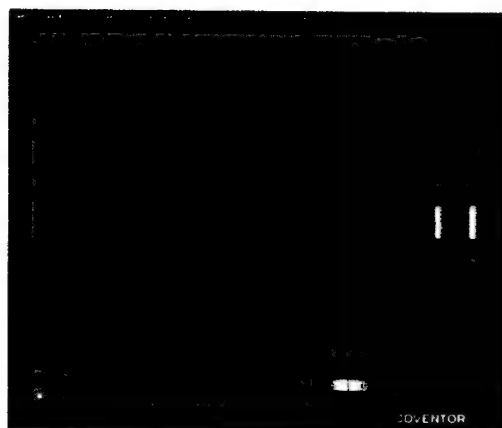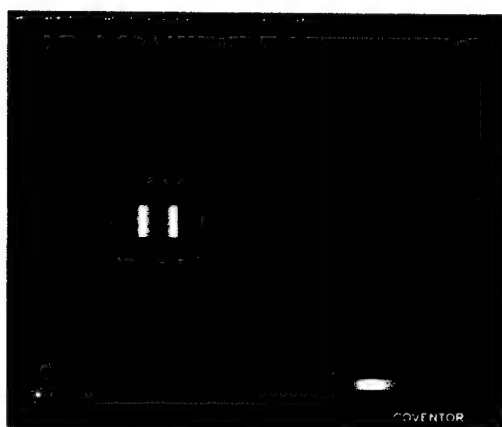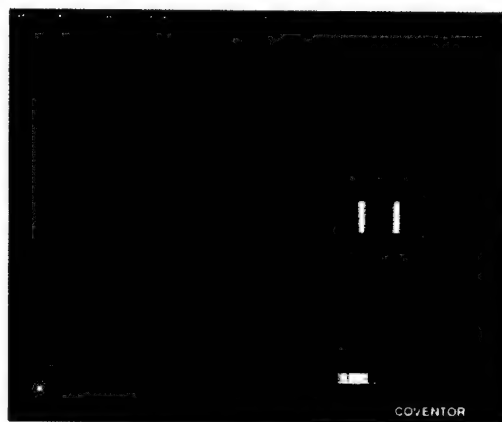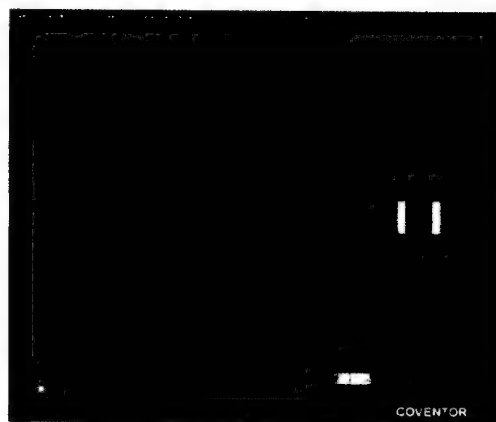
Fig. 2 Simulation Results: a) before running; b) mobility=500; c) mobility=400;
d) mobility=200; e) mobility=100; f) mobility=50 cm^2/Vs

Material Synthesis

Two hydrogels were selected as the testing candidates. These are poly(2-hydroxyethyl methacrylate) (pHEMA) and polyAcrylamide (PAA). PHEMA is a typical optical material used for the making of contact lens, and it shows good tensile and tear strength properties. PAA is used as electrophoresis medium in biological species separation. It has good transparency and could be a potential optical material in the optics industry.

The synthesis recipe of pHEMA is as following:

- HEMA is the monomer; ethylene glycol dimethacrylate (EGDMA) is the initiator; DEAP or Darocur-1173 or BME is the crosslinker.
- Mixture of HEMA/water/EGDMA/DEAP at a weight ratio of 60/40/0.34/0.51
- Use a UV lamp which gives emission between 310-400 nm, with peak at 350 nm and intensity is 4000 microwatts per centimeter square.
- Place the mixture in glass plate and cure it under UV light for 30 minutes at ambient temperature

Different monomer/water percentage ratios were tried to test the mechanical property. The following results have been obtained:
1) When monomer is below 50%, the polymer will become white in color, which is not acceptable for optical application;
2) Higher water content has worst mechanical property;
3) After losing all the water content, pHEMA will shrink and become very hard.

Concentration	10%	20%	30%	40%	50%	60%	70%	80%	90%
Transparency (Y-Yes, N-No)	N	N	N	N	N	Y	Y	Y	Y
Tensile strength (G-Good, B-Bad)	B	B	B	B	G	G	G	G	G

PolyAcrylamide is used as separation gel for DNA and proteins in electrophoresis, and shows good separation results. But it does not have very ideal mechanical properties when water content is high. It can be synthesized based on the following recipe:
- Acrylamide/bisacrylamide are monomer and initiator; Ammonium persulfate (APS) is crosslinker; TEMED (N,N,N',N'-tetramethylene-ethylenediamine) is catalyst.
- Prepare mixture of acrylamide/bisacrylamide/APS/water
- Drop 0.5% TEMED
- Wait 15 minutes for polymerization

Normally in biological separation, the polyacrylamide gel is 5% to 40% based on the different sizes of molecules. It is made to 800 μm thin film, with 5% acrylamide concentration. After polymerization, the thin film is sticky on its surface. Mechanical properties are measured under different pH values using 3D stage to obtain thin film deflections versus forces. From the experimental results of force vs. displacement, the polyacrylamide thin film shows to be much more rigid when the pH value is 7 than when pH value is 10.58. The maximum force is very low

before rupturing the film. But its elasticity is very good. Its deformation could reach 6 mm when only applying 5g forces. Fig. 3 illustrates the measurement setup and Fig. 4 shows the measurement results.
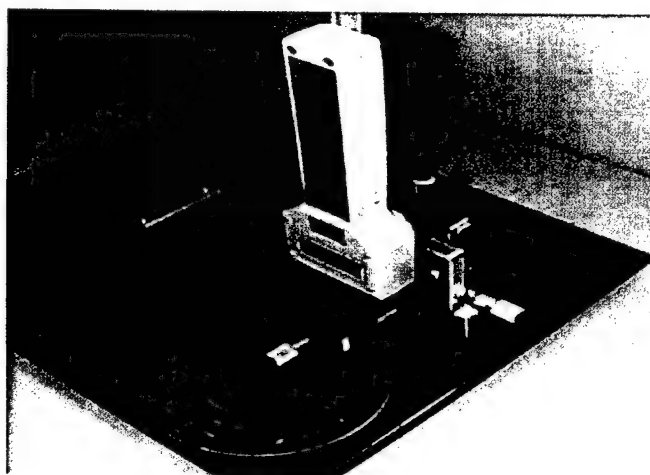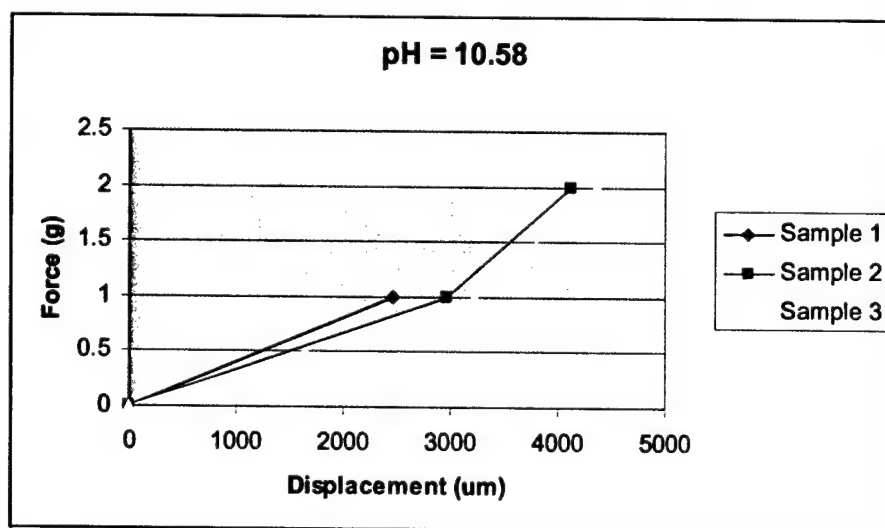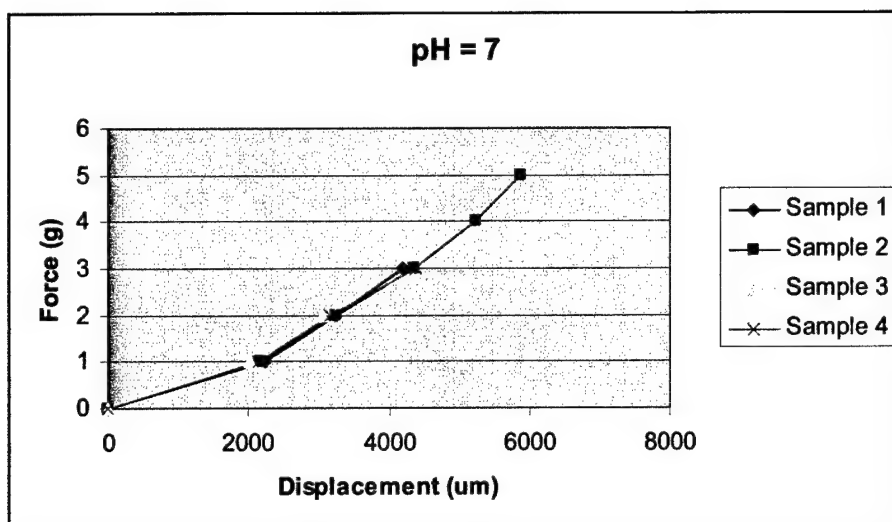

Fig. 3 Deformation Testing Setup

Fig. 5 Deflection with Applied Force

Acrylamide can also be polymerized, if using photosensitive crosslinker. The polymer is not transparent after UV exposure. After losing water content, it could shrink to half of original size. But the thin film still has certain tensile strength.

Experiments & Results

1. Diffusion Test

Before the electrophoresis running, free diffusion tests using 300 nm nanoparticle dispersion were done in pHEMA and polyacrylamide. After one week, No blue colored nanoparticles have been automatically diffused inside of polymer (Fig. 6). Thus, the electrophoresis is necessary to distribute the charged nanoparticals into the polymer.

Fig. 6 Free Diffusion Test

2. Nanoparticle Coating

In order to observe the nanoparticle distribution in polymer after electrophoresis running, the nanoparticle dyeing has been done during sample preparation. Normally there are two methods to dye nanoparticles. These are fluorescent dye and absorbing dye. Since spectrum microscope can only analyze particles inside solution, fluorescent dye is used in the experiment, as it is easy to check under fluorescent microscope.

Two kinds of nanoparticle powders (zirconium oxide and silicon oxide) have been available in the lab. Due to Rayleigh-scattering in case of refractive index mismatch between the particles and the polymer matrix, scattering losses could be reduced using nanoparticles with particle diameters < 10 nm. In the following experiments, 7~9 nm silica has been used as electrophoresis running sample. First, it is dyed by fluorescent label, as showed in Fig. 7.

In water solution, silica particles have negative charge in zeta potential measurement. Since Poly allylamine Hydrochloride (PAH) is positively charged polymer, based on the theory of layer-by-layer self-assembly, it will be the first mono layer (since silica particles are negatively charged). The fluorescent TRITC labeled PSS, which has negative charge, is fluorescent dye as second layer of one bilayer (Fig. 7).

Nanoparticles (SiO$_2$)

PAH (+)   **PSS-TRITC addition (-)**
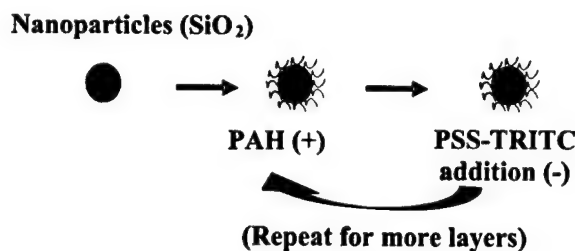
(Repeat for more layers)

Fig. 7   Silica Coloring

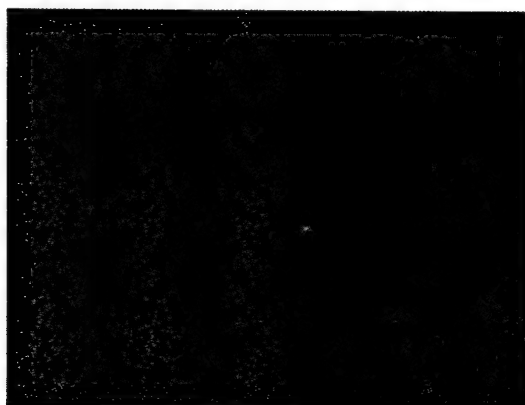Four bilayers have been coated on silica nanoparticles for electrophoresis.

Fig. 8 Fluorescent Dyed Nanoparticles in Gel

When dyed silica is mixed uniformly in a gel thin film, the red fluorescent silica can be seen under the fluorescent microscope (Fig. 8).

3. Electrophoresis Running

In order to get the best running results, a miniaturized electrophoresis running setup has been designed and fabricated.

1) Experiment Setup

The height of the miniaturized running setup is 3.5 cm and the width is 4 cm, while the standard vertical electrophoresis equipment (Fig. 9) is 10 cm by 11 cm.
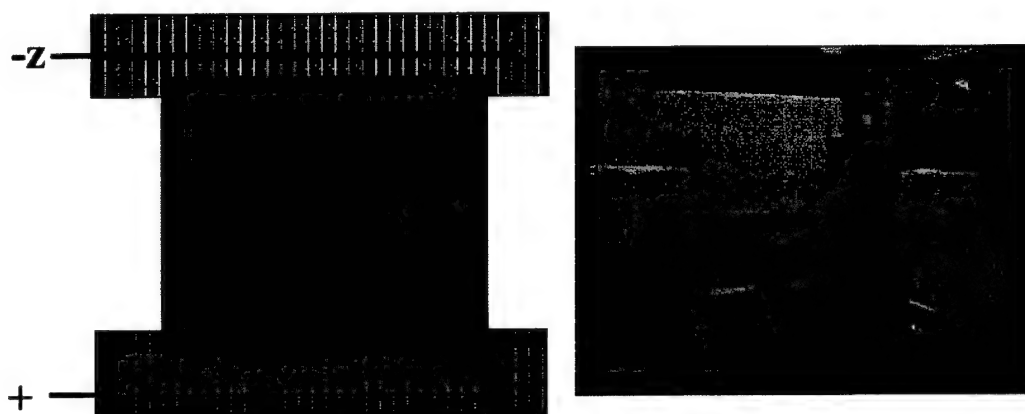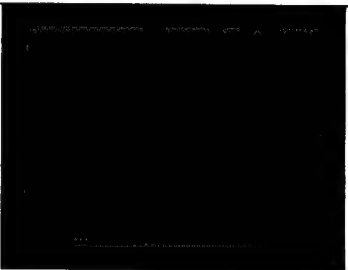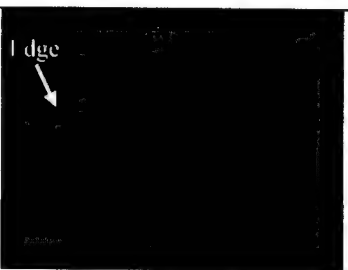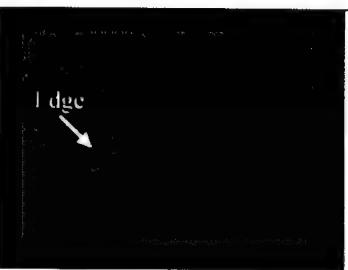

Fig. 9 Vertical Electrophoresis Running Scheme and a Standard Running Tool

2) Electrophoresis Running

Several Electrophoresis runnings have been done using different driving DC voltages. Pictures, as shown below, have been taken to show the movement of silica nanoparticles. In these experiments, the driving voltages are kept constant and the gel concentration is 5%. All the results indicate the possibility of controlling the nanoparticle distribution in gel using electrophoresis. The results also have provided the experimental prove to make this distribution to occur inside circular shaped gel to form GRIN structures.

Voltage	Current	Time	Picture	Observation
250 V	—	4 min		1. Obvious red color at the well edge; 2. At around 1 mm position, a red particle line was found; 3. At 2 mm position, some red particles were found; 4. At 4 mm, almost nothing.
250 V	—	8 min		1. Red band was found at a little farther position than the 4-min running position; 2. Very clear edge formation
500 V	—	45 min	Edge	1. At 2 mm and 2.5 mm, particles were found; 2. Obvious band can be found close to the edge of film (0.7 mm).
500 V → 800V	—	45 min	Edge	Note: gel recipe was changed a little with more buffer inside 1. No obvious band in long distance position; 2. Particles concentration could be found to gradually drop in the gel at the edge of thin film.

Approach 2: Droplet Size Control in Dispersed Liquid Crystal

The goal of this research is to develop a new approach to fabricate the gradient refractive index lens with dispersed liquid crystal (LC), which provides a quick and simple way to control the gradient refractive index with electrodes.

Theory and Background

A variation of the overall focal length of an optical system is required if the object being imaged is not in a fixed position. Previously this variation was done by a mechanically driven shift of the separation between combinations of lenses. The technology of liquid crystals with their electrically controllable birefringence may provide an alternative. A cell is constructed using electrodes patterned with holes on both substrates and then the fringing fields between the electrodes cause the liquid crystal molecules to orientate themselves into what is, optically, a lens structure.

Liquid crystal cells with axially distributed tilt angles may be constructed using a pair of circular hole-patterned electrode substrates. With this approach, very small LC lens with variable focal length can be fabricated. Optimizing the electrode structure, device parameters and LC material parameters, good lens properties may be achieved. The properties of the LC microlens may also be improved by using the polymer stabilization technique.

As the Polymer Dispersed Liquid Crystal (PDLC) seems to be more promising for varying the focal length and the refractive index of the cell, in this work PDLC has been used. PDLC is liquid crystal dispersed in the monomer matrix. The dispersion is obtained through photopolymerization. The mixture of LC and monomer are mixed in certain proportions and then they are exposed under UV light. In this manner, the liquid crystal molecules will be polymerized and dispersed in the monomer matrix. The size of the droplet depends on the intensity of the UV radiation. As the droplet size is the major deciding factor for the change in the refractive index of the lens, selection of the droplet size is highly important.

Electrode Design, Simulation and Fabrication

The hole of patterned electrodes is selected, because the variation of the electric field across the hole aids in building a lens with graded index of circular pattern. When a voltage is applied across the electrodes, the electric field is minimum at the center of the hole and maximum at the edge of hole. In this manner, the radial distribution properties of the refractive index can be obtained in the hole-patterned area. The director of LC is uniformly parallel to the substrate when a voltage is removed. When no voltage is applied, the director is uniformly oriented parallel to the substrate surface, and the refractive index is n_e for the extraordinary ray. The director near the edge of hole pattern is forced to align along the direction of the electric field when voltage above the threshold is applied across the LC cell. The director near the center of the hole-pattern, however, remains parallel to the substrate; the refractive index near the edge is smaller than the value of n_e, does not change near the center and itself becomes n_e. The refractive index gradually changes from the minimum value at the edge to the maximum value at the center. The LC cell prepared using the substrates with hole-patterned electrodes are therefore expected to behave like a graded index converging lens. When the applied voltage increases, the gradient of the refractive index becomes less steep and the focal length becomes longer and the cell changes to a diverging lens.

In this work, simulations has been carried out using ANSYS to find the electric field distribution across the cell, and the electric field intensity across the hole. In this simulation work the cell

spacing is such that the ratio of the diameter of the hole to the thickness of the cell is 3. One can observe form the vector plot in Fig. 11 for the top view of the hole patterned electrode that according to theory the electric filed at the center of the hole is minimum and at the edge it is maximum. This is for the case when 50 V has been applied in-between the electrodes. In Fig. 12, the contour plot of the electric potential across the cell is provided, showing the potential gradually decreasing from the top plate. Fig. 13 provides the cross sectional view of the vector plot, showing how the electric field vectors vary across the hole and across the cell in the vertical direction.
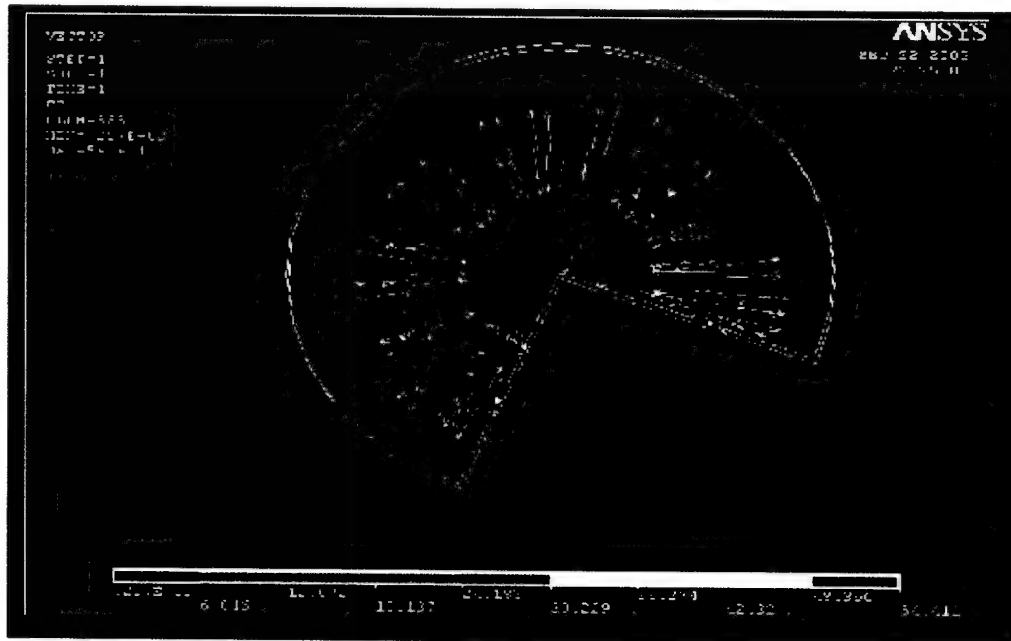

Fig 11: Top view of the electric field intensity across the hole of the electrode.
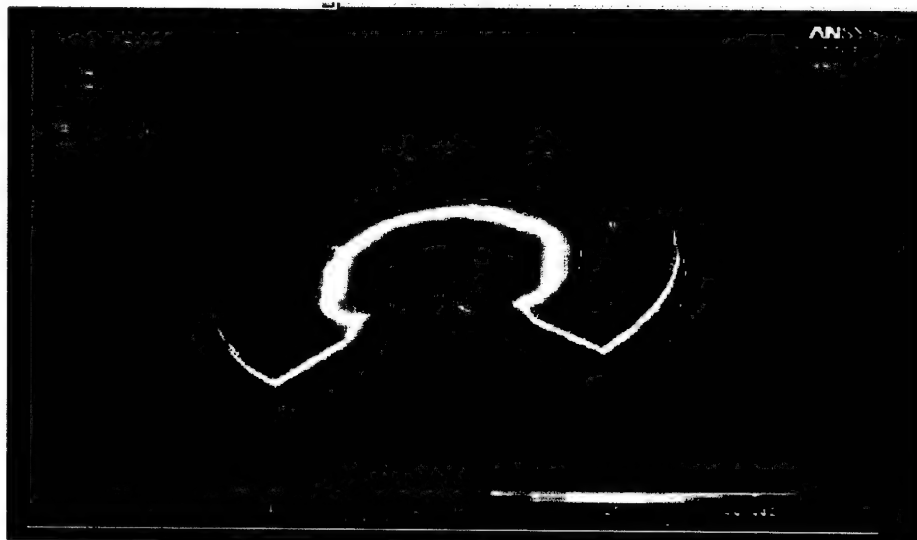

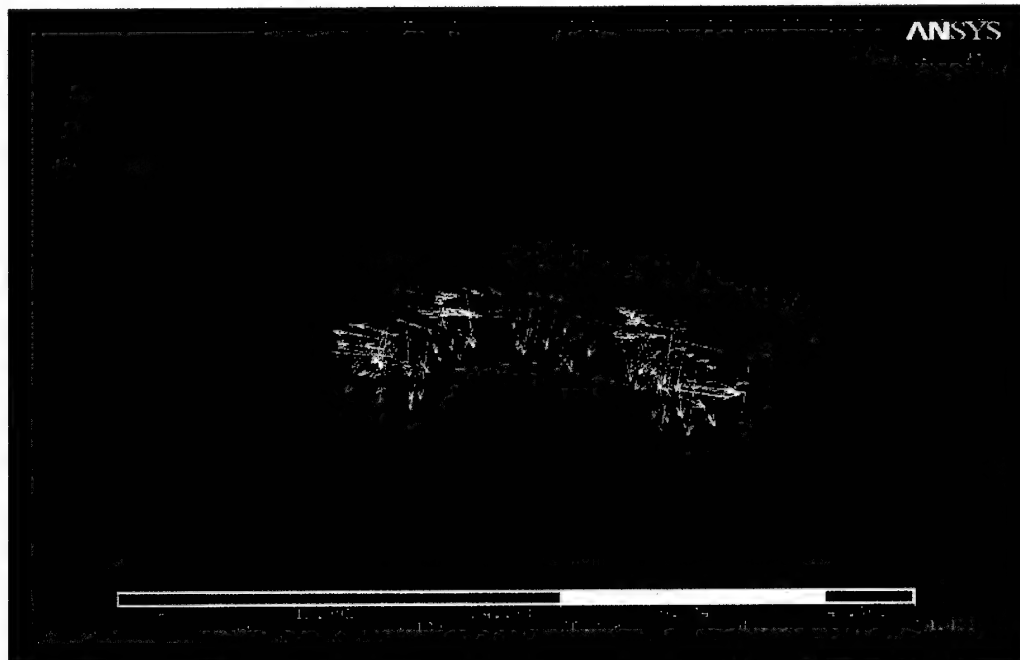Fig 2: Contour plot of electric potential across the cell.

Fig 13: Vector Plot of Electric Field across the Cell.

The hole patterned electrodes are ITO coated, and are fabricated using lithography, following the steps shown in Fig. 14. The procedure that was followed, first consisted of spin coating AZ 9260 photoresist on to the ITO coated glass slide. Then the electrode patterns are transferred to the photoresist by exposing it for 360 s. The intensity of the UV source used is 7 mW/cm^2. After exposing, the photoresist is developed for pattern transfer using AZ400 developer, which is mixed with water in the ratio of 1:4. Once the pattern is obtained, the ITO is etched by acid etching, using HCl and HNO$_3$ mixed in water. Two glass slides were prepared in this manner, and then bonded together. At this stage the PDLC is introduced into the cell.

ITO coated glass slide

AZ9260 PR coating

UV Exposure

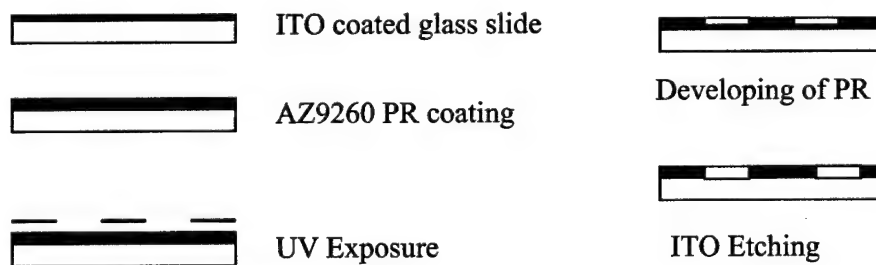Developing of PR

ITO Etching

Fig. 14 Electrode Fabrication Process

Experiment and Results

As mentioned in the above lines, PDLC is prepared by exposing the mixture of LC and monomer, and exposing them under the UV light. In this work, the monomers NOA-65 and NOA-81(from
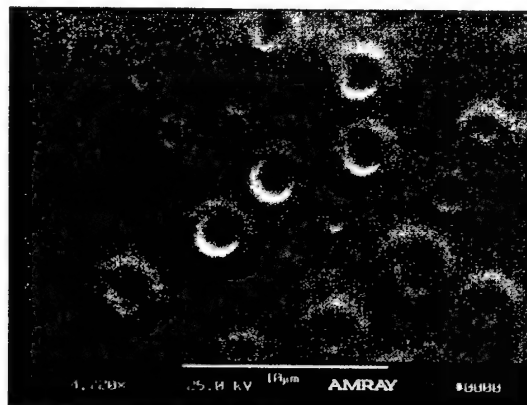
Norland Inc.) and BL 038 liquidcrystal (from EMD chemicals) have been chosen. Below are some SEM images of the PDLC using both monomers after UV light exposure. The intensity of the UV light used is 10 mW/cm^2.

Sample 1

LC: Monomer (NOA-81)= 50%:50%
Temperature = 50^{0}C
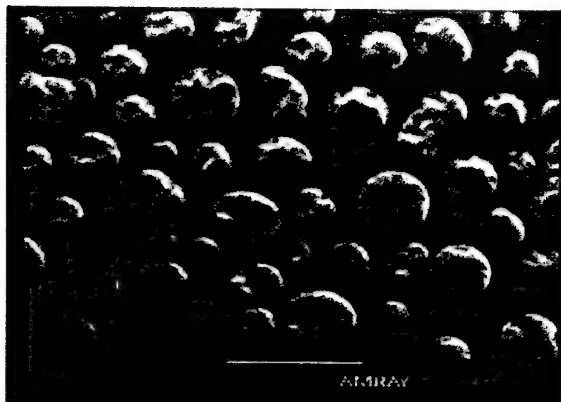
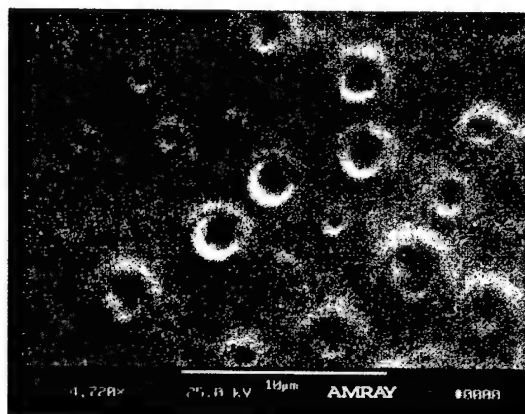Exposure Time = 15 min

Exposure Time = 10 min

These samples are the mixture of liquid crystal and monomer in the ratio of 50:50, and these are the samples which are exposed directly under UV light of intensity 10 mW/cm^2. One can observe the droplets may be of uniform size in a particular sample, and there may also be a variation in droplet size if the time of exposure is changed.

Sample 2:

LC: Monomer (NOA-81) = 30%:70%
Temperature = 50^{0}C

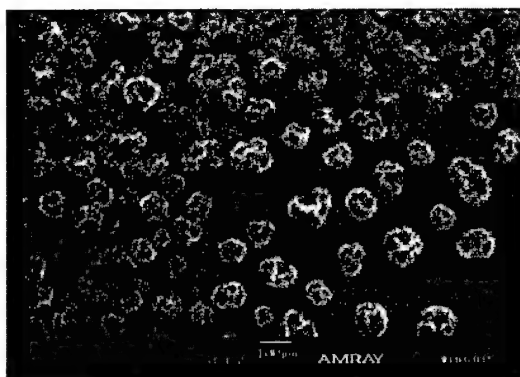Exposure Time =10 min

Exposure Time = 8 min
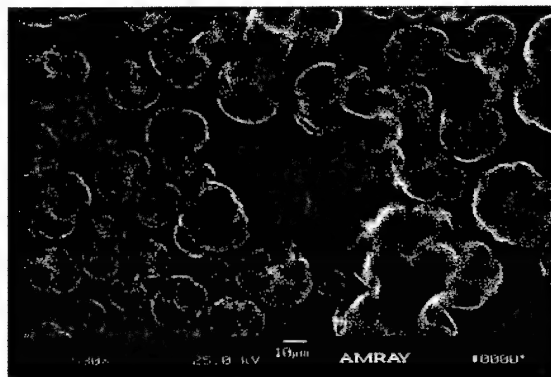
Sample 3:

LC: Monomer (NOA-65) = 30%:70%
Temperature = 50^{0}C

Exposure Time = 15 min   Exposure Time = 8 min

It is observed that NOA-65 is easily solvable in BL-038 and easily to be polymerized. The droplet size is also more uniform than for NOA-81.

The PDLC mixture is filled in between the two electrodes and the voltage is applied across them. At the voltage OFF state, the directors in the cell are randomly oriented and the cell behaves like an opaque medium. Once the voltage is applied, the directors are reoriented and the cell turns into a transparent one. A schematic of the testing system that has been setup for the measurement of the optical properties of the PDLC is shown in Fig. 15. The testing setup is used to measure the transmission efficiency of the lens. The laser light used in the testing setup has a wavelength of 636.2 nm.
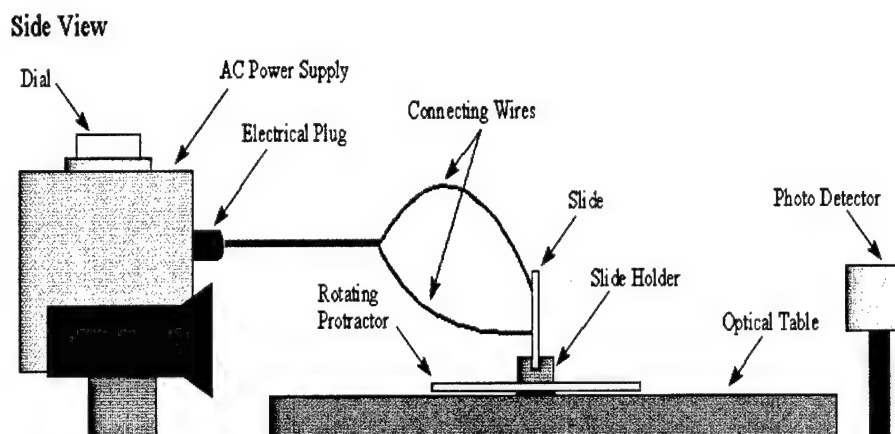

Fig. 15 Testing Setup

The samples prepared have been tested using the setup in Fig. 15. By applying voltage across the electrodes, there is a gradual increase in the voltage at the detector, indicating that the directors in the PDLC sample are reoriented when the voltage is applied across the cell. The voltage applied across the electrodes and the voltage at the detector has been recorded, and provided in the table shown below.

The graph obtained for the transmission efficiency is provided in Fig. 16 (photodetector output with control voltage).

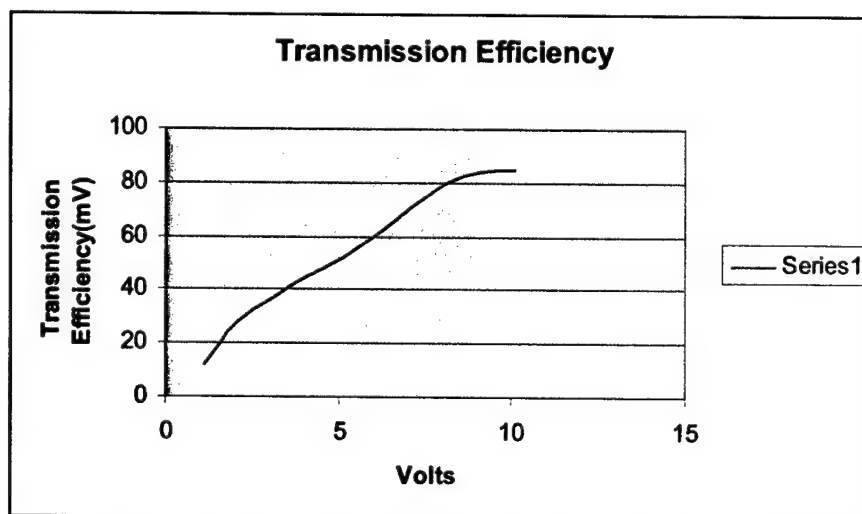| Voltage Applied on Electrodes (V)	Voltage at Detector (mV)
1.1	12
2.1	28
3.1	36.5
4.1	45.1
5.1	52.1
6.1	60.4
7.1	70.5
8.1	80
9.1	83.8
10.1	84.8

Fig. 16   Photodetector Output with Control Voltage

Approach 3: Diffusion of Copolymers

Another approach that has been investigated is the copolymer diffusion, with two different refractive index polymers. We selected PDMS as one copolymer. If this approach is successful, the lens structure can be easily integrated with electroactive polymer (EAP) actuator.

Theory and Background

The copolymer system investigated consisted of styrene (St) and methyl-methacrylate (MMA). This work was done for several reasons. First, there is little information about the use of GRIN polymer. There are few investigations of the diffusion properties. Styrene was used to diffuse into poly(methyl-methacrylate). This system provides a Δn of 0.1 and diffusion depths upward of 40 mm. This is among the largest Δn and deepest diffusion depths measured in a polymer system during the diffusion process. This provides a good start towards the material required for GRIN lenses. Figure 17 shows the sample of GRIN rod of Styrene-poly(methyl-methacrylate).

Figure 17: GRIN rod of Styrene-poly(methyl-methacrylate).

The GRIN lens with Styrene-poly(methyl-methacrylate) copolymer provides with a rigid lens structure. The focal length of this GRIN lens can not be changed due to the material properties. Therefore, a new design with deformable lens structure is needed. PDMS is not only a suitable material for EAP actuating mechanism, but also provides good optical and flexible lens characteristics. PDMS is a polymer which consists of long silicon chains. Macromer, short silicon chains, can diffuse into the matrix and be polymerized inside the matrix by UV light (Fig. 18). This forms a chemical distribution and induces a gradient refractive index profile.
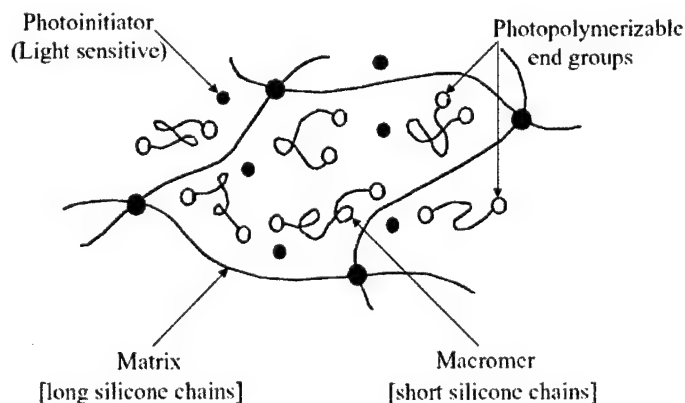

Figure 18: Schematic View of Copolymerization

Experiment and Results

After the PDMS lens has been fabricated, a monomer was used to diffuse to the PDMS lens, and get polymerized inside the lens. Several trail runs were conducted by using styrene or methyl-methacrylate. The PDMS lens swallows monomers and expands in volume. Figure 19 shows the final polymerization of monomers inside the PDMS. The original PDMS is transparent. After diffusing styrene or methyl-methacrylate and polymerizing by heat curing, the final PDMS became white and not transparent. There must be a chemical reaction occurring in the PDMS matrix and forming the white substance. Therefore, styrene or methyl-methacrylate may not be a proper monomers for the PDMS matrix.
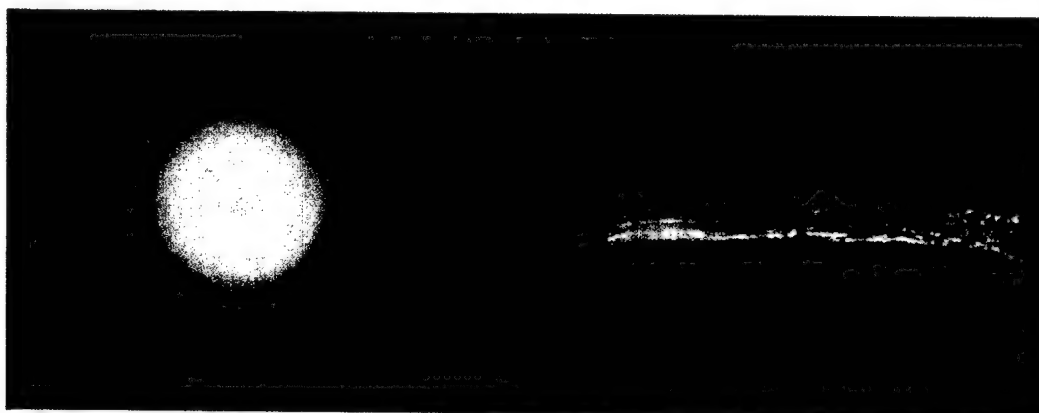

Fig. 19: Final Polymerization of Monomers in PDMS Substrate.

Currently, the research is focusing on the material synthesis for both macromers and photoinitiators. Research on material selections is in progress for GRIN distribution. The following table shows the possible materials that may be used for the first matrix, the guest macromers, the photo-initiators, and the UV absorbers.

PDMS Matrix	Macromers	Photo-Initiator	UV Absorber
MED-6033 NuSil	Vinyl Terminated Diphenylsiloxane Dimethylsiloxane (DMDPS)	Irgacure 369	UVAM
MED-6820 NuSil	Methacrylate endcapped Diphenylsiloxane Dimethylsiloxane	Irgacure 651	
Gelest DMS-D33		DMPA	
Dow Corning 165			
Dow Corning 6121			

A new fabrication technique that is capable of easy pattern formation for gradient-index polymer optical devices is proposed here. A guest macromer with higher or lower refractive indices is diffused into the first polymer matrix, which is made by PDMS, and then the diffusion profile is fixed by final polymerization. The gradient-index profiles can be selectively formed in the ultraviolet-irradiated regions, by utilizing the difference in diffusion rate. The proposed approach

is to modulate the refractive power of GRIN lens composed of a first cross-linked silicone polymer matrix (PDMS), a guest macromer, and a photoinitiator. The application of the appropriate wavelength of light onto the central optical portion of the lens polymerizes the macromer in the exposed region, thereby producing a difference in the chemical potential between the irradiated and nonirradiated regions. To reestablish thermodynamic equilibrium, unreacted macromer and photoinitiator diffuse into the irradiated region. As a consequence of the diffusion process and the material properties of the host silicone matrix, the lens will swell, producing a concomitant decrease in the radius of curvature of the lens and a corresponding shift in the refractive power of the lens. Figure 20 shows the schematic process flow.
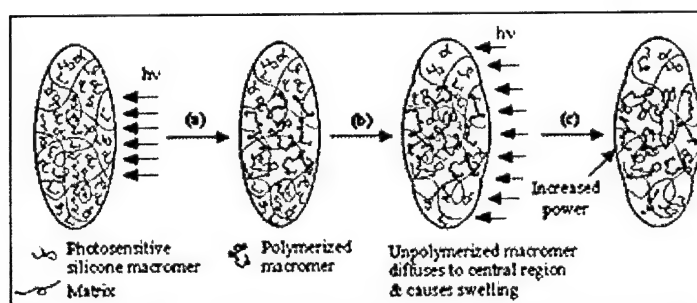

Fig. 20   Schematic Diagram Illustrating the Proposed Mechanism of Swelling

The novel GRIN planar lens comprises a first polymer matrix and a refraction modulating composition dispersed therein. The first polymer matrix forms the optical element framework and is generally responsible for many of its material properties. The refraction modulating composition (RMC) is a compound that is capable of photo polymerization. The refraction modulating composition is capable of photo-induced polymerization and may be monomers so long as:

1. it is compatible with the formation of the first polymer matrix;
2. it remains capable of photo-induced polymerization after the formation of the first polymer matrix; and
3. it is freely diffusible within the first polymer matrix.

Because of the requirement that the monomers must be diffusible within the first polymer matrix, the monomers generally tend to be smaller (have lower molecular weights) than the monomers, which form the first polymer matrix. In addition to the monomers, the refraction modulating composition may include other components, such as initiators and sensitizers that facilitate the formation of the second polymer matrix. In the current material research based on our pervious work on variable focal length lens and EAP actuation, the first polymer matrix is set to poly-dimethylsiloxane (PDMS). Based on the properties of PDMS matrix, material for the refraction modulation composition (RMC), such as macromers, photo-initiators, and sensitizers have been searched for finding proper materials and fulfilling the above three requirements. In the following section, the materials that can be used are discussed in detailed.

Another important reason for using this approach is due to the cross-linked silicone polymer matrix is made by PDMS with gradient refractive index distribution; it can be coupled with the EAP actuation mechanism. Thus, the entire device can be made of PDMS with two compliant electrodes, and it can fulfill the functions of gradient refractive index distribution, and variable focal length.

PART V: Electroactive Polymers Actuation

Over the past ten years, research on electroactive polymers (EAP) has become a "hot" field in applications for artificial muscle, robotics and toys. Their large electrically induced strains (longitudinal or bending), low density, mechanical flexibility and ease of processing offer advantages over traditional materials. These materials have characteristic similarities to biological muscles, and moreover, may be used as lens structure. In the meanwhile, we have developed the 3D lens fabrication processing, which can be exploited to fabricate the entire device, including the gradient lens and actuator, from the same material.

Theory and Background

The pervious research work on the microfluidic tunable focal length microlens has its drawback. The liquid filled lens requires a high power external syringe pump to generate enough fluidic pressure and to induce the deflection of the flexible PDMS diaphragm. Therefore, a new transducer design is needed for fine tuning focal length efficiently and precisely. Electroactive polymers (EAPs) have been studied and evaluated for replacing the existing microfluidic actuation chip. One of the electroactive polymers, which was developed as muscle-like actuator, is called dielectric elastomer, sometimes called "electroelastomer". PDMS is also a dielectric elastomer, which can be actuated by applying a voltage. Based on the existing PDMS microlens fabrication techniques, it can be used as the substrate with EAP actuation mechanism. This is one of the advantages that this project's actuation system switches from microfluidic chip to electronic transducer. Actuators based on dielectric elastomer technology operate on a simple principle. When a voltage is applied across the compliant electrodes, the polymer shrinks in thickness and expands in area. By changing in thickness, PDMS can be actuated with a maximum strain of about 63%. Figure 22 shows the principle of how EAP works.
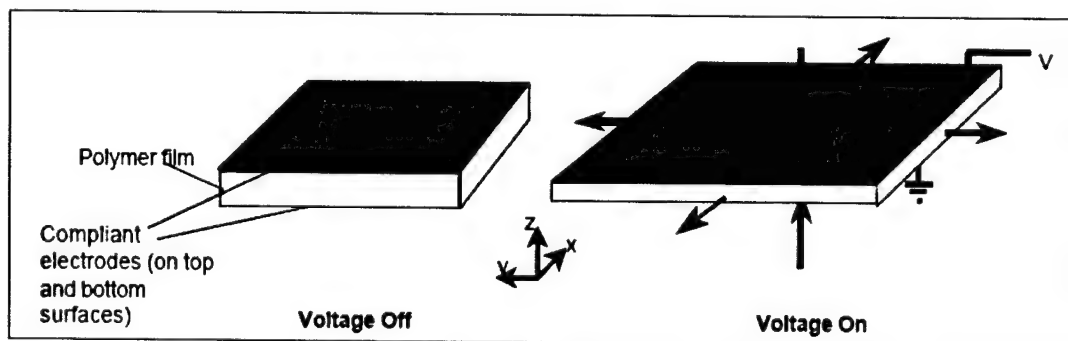

Fig. 22 Principle of Operation of Dielectric Elastomer Actuation.

There are two EAP actuator configurations proposed for dynamic tunable focal length in this report: out-of-plane and in-plane actuators. Both configurations use PDMS diaphragm mechanism, as described in the following lines.

Out-of-Plane EAP Actuator

The first EAP diaphragm actuator can take advantage of the large strain capability of dielectric EAPs to produce large out-of-plane deflections and correspondingly large axial displacement. This large deflection makes a concomitant decrease in the radius of curvature of the lens and a corresponding shift in the refractive power of the lens. The best films allow for out-of-plane deflection equal to 50% of the diaphragm diameter. Figure 23 shows a PDMS diaphragm actuator undergoing out-of-plane deformation in which the diaphragm changes shape from flat to hemispherical. The small number of moving parts will allow for high reliability operation.

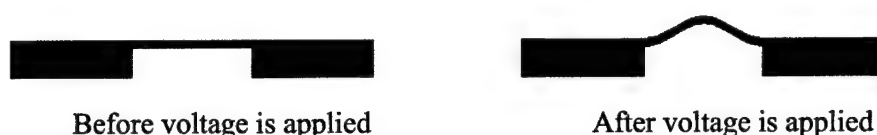Before voltage is applied   After voltage is applied

Fig. 23: Circular EAP with Out-of-Plane Deflection

In-Plane EAP Actuator

The second EAP diaphragm actuators can produce large in-plane area expansion, and cause the lens area be squeezed in area and thickness. A thin PDMS film has been stretched uniformly across a circular hole in a rigid frame. Carbon grease is applied to small hollow circles at the center of film and on top and bottom of film as compliant electrodes. When a voltage is applied to the electrodes, the film between the electrodes expands in area, and contracts in thickness. This expansion in area and contraction in thickness can cause the center portion of film be squeezed in area and thickness. By controlling the applied voltage, the area and thickness of the lens can be measured with an optical microscope, a video camera, video digitizing hardware, and digital measurement software. Thus, the lens' in-plane area changes can be determined when a given voltage is applied. By coupling with axial GRIN lens, the focal length varies when the refractive index distribution is changed by lens' area and thickness. By changing refractive index distribution along the distance from center axis, the focal length can be controlled accurately. Figure 24 shows the in-plane actuator mechanism and illustrates the change in refractive index distribution when the GRIN lens structure changes.
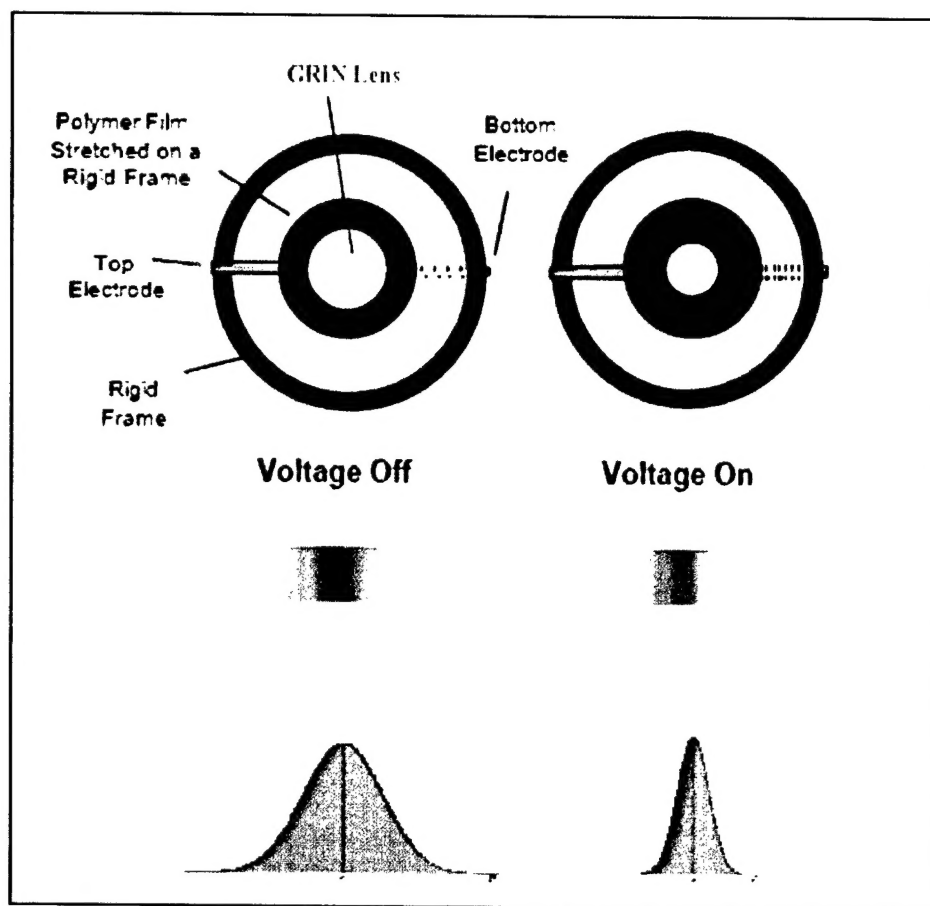
Fig. 24 In-Plane Movement with Circular EAP and the Refractive Index Distribution Change When the GRIN Lens Structure Changes.

Experiment and Results

Diaphragm Actuator for Lens Surface

Diaphragm actuators can take advantage of the large strain capability of dielectric EAPs to produce large out-of-plane deflections, and correspondingly large axial displacement. This large deflection makes a concomitant decrease in the radius of curvature of the lens and a corresponding shift in the refractive power of the lens.

The best films allow for out-of-plane deflection equal to 50% of the diaphragm diameter. Figure 25 shows a 75 µm thick PDMS diaphragm actuator undergoing out-of-plane deformation, in which the diaphragm changes shape from flat to hemispherical. Figure 26 shows the PDMS diaphragm with in-plane movement. The small number of moving parts will allow for high reliability operation.
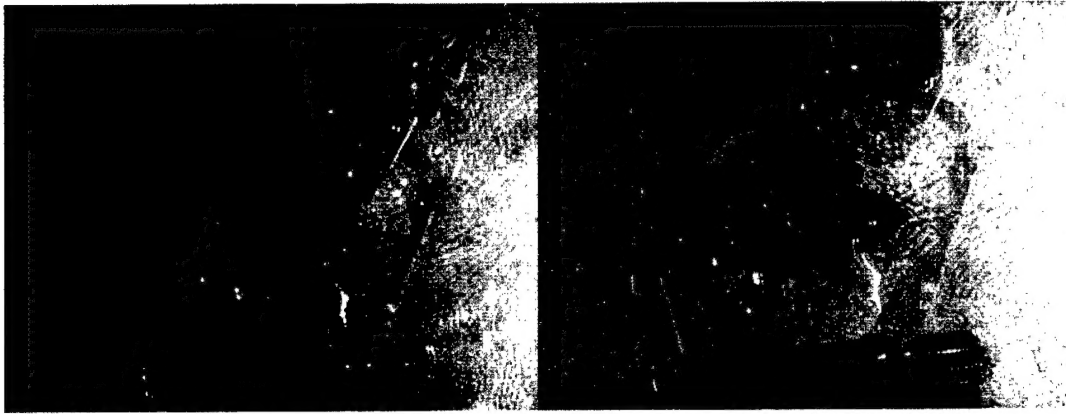
Fig. 25 PDMS Diaphragm Actuator Showing Large Out-of-Plane Motion in Response To an Applied Voltage.

Fig. 26 PDMS Diaphragm Actuator Showing In-Plane Motion in Response To an Applied Voltage.
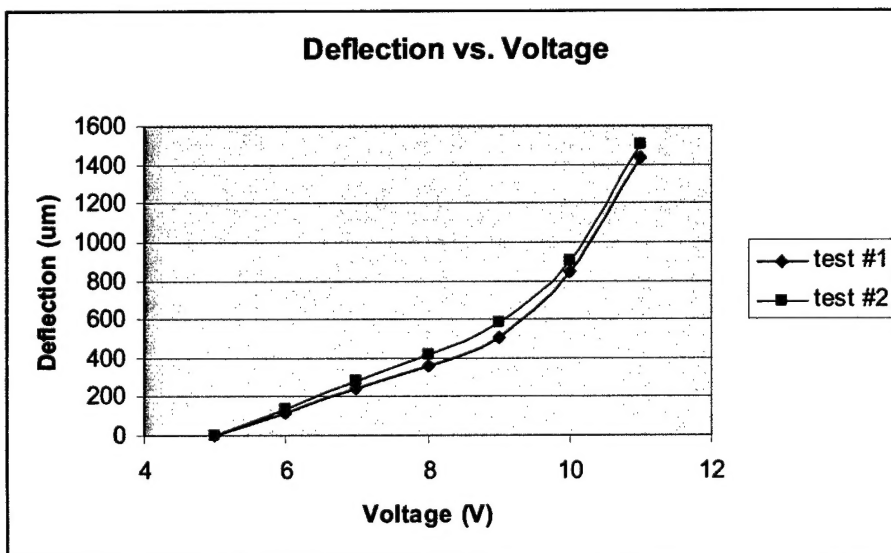

Fig. 27   Relationship between Defection and Applied Voltage

Figure 27 shows the relationship between the deflection and applied voltage. When the applied voltage exceeds 9 V, the deflection increases significantly. However, there is a linear deflection for the applied voltage between 6 to 9 V. In this linear actuation range, the deflection can be controlled precisely, and be used as the tunable focal length actuation mechanism.

PARTS IV & V - Future Work

The gradient refractive index lens structures have been successfully investigated and tested. The experimental results indicate that distributing the nanoparticles with electrophoresis, droplets control in dispersed liquid crystal, and diffusion copolymer with different refractive index; these three approaches can be used to fabricate the desired gradient refractive index lens structures. Based on the research work conducted, future work, if funded, will focus on optimizing the fabrication processing of the gradient refractive index lens structure and EAP actuator, and on the design, fabrication, and characterization of the prototype lens.

Project 3 Publications and Presentations

M. Agarwal, R. A. Gunasekaran, P. Coane, and K. Varahramyan, "Design and Fabrication of Variable Focal Length Microlens System," submitted for publication to Optics Express Journal, November 2003.

R. A. Gunasekaran, M. Agarwal, A. Singh, P. Dubasi, P. Coane, and K. Varahramyan, "Design and Fabrication of Fluidic Controlled Dynamic Optical Lens System," submitted for publication to Optics Communications, November 2003.

J. Chen, W. Wang, J. Fang, and K. Varahramyan, "Variable-Focusing Microlens with Micro Fluidic Chip," submitted for publication to Journal of Micromechanics and Microengineering, November 2003.

J. Chen, W. Wang, J. Fang, and K. Varahramyan, "Design and Fabrication of a Variable-Focusing Microlens," TexMEMS V Conference, Forth Worth, TX, May 2003.

Project 3 Disclosure

R. A. Gunasekaran, K. Varahramyan, M. Agarwal, A. P. Singh, and P. S. Dubasi, "Design and Fabrication of Wide Angle Variable Focal Length Optical Lens System," Report of Invention, October 30, 2003.

AD NUMBER

AD NUMBER	DATE	DTIC ACCESSION NOTICE

1. REPORT IDENTIFYING INFORMATION

A. ORIGINATING AGENCY

Louisiana Technical University

B. REPORT TITLE AND/PR NUMBER

New Technologies for Polymer...

C. MONITOR REPORT NUMBER

44365.1-MS

D. PREPARED UNDER CONTRACT NUMBER

DAAD19-02-1-0338

2. DISTRIBUTION STATEMENT

A

REQUESTE

1. Put your
   on revers
2. Complet
3. Attach fc
   mailed t
4. Use unc
   informat
5. Do not c
   for 6 to

DTIC:
1. Assign .
2. Return .

2004 0112 023